MATERIALS ENGINEERING FOR HIGH EFFICIENCY THIN FILM ELECTROLUMINESCENT DEVICES

Emmanuel Antoine MASTIO

- 5 MAY 2000

A thesis submitted in partial fulfilment of the requirements of The Nottingham Trent University for the degree of Doctor of Philosophy

Department of Electrical and Electronic Engineering

The Nottingham Trent University

December 1999

ProQuest Number: 10290293

Abstract

The effect of annealing on electroluminescent devices based on inorganic ZnS:Mn (phosphor) thin films has been investigated. Conventional thermal annealing is compared with a new technique utilising pulsed optical irradiation of the thin film structure. Typically, alternating current thin film electroluminescent (TFEL) structures consist of a phosphor thin film sandwiched between two insulating layers and the light is produced via high field electroluminescence mechanisms. In the past, conventional thermal annealing at temperatures >500 °C has been demonstrated to increase the number of active luminescent centres, but also to modify the density of electrons trapped at the phosphor / insulator interface which was suggested to limit device performance. Thus, to further improve the luminescence efficiency of TFEL devices, laser annealing was proposed as a means to heat the phosphor thin film at high temperatures but without altering the interface states density.

In the present work, laser irradiations were performed directly on the un-coated phosphor using 20 ns pulses of KrF lasers. During laser annealing the samples were placed in a pressurised environment to limit the phosphor sublimation, which is described to be the mechanism responsible for laser ablation processes. Crystalline analyses using x-ray diffraction were performed and a thermal model was developed. The combination of experimental results and theoretical analysis demonstrate that pulsed KrF laser annealing enables in-depth phase transitions within the phosphor layer with minimal energy absorption at the interfaces and cladding dielectrics. Photoluminescence investigations suggest that the phase transition is concomitant to an increase of the number of active luminescent centres. Hence, it is demonstrated that this novel annealing technique is suitable for electroluminescence applications and experimental evidence is shown by a fourfold increase in device brightness compared to thermally treated devices at 450 °C. According to the simulation, the structural, and the luminescence analyses, this improved electroluminescence efficiency is attributed to localised annealing of the phosphor thin film with minimal modifications at the phosphor / dielectric boundary, which was the premise behind this study.

Résumé

L'effet de recuit a été examiné sur des dispositifs électroluminescent à base de couches minces inorganiques en ZnS:Mn (phosphorant). Le recuit thermique classique est comparé avec une nouvelle technique utilisant des irradiations optiques pulsées sur la structure en couches minces. Typiquement, les structures des dispositifs électroluminescents à base de couches minces (TFEL) fonctionnant au courant alternatif consistent en un film phosphorant pris en sandwich entre deux couches isolantes; la lumière étant produite par des mécanismes d'électroluminescence sous l'action de grands champs électriques. Dans le passé, il a été démontré que le recuit thermique classique utilisé à des températures >500 °C augmente le nombre de centres luminescents actifs. Mais il modifie aussi la densité d'électrons piegés à l'interface phosphorant / isolant susceptible de limiter la performance du dispositif. Ainsi, pour améliorer d'avantage le rendement lumineux d'afficheurs TFEL, le recuit laser fut proposé comme un moyen pour chauffer le film phosphorant à de hautes températures mais sans modifier la densité des niveaux d'énergie d'interface.

Dans le cadre de ce travail, les irradiations laser furent appliquées directement sur le phosphorant non recouvert en utilisant des impulsions de 20 ns provenant de lasers KrF. Durant le recuit laser, les échantillons furent placés dans un environnement pressurisé pour limiter la sublimation du phosphorant supposée être le mécanisme responsable des processus d'ablation laser. Des analyses cristallines au moyen de diffraction aux rayons X ont été faites et un modèle théorique a été développé. La combinaison des résultats expérimentaux et théoriques démontre que le recuit par laser KrF pulsé permet une transition de phase en profondeur dans la couche phosphorante avec une absorption minimale d'énergie aux interfaces et revêtements diélectriques. Des mesures de photoluminescence suggèrent que la transition de phase est concomitante à une augmentation du nombre de centres luminescents actifs. Ainsi, il est démontré que cette nouvelle technique de recuit convient aux applications électroluminescentes et la preuve expérimentale est donné par une augmentation quadruple de la brillance du dispositif comparée à des dispositifs traités thermiquement à 450 °C. En accord avec la simulation et les analyses structurelles et de luminescence, cette amélioration du rendement d'électroluminescence est attribuée à un recuit localisé du film phosphorant avec des modifications minimales à la limite phosphorant / diélectrique ce qui fut en prémisse de cette étude.

L'Homme se sent comme un étranger dans ce monde régit par l'Esprit qui calcule et mesure

Man feels like a stranger in this world, ruled by the Spirit that calculates and measures

Acknowledgements

List of Publications (refereed journals)

E. A. Mastio, W. M. Cranton, C. B. Thomas, E. Fogarassy, and S. de Unamuno. *Pulsed KrF laser annealing of RF sputtered ZnS:Mn thin films*, Appl. Surf. Sci. **138-139**, 35 (1999).

E. A. Mastio, M. Robino, E. Fogarassy, M. R. Craven, W. M. Cranton, and C. B. Thomas, *The effects of KrF pulsed laser and thermal annealing on the crystallinity and surface morphology of radiofrequency magnetron sputtered ZnS:Mn thin films deposited on Si*, J. Appl. Phys. **86** (5), 2562 (1999).

E. A. Mastio, E. Fogarassy, W. M. Cranton, and C. B. Thomas, *Ablation study on pulsed KrF laser annealed electroluminescent ZnS:Mn / Y_2O_3 multilayers deposited on Si*, accepted for publication in Appl. Surf. Sci. (2000).

E. A. Mastio, C. B. Thomas, W. M. Cranton, and E. Fogarassy, *The effects of multiple KrF laser irradiations on the electroluminescence and photoluminescence of RF sputtered ZnS:Mn based electroluminescent thin film devices*, accepted for publication in Appl. Surf. Sci. (2000).

E. A. Mastio, W. M. Cranton, and C. B. Thomas, *Thermal annealing effects on recrystallisation and luminescence properties in ZnS:Mn based alternating-current thin film electroluminescent devices*, submitted to J. Appl. Phys.

E. A. Mastio, W. M. Cranton, and C. B. Thomas, *Pulsed laser annealing for high efficiency thin film electroluminescent devices*, submitted to J. Appl. Phys.

D. C. Koutsogeorgis, E. A. Mastio, R. Stevens, W. M. Cranton, C. B. Thomas, *Photoluminescence improvement of RF magnetron sputtered Y2O3:Tb thin films by KrF pulsed laser annealing*, submitted to Appl. Phys. Lett.

List of Publications (conference proceedings)

W. M. Cranton, C. B. Thomas, R. Stevens, M. R. Craven, S. O. Barros, E. A. Mastio, and P. S. Theng, *Laterally Emitting Thin Film Electroluminescent Devices For Head Mounted Displays*, Proc. Electronic Information Displays Conference (1997).

W. M. Cranton, E. A. Mastio, C. B. Thomas, R. Stevens and J. P. O. Evans. *Laser annealing for high intensity flat screen displays*, CLF-RAL Annual Report, 147 (1997).

E. A. Mastio, W. M. Cranton, and C. B. Thomas. *Phosphor dopant activation using pulsed KrF laser annealing*, CLF-RAL Annual Report, 11 (1998).

D. A. Pepler, R. Allott, A. Boba, W. M. Cranton, C. N. Danson, G. Hirst, D. Koutsogeorgis, E. A. Mastio, D. Neely, M. Notley, M. Payne, and T. Winstone, *Materials processing with high power lasers*, Diffractive Optics **99** Proc. (1999).

E. A. Mastio, W. M. Cranton, and C. B. Thomas. *KrF laser annealing of ZnS:Mn thin film phosphors*, CLF-RAL Annual Report, (1999).

Contents

CHAPTER 3: Crystallinity and surface morphology of laser annealed ZnS:Mn thin films grown on Si

CHAPTER 6: Thermal annealing effects upon the interface structure of ZnS:Mn / Y2O3 multilayers

CHAPTER 7: Pulsed laser annealing for high efficiency thin film electroluminescent devices

CHAPTER 8: Conclusions and Further work

APPENDIX A: Conversion Factors

APPENDIX B: Shadow mask designs for ITO deposition

PUBLISHED ARTICLES

x

Abbreviations

a.c.	Alternating Current
a.u.	Arbitrary Units
AFM	Atomic Force Microscopy
Ar	Argon
$BaTiO_3$	Barium Titanate
B-V	Brightness-Voltage
C	Celsius
CCD	Charge Coupled Device
CRT	Cathode Ray Tubes
CW	Continuous Wave
d.c.	Direct Current
EL	Electroluminescence
EPSRC	Engineering and Physical Sciences Research Council
eV	Electron Volts
FED	Field Emission Display
fL	Foot-Lambert
FWHM	Full Width at Half Maximum
HMD	Head Mounted Display
JCPDS	Joint Committee on Powder Diffraction Standards
K	Kelvin
KrF	Krypton Fluoride
LCD	Liquid Crystal Display
LSF	Laser for Science Facility
N_2	Nitrogen
Ne	Neon
PHASE	Laboratoire de Physique et Applications des Semiconducteurs
PL	Photoluminescence
psi	Pound-force per Square Inch
RAL	Rutherford Appleton Laboratory

RHEED	Reflection High Energy Electron Diffraction
RMS	Random Mean Square
SEM	Scanning Electron Microscope
Si	Silicon
SID	Society for Information Display
STEM	Scanning Transmission Electron Microscope
TFEL	Thin Film Electroluminescence
TFTs	Thin Film Transistors
TITANIA	High power laser facility at RAL
TNTU	The Nottingham Trent University
UV	Ultra Violet
wt%	Weight Percent
XeCl	Xenon Chloride
XRD	X-Ray Diffraction
Y_2O_3	Yttrium Oxide
ZnS	Zinc Sulphide
ZnS:Mn	Zinc Sulphide doped with Manganese
ZnS:TmF	Zinc Sulphide doped with Thulium Fluoride

Variables

λ	Wavelength
α	Optical absorption coefficient
ρ	Density
η_{exc}	Excitation efficiency
θ_{hkl}	Half of the diffraction angle
η_{out}	Light outcoupling efficiency
τ_p	Laser pulse duration
η_{rad}	Radiative efficiency
$2\theta_{hkl}$	Diffraction angle
a	Lattice constant
$B(2\theta)$	FWHM in radians
C_s	Specific heat
E	Energy
E_d	Energy density
E_g	Energy bandgap
$g(E)$	Density of trapping states at the phosphor / insulator interface
hkl	Miller indices
I_{hkl}	Diffraction intensity of the hkl lattice plane
k	Thermal conductivity
L	Luminance
L_c	Average crystal dimension
n	Order of lattice plane reflection
n_e	Density of hot electrons
N_L	Density of active luminescent centres
P_d	Power density
R	Surface reflectivity (normal)
S	Heat generation by optical absorption
T	Temperature
V_{th}	Threshold voltage for electroluminescence

CHAPTER 1: Introduction

I.   Introduction

A. Thin film electroluminescent devices for head mounted displays

In the field of flat panel display technology, thin film electroluminescence (TFEL) continues to provide the solution for applications requiring a rugged, high contrast display screen with wide viewing angle and a large temperature operating range.[1]

A practical application of TFEL technology is the head mounted display (HMD).[2] In its simplest form, an HMD consists of an image source (TFEL display) and collimating optics that images the information into the user's eye. The visual information can be seen directly with occluded external vision for a fully immersive projection, or the HMD may incorporate a semi-transparent window to provide a non occluded display overlaid on the outside world view. In the latter form, the HMD superimposes information on normal vision and the projected display image must be bright enough to permit viewing over ambient background illumination. Being attached to the head, the HMD must not impede movement and prevent discomfort. Hence, it should also be as small and as lightweight as possible.

Alternative technologies for HMD are available, but fall short of satisfying the whole range of requirements. For example, cathode ray tubes (CRT) provide high brightness and resolution but have high power consumption and are bulky and heavy.[3]   A much newer innovation dating from the 60's, which has seen

development during this decade is the Field Emission Display (FED). Unlike the CRT this is a flat screen display with the electron emission from individual cathodes, addressing the phosphors of equivalent pixels. Although, the FED dimensions may be suitable for HMD, its brightness is not yet high enough for ambient viewing (non occluded display).[4] Similarly, liquid crystal displays (LCD) may be very suitable for some applications,[5,6,7] but in an HMD, the required intensity levels demand a high brightness light source which is power intensive and may also be likely to create heating problems. Furthermore, a LCD display, unlike the emissive TFEL, CRT, or FED display, requires a separate light source, thus increasing size and weight.

Recently, the displays research group at The Nottingham Trent University (TNTU) has demonstrated the use of TFEL technology with a novel high resolution, miniature, display device that utilises laterally transmitted light to produce high intensity emission with reflecting microstructures.[8,9] Miniature flat screen displays based on this technology have sufficient luminance (>3000 fL), which is the minimum requirement of effective sunlight readable HMD.[4] This brightness has been obtained using inorganic thin films of ZnS:Mn which are the most efficient and widely used active light emitting layer in TFEL displays.[10,11] However, it would be of great advantage to further enhance the luminescent efficiency of these devices, particularly where highly attenuating optical systems may be necessary for practical application. In addition, a major objective of the future TFEL development is to extend the technology to encompass full colour display applications,[12,13,14] which also requires enhancements in device performance so that low efficiency blue phosphors may be effectively used.

B. Background

TFEL displays are all solid state structures based on the device first demonstrated by Sharp in 1974,[15] and typically consist of a thin film phosphor layer (active layer) sandwiched between dielectric thin films (e.g. Y_2O_3, $BaTiO_3$), with a transparent electrode,[16] and glass substrate allowing the internally generated light to be viewed by the user.

Critical to the luminescent efficiency of any phosphor material is a post annealing treatment, which allows for the active incorporation of the luminescent dopant ions within the host lattice. Commercial TFEL phosphors, commonly used in large area flat panel displays, are typically subjected to a post deposition anneal at 500 °C for ~1 hour, which is the maximum practical temperature that may be employed due to the need for glass substrates. TFEL devices developed at TNTU, however, do not rely upon surface emission and may therefore be fabricated on silicon wafers (Figure 1).

Substrates of silicon are advantageous in that: (i) standard silicon processing techniques may be employed to fabricate device structure, (ii) integration of drive and control electronics is feasible,[17] and (iii) higher annealing temperatures may be investigated.
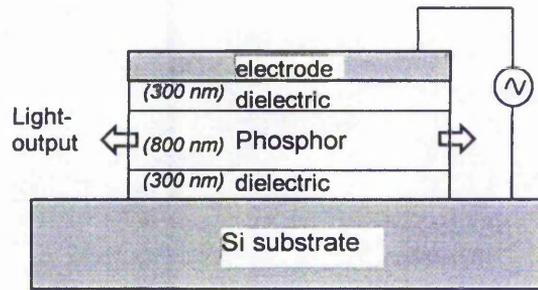
FIG. 1. Schematic TFEL structure developed at TNTU. The substrate used is silicon and light is emitted laterally as opposed to conventional surface emission.

C. Definition of the problem

To achieve the desired enhancement in efficiency of a typical TFEL structure as mentioned in Section IA, it is necessary to consider the physics of light generation via high field electroluminescence. This is best illustrated by an energy band diagram as shown in Figure 2.[18,19,20,21]

Under the application of an electric field, electrons trapped at the interfacial region between the phosphor and cladding insulator are liberated by tunnelling into the conduction band of the phosphor.[22] Acceleration of these electrons by the high field results in the gain of energy, which may then be imparted to the luminescent ions within the phosphor by impact excitation.[23,24] For the ZnS:Mn phosphor, the luminescent ions have a first excited state at 2.1 eV above the ground state.[25] Hence, electrons attaining an energy >2.1eV may impact excite the Mn^{2+}.[26]
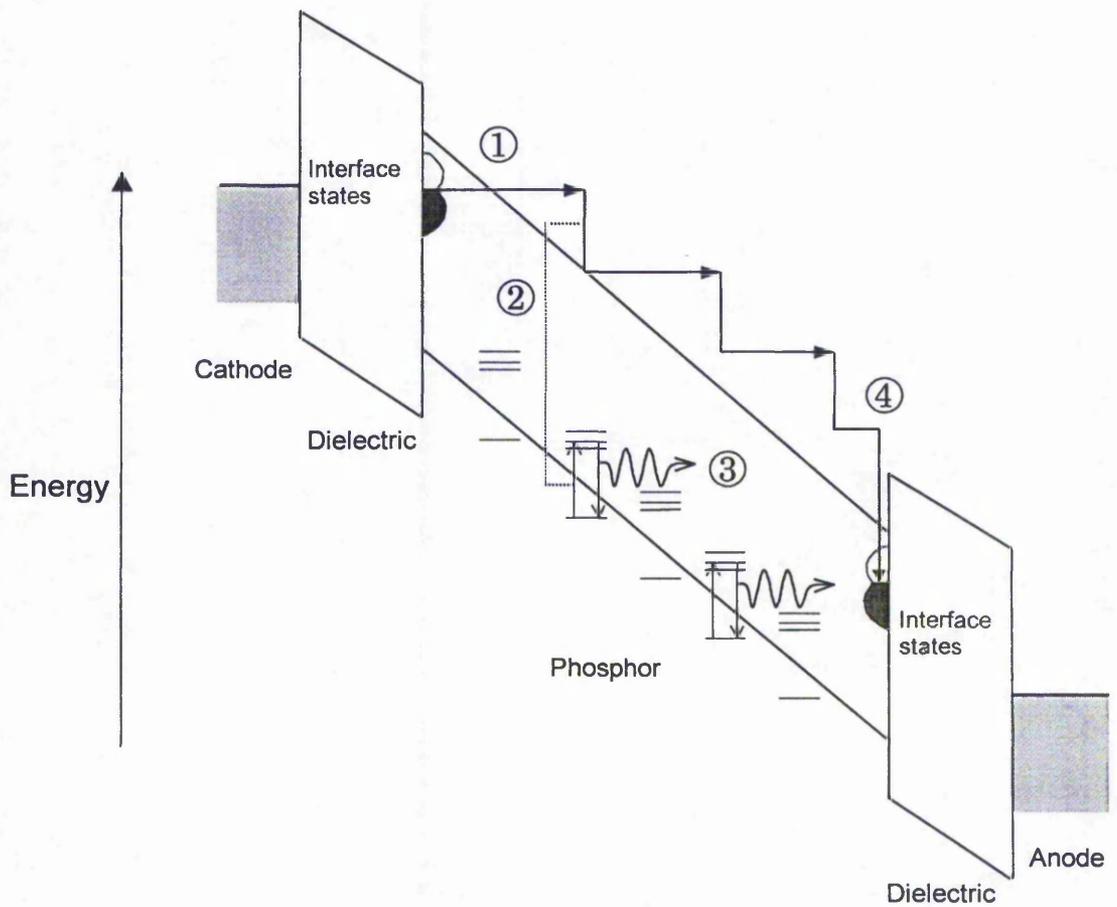
① Tunnel emission of electrons and acceleration due to applied field

② Impact excitation of luminescent centres

③ Radiative emission

④ Re-trapping of electrons at anodic interface

FIG. 2. Simplified energy band diagram of a typical TFEL structure. Electroluminescence arises following the distinctive mechanisms ① to ④.

The luminescence resulting from the electroluminescence process may be expressed mathematically by the relation:

$$L = \text{Function } (N_L, n_e, \eta_{exc}, \eta_{rad}, \eta_{out}), \tag{1}$$

where: L = luminance, N_L = density of active luminescent centres, n_e = density of hot electrons (electrons accelerated to energies >2.1 eV), η_{exc} = excitation efficiency, η_{rad} = radiative efficiency, η_{out} = light outcoupling efficiency. For a conventional TFEL device, n_e is dependent on the density of trapping states (g(E)) at the phosphor / cladding layer boundary and on the tunnelling rate at a particular applied field.

By concentrating on the lateral, as opposed to surface emission, the TFEL devices developed at TNTU exhibit a four-fold improvement in emitted intensity via the use of micro-mirror technology, which is a result of an improved η_{out}.[27] By using the silicon substrates, the Display Group at TNTU was also able to explore thermal annealing effects at temperatures >500 °C, and in doing so, demonstrated that the density of active luminescent centres (N_L) increases with annealing temperatures.[28] However, while annealing improved N_L, L saturated and it was suggested that annealing is responsible for a reduction of n_e. In fact, based on the results of a electrooptical model developed by W. M. Cranton, such behaviour can be shown to be due to a reduction of g(E) with annealing that is concomitantly un-pinning the Fermi energy level.[27] Consequently, a reduction occurs also of the field strength at which electrons commence tunnelling from interface states into the ZnS:Mn conduction band. The reduced field leads subsequently to a reduction of n_e. So while thermal annealing increases, the penalty is a reduction of n_e.

Clearly an adequate annealing technique must be employed to increase N_L but without reducing n_e and consequently, reducing or limiting L (Equ. 1).

The four main parameters involved in the annealing treatment of TFEL devices are time, temperature, treated volume, and environment. The conventional thermal annealing technique for TFEL devices is effective when processing times are of the order of one hour.[29] Thus, the entire structure heats up which limits the annealing temperature to ~500 °C by either the type of substrate used, e.g. melting temperature of glass, or by the induced modifications on the interfacial electron trapping states as mentioned above. A further temperature limit for the conventional thermal annealing treatment (in vacuum) is induced from the ZnS:Mn phosphor itself since it sublimes at ~1300 K under atmospheric pressure.[30]

II.   Proposed solution and objectives

Based on the results and annealing temperature limitations discussed in the previous section, it is proposed that the use of pulsed excimer laser annealing could provide a more effective means of heat treating the phosphor thin films for TFEL devices.[31] This laser processing technique has been intensively studied to improve the electrical properties of silicon based thin film transistors (TFTs),[32,33,34,35] but no successful results have been published on laser annealed TFEL devices. The first work on pulsed excimer laser annealing of phosphors was reported by H. S. Reehal, et al., in 1982. In the latter, the examined samples were not designed for electroluminescence applications but some results were used as a starting point for the present PhD (see Chapter 2).

By use of a suitable irradiation wavelength and optical energies, it is intended to optimise the process so that the optical energy is absorbed and dissipated primarily within the ZnS:Mn thin film, with minimal effect upon the insulating layers and hence the interface regions. Ideally, therefore, this novel annealing process will exhibit the beneficial effects of high temperature annealing (increase of N_L), but without concomitant modification of the electronic interface at the phosphor / dielectric boundary (n_e unchanged).

Additionally, previous work showed that the excitation and radiative efficiencies (η_{exc}, and η_{rad}) of TFEL devices are increased when improving the crystallinity of the active layers.[36] Hence, by generating high annealing temperatures

and, potentially, crystallographic transformations via pulsed laser annealing, these two factors may be increased as well, resulting in a further enhancement of the luminescent characteristics (see Equ. 1 in Section IC).

Thus, the primary aim of this work is to define the optimum pulsed laser annealing conditions of phosphor layers to produce highly efficient TFEL devices.

The specific objectives are to:

- Develop an experimental technique to laser anneal TFEL devices with non or minimal ablation of the films.

- Study of the effect of pulsed laser annealing on the photoluminescence properties of ZnS:Mn thin film phosphors deposited on silicon substrate.

- Perform thermal simulations of the pulsed laser annealing process using a one-dimensional thermal model. Maximal surface and interface temperatures will be emphasised.

- Study of the structural properties of the pulsed laser annealed samples.

- Validate the thermal model based on the results of structural characterisations.

- Grow suitable electroluminescent structures for pulsed laser annealing processing.

- Study of the photoluminescence, electroluminescence, and structural properties of the pulsed laser annealed samples.

III.   Collaborations and available facilities

- The thin films of ZnS:Mn and Y_2O_3 are deposited using existing facilities at TNTU (Chapter 2) and luminescence properties of TFEL structures are analysed at TNTU via photoluminescence and electroluminescence measurements at room-temperature.

- Pulsed laser annealing experiments are performed at the Rutherford Appleton Laboratory (RAL) as part of the EPSRC grant No GR/K90074. The time covered by the research grant was a period of three years (1/1/1997 – 31/12/99).

  At RAL, two irradiation arrangements were available. One comprising a commercial laser at the Laser for Science Facility (LSF) and a second one purely experimental called TITANIA. Both are KrF lasers emitting at a wavelength of 249nm (~20 ns pulse width) but TITANIA has a considerably larger output power and beam size. Hence, TITANIA was used to provide large irradiated samples to facilitate structural analyses. On the other hand, due to its better performance stability, higher repetition rates, and flexibility, the beam of the commercial laser was used to investigate various pulse numbers with small laser power density increments.

- Structural analyses were available at the Semiconductors Physics and Applications (PHASE) laboratory at Strasbourg (France) under a collaborative scheme. There, access was provided to high quality characterisation methods providing crucial feedback to the work carried out at TNTU and RAL.

Specifically, the collaboration permitted access to x-ray diffraction (XRD) and atomic force microscopy (AFM) measurements.

Moreover, a thermal model of the laser-matter interactions was also available at Strasbourg. This model was used as a characterisation tool, and as such, it was not intended to develop it further within the research schedule.

IV.   Programme and structure of the thesis

Preliminary evaluations of the effects of laser processing on solely the phosphor layer (directly deposited on Si) are presented in Chapters 2 and 3. The main reasons for studying this monolayer are to demonstrate the potential of this novel process to increase the density of active luminescent centres and to study the induced structural modifications within the phosphor layer.

The thin film deposition technique used throughout this thesis is briefly described in Chapter 2. Also presented is the annealing arrangement using the commercial KrF laser at RAL, the thermal model developed at PHASE, and photoluminescence investigations.

Chapter 3 shows the experimental TITANIA laser facility at RAL as well as XRD and AFM analyses performed on thermally and laser annealed ZnS:Mn thin films deposited on Si.

Building on the knowledge and experimental observations gathered from Chapters 2 and 3, Chapters 4 to 7 are dedicated to studies of TFEL structures (multilayers).

In Chapter 4, the thermal model is applied to ZnS:Mn / Y_2O_3 multilayers deposited on Si and an ablation study is conducted to understand and establish the limitation of the laser annealing processing when using multiple pulse irradiations at high laser power densities.

Chapter 5 shows the photoluminescence and electroluminescence results obtained from measurements performed on the laser processed samples from Chapter 4. Laser annealed device performance are compared with those of thermally annealed devices and the observed brightness limitations are interpreted in terms of electronic interface modifications at high annealing temperatures.

In Chapter 6, a detailed crystallographic study of the insulator and phosphor layers thermally annealed at temperatures up to 600 °C gives more insight into the possible mechanisms responsible for the interface states modifications and the induced electroluminescent brightness limitations at high annealing temperatures.

The latter structural results are used in Chapter 7 in order to probe the temperatures generated by KrF pulsed laser annealing within the ZnS:Mn / Y_2O_3 multilayers. It is shown that under certain irradiation conditions, TFEL structures processed with single pulse laser annealing exhibit a fourfold increase in brightness compared to conventionally thermally annealed devices. This improvement agrees well with the annealing dependent interface structure discussed in Chapter 6 and with the optoelectronic model described in Chapter 1.

Finally, Chapter 8 contains concluding remarks and suggestions for further work.

References

[1] P. Rack and P. Holloway, Mater. Sci. and Eng. **R21**, 171 (1998).

[2] J. E. Melzer and Moffitt, *Head Mounted Displays* (McGraw-Hill, 1997).

[3] L. E. Tannas, *Flat Panels Displays and CRTs* (Van Nostrand, Princeton, 1985).

[4] C. Stavely (Fraser Nash Research Ltd., Surrey, UK), private communication.

[5] W. A. Barrow, R. C. Coovert, E. Dickey, C. N. King, C. Laakso, S. S. Sun, R. T. Teunge, R. Wentross, and J. Kane, SID **93** Digest 761 (1993).

[6] T. Parados, H. P. Maruska, W. Halverson, R. A. Budzilek, D. Monarchie, and E. Schlam, SID **93** Digest 777 (1993).

[7] C. N. King, Conference Record of the 1994 International Display Research Conf. 69 (1994).

[8] C. B. Thomas, W. M. Cranton, and R. Stevens, SID **96** Digest (1996).

[9] W. M. Cranton, C. B. Thomas, R. Stevens, M. R. Craven, S. O. Barros, E.A. Mastio, and P. S. Theng, Proc. Electronic Information Displays Conference (1997).

[10] Y. A. Ono, Encyclopedia of Appl. Phys. **5**, 295 (1993).

[11] R. Mach and G. O. Mueller, Phys. Stat. Sol. (a) **69**, 11 (1982).

[12] J. Haaranen, R. Tornqvist, J. Koponen, T. Pitkanen, M. Surma-aho, W. Barrow, and C. Laasko, SID **92** Digest 348 (1992).

[13] K. O. Velthaus, U. Troppenz, B. Huttl, R. Herrman, and R. H. Mauch, Conference Record of the 1994 International Display Research Conference 346 (1994).

[14] W. A. Barrow, R. C. Coovert, E. Dickey, T. Flegal, M. Fullman, C. King, and C. Laakso, Conference Record of the 1994 International Display Research Conference 448 (1994).

[15] T. Inoguchi, M. Takeda, Y. Kakihara, Y. Nakata, M. Yoshida, SID **74** Digest (1974) 86.

[16] R. Tueto and M. Braguier, Thin Solid Films **80**, 143 (1981).

[17] C. B. Thomas, I. P. McClean, R. Stevens, and W. M. Cranton, IEEE Electron. Let. **30** (16), 1250 (1994).

[18] D. H. Smith, J. Lumin. **23**, 209 (1981).

[19] A.Onton and V. Marello, Advances in image pickup and display **5**, 137 (1982).

[20] K. A. Neyts and P. De Visschere, J. Appl. Phys. **68** (8), 4163 (1990)

[21] E. Bringuier, J. Appl. Phys. **66** (3) 1314 (1989).

[22] G. Vincent, A. Chantre, and D. Bois, J. Appl. Phys. **50** (8), 5484 (1979).

[23] J. W. Allen, J. Lumin. **23**, 127 (1981).

[24] E. Bringuier, J. Appl. Phys. **70** (8), 4505 (1991).

[25] N.T. Gordon, IEEE Trans. Elect. Dev. **ED-28** (4), 434 (1981).

[26] E. Bringuier, J. Appl. Phys. **75** (9), 4291 (1994).

[27] R. Stevens, C. B. Thomas, and W. M. Cranton, IEEE Electron. Device Let. **15**, 1997 (1994).

[28] W. M. Cranton, R. Stevens, C. B. Thomas, A. H. Abdullah, and M. R. Craven, Poc. IEE Colloquium on Materials for Displays, 1995.

[29] J. M. Hurd and C. N. King, J. Electronic Materials **8**, 879 (1979).

[30] W. M. Cranton, P. H. Key, D. Sands, C. B. Thomas, F. X. Wagner, Appl. Surf. Sci. 96-98 (1986) 501.

[31] W. M. Cranton, E. A. Mastio, C. B.Thomas, R. Stevens and J. P. O. Evans, CLF-RAL Annual Report, 147 (1997).

[32] E. Fogarassy, H. Pattyn, M. Elliq, A. Slaoui, B. Prevot, R. Stuck, S. de Unamuno,

and E. L. Mathé, Appl. Surf. Sci. **69**, 231 (1993).

[33] P. Baeri and E. Rimini, Mater. Chem. and Phys. **46**, 169 (1996).

[34] K. Choi, Y. Uchida, and M. Matsumura, Jpn. J. Appl. Phys. **35**, 1648 (1996).

[35] T. Inushima, N. Kusumoto, N. Kubo, H-Y. Zhang, and S. Yamazaki, J. Appl. Phys. **79** (12), 9064 (1996).

[36] H. Xian, P. Benalloul, C. Barthou, and J. Benoit, Jpn. J. Appl. Phys. **33**, 5801 (1994).

CHAPTER 2: Pulsed KrF laser annealing of ZnS:Mn thin films deposited on Si

I.   INTRODUCTION

The aim of this initial study is demonstrate the possibility of improving the luminescent properties of a sputtered phosphor thin film by pulsed laser annealing. This has necessitated the construction of a pressure cell to house the target wafer during laser annealing, since previous work has demonstrated that it is essential to carry out these experiments with the samples held under inert gas pressure to prevent material loss at high irradiation levels.[1] In Ref. 1, H. S. Reehal, et al., reported successful pulsed laser annealing of ZnS thin films implanted with Mn ions when irradiating under 90 psi (~6.2 bars) of Ne. They investigated the photoluminescence improvements obtained using a laser fluence of 2.8 J/cm^2 at various pressures from 15 (~1 bar) to 90 psi, and showed that slight loss of material still occurred at 90 psi, suggesting that higher pressures may be employed. Therefore, the pressure cell used in the present work has been constructed to withstand pressures up to 150 psi (~10.34 bars).

In the following, the influence of the surrounding gas pressure during laser exposure, the laser power density, and double irradiation are investigated to probe their effects on the luminescent properties of the ZnS:Mn layer. Also, the thermal model of the laser-matter interaction is presented and results are compared with previous structural investigations.[1]

II.   EXPERIMENTAL CONDITIONS

A. Samples

Two 800 nm thick ZnS:Mn thin films were sputtered onto polished n-type single crystal (100) silicon wafers, from a pressed powder ZnS:Mn target. The Mn concentration of the source material is 0.45 wt% i.e. ~2.45×10^{20} ions/cm^3, which is the optimum value when using conventional thermal annealing.[2]

Growth was performed in an argon atmosphere at 3 mT using a cluster magnetron radio-frequency deposition system.[3] An interferometric monitor was used to determine the film thickness during growth. The final thickness of 800 nm has been established by profile measurements from edges of the thin film to non-coated Si areas, using a Dektak II surface profilometer. The thickness uniformity is determined to be better than ±5% across the 4-inch wafer. The substrate temperature was maintained at 200 °C during the 2 hours of deposition time. Typically, a sputtered ZnS:Mn thin film is polycrystalline (predominantly cubic) in nature,[4] with columnar structure. In the following, the two depositions are reported as NTU185(LSF2) and NTU201(LSF3).

B. Laser annealing conditions

In order to achieve efficient absorption of the laser irradiation in the phosphor thin film, it is necessary to irradiate with photons of energy greater than the band gap (~3.66 eV for ZnS), since at lower energy these films are optically transparent.[5]

With KrF laser emission of 249 nm corresponding to ~4.98 eV, the optical absorption coefficient α has been determined to be 3.33×10^5 cm^{-1} for crystalline ZnS and 3.15×10^5 cm^{-1} for polycrystalline ZnS:Mn thin films.[6,7] Irradiation of the samples was performed under 150 psi (~10.34 bars) of Ar pressure to prevent atmospheric contamination and laser ablation[8,9] due to the low ZnS vapour pressure at atmospheric pressure. The evacuable pressure cell (Fig. 1) in which the wafer was mounted is fitted with an UV-grade quartz window. To facilitate the accurate positioning of the target wafer in the KrF laser beam, an XZ motion was designed using two micropositionning stages (±10 μm accuracy over a total travel of 200mm), capable of supporting 30kgs. Computer control of the stepper motor drives allows the positioning of specific target areas of the wafer.
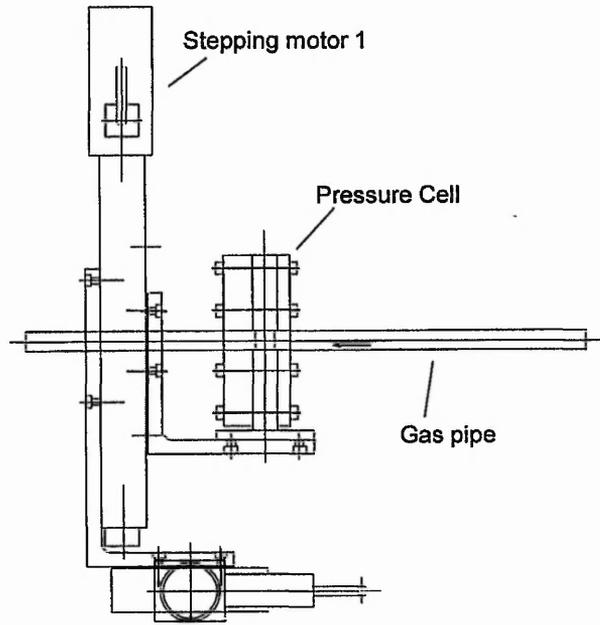
Side view
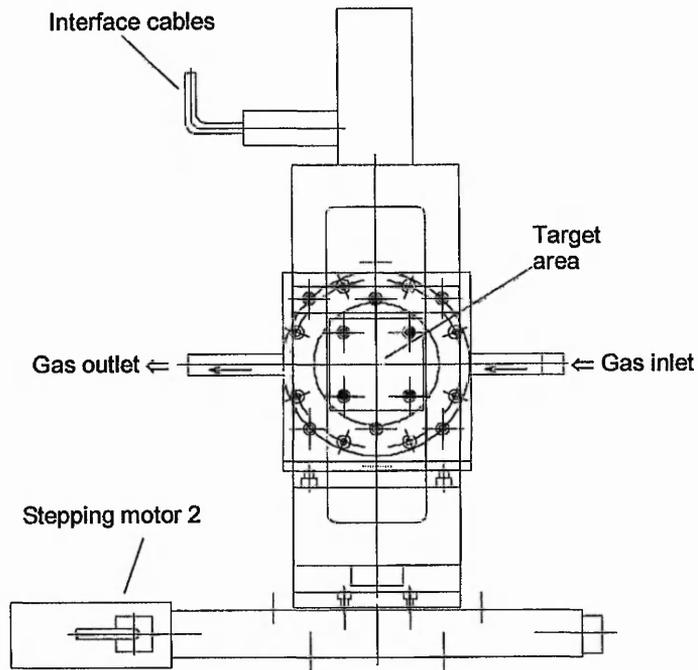
Front view

FIG. 1. XZ motion and pressure cell design.

Laser irradiation of the samples was carried out using the arrangement shown in Figure 2. A first rectangular aperture was used to select a uniform region at the unstable cavity output of a commercial KrF laser beam. The aperture was focused onto the coated Si wafer using a quartz lens (f = 2.5 m). A second aperture placed near the pressure cell allowed refinement of the impinging beam uniformity.

On line diagnostic of the 20 ns pulsed KrF (248 nm) laser beam was achieved using two HOYA plates (fused silica) as beam splitters (reflectivity ~8%). A CCD camera fitted with an interference filter centred at 248 nm was used for the beam uniformity analysis, and a cross-calibrated Gentec ED 200 energy-meter (sensitivity = 9.29 V/J) for the energy measurement. Beam uniformity over the 2 mm x 2.5 mm laser spot (at target) was determined to be better than ±10%. Variations of the impinging power densities were obtained by serial combinations of HOYA plates, each transmitting ~92% (Fresnel losses) of the incident laser beam. The obtained power density range varied from 2.6 MW/cm^2 to 39 MW/cm^2.

The number of laser shots utilised for this initial phase of experimentation was either one or two. The time delay between consecutive pulses was always longer than one second, ensuring complete thermal relaxation of the wafers and the pressure cell.
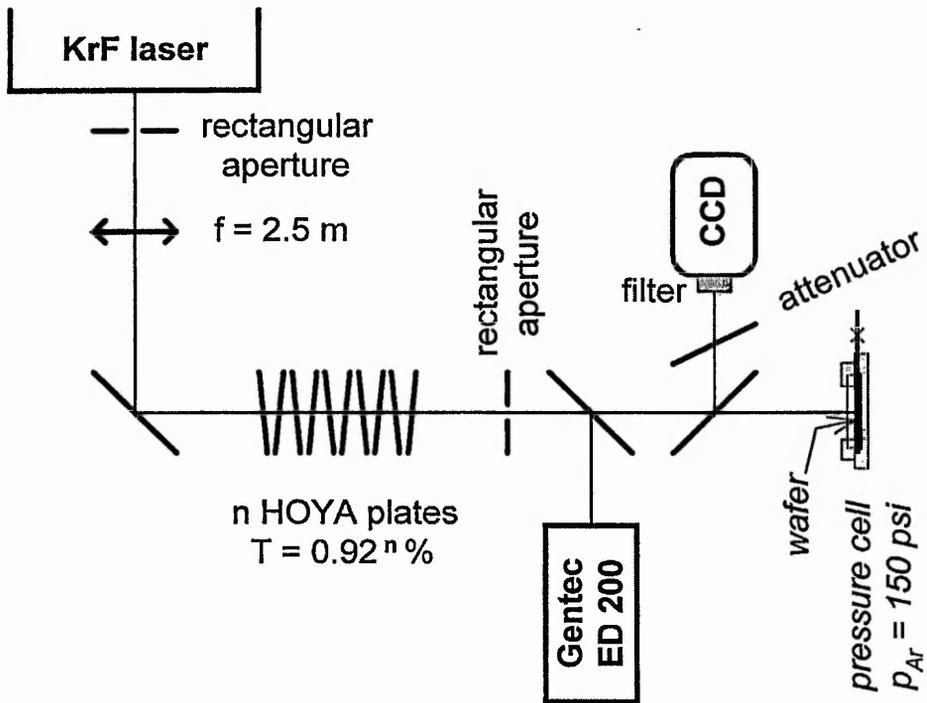
FIG.2. Experimental system for multiple KrF irradiations under 10.34 bars of argon pressure. Control of the laser energy impinging on the sample is provided by n HOYA plates (fused silica) transmitting 0.92^n % of the initial irradiation energy. On-line diagnostics of the energy and beam uniformity are provided by a Gentec ED200 and a CCD camera, respectively.

C. Photoluminescence measurement

In the ZnS:Mn system, Mn^{2+} ions are incorporated into the host lattice by direct substitution on Zn^{2+} lattice sites.[10] Their characteristic orange photoluminescence emission was measured before and after laser processing. Excitation of the phosphor was accomplished at room temperature with a pulsed N_2 laser (337 nm i.e.~3.68 eV) operating at 20 Hz, 6 mW average power, and 400 mJ maximal energy per pulse. At this excitation wavelength, photoluminescence excitation is mainly achieved via energy transfer from electron hole pair recombination following direct excitation of the host lattice ($E_{g,ZnS}$ ~3.6 eV).

Photoluminescence signals were measured via a Minolta LS110 luminance-meter placed at right angles to the examined samples. A remote voltmeter coupled to the luminance-meter output permitted signal readings when operating in a dark room (very low background signal) and a probe-station allowed accurate positioning of the tested samples. The reported values are all relative to non-annealed regions for comparative analysis between the various laser power densities.

III. THERMAL SIMULATION OF THE LASER-MATTER INTERACTION

As discussed in Chapter 1, the temperature control of the phosphor bulk and its interface during post-deposition annealing are crucial for TFEL applications. Since measurements of these temperatures are difficult during laser processing, the thermal effect of pulsed laser annealing has been simulated by solving the one-dimensional heat flow equation:[11]

$$C_s\rho\frac{\partial T(x,t)}{\partial t} = \frac{\partial}{\partial x}\left(k\frac{\partial T(x,t)}{\partial x}\right) + S(x,t),\tag{1}$$

where C_s represents the specific heat, ρ the density and k the thermal conductivity of the different layers. The temperature T and heat generation S are functions of space and time. The heat generation can be described as

$$S(x,t) = P_d(t)\alpha\,(1\text{-}R)\exp(\text{-}\alpha x),\tag{2}$$

where $S(x,t)$ depends on the optical absorption α and surface reflectivity R of the material. $P_d(t)$ is the time dependent power density of the laser beam.

The accuracy of the modelling is strongly related to how precisely the optical and thermal properties of the irradiated materials are known. Si is probably the best understood component thanks to semiconductor technology but for the phosphor

layer, even if ZnS is an "old" material, the reported optical and thermal parameters of its polycrystalline form are non-exhaustive. Hence, the assumption was made that the low doped polycrystalline ZnS:Mn thin film possesses the same properties as a single crystal zincblende structure. The different parameters used for calculation are reported in Table I.

Further assumptions used to perform the simulations were:

(i) No temperature dependence on the thermal and optical properties.

(ii) Omission of the necessary transformation energy for the cubic to hexagonal phase transition of ZnS (latent heat).

(iii) No edge effects, since the width of the laser beam is much greater than the heated sample thickness.

(iv) Perfect laser beam uniformity and constant rectangular laser pulse duration of 20ns.

(v) Homogeneous thin film composition.

TABLE I. Optical and thermal parameters of the phosphor thin film and the substrate used for simulation. Values determined at 300 K. The melting temperature of ZnS was determined under an argon pressure of 150 psi.

	c-ZnS	*c*-Si
$R_{(\perp \text{ to surface})}$ at 249nm	0.27 [6]	-
α (cm^{-1}) at 249nm	3.33x10^5 [6]	-
T_{melting} (K)	2100$^{\pm20}$ [12]	1683 [11]
$T_{\text{transition}}$ (K)	1295 [13]	-
$T_{\text{sublimation}}$ (K)	~1273 [9] (estimated value)	-
k (W/cm.K)	0.251 [14]	1.40 [11]
C_s (J/kg.K)	472 [14]	745 [11]
ρ (g/cm^3)	4.079 [14]	2.32 [11]

IV. RESULTS AND DISCUSSION

A. Thermal model

Based on the simulation of the thermodynamic effect of KrF pulsed laser annealing on 800 nm thick films of ZnS on Si, Fig. 3 shows the calculated maximal transient temperatures attained at the phosphor layer surface and at the phosphor / substrate interface, as a function of incident laser power density. Both surface and interface temperatures are increasing linearly with laser power density, and their heating rates are 59 and 13.6 $K/MW.cm^{-2}$, respectively.

The surface melting point and phase transition temperature from the cubic to hexagonal structure for single crystal ZnS are $T_{melting} = 2100$ K and $T_{transition} = 1295$ K, respectively (Table I). Using these temperatures as reference points, we can determine the expected laser power density required for solid-liquid and cubic (sphalerite) to hexagonal (wurzite) phase transitions; i.e. respectively 30.5 MW/cm^2 and 17 MW/cm^2 (610mJ/cm^2 and 340 mJ/cm^2).

In the past, structural investigations of ZnS thin (200nm) films, deposited on Si and implanted with Mn ions, implied a possible melting threshold in the region of ~0.6 - 0.8 J/cm^2 when irradiated with a XeCl laser (pulse duration ~40 ns) under 90 psi (~6.2 bars) of Ne.[1] Interestingly, the calculation of the melting fluence using the experimentation conditions of the latter work gives 0.7 J/cm^2, which agrees well with the experimental observations.
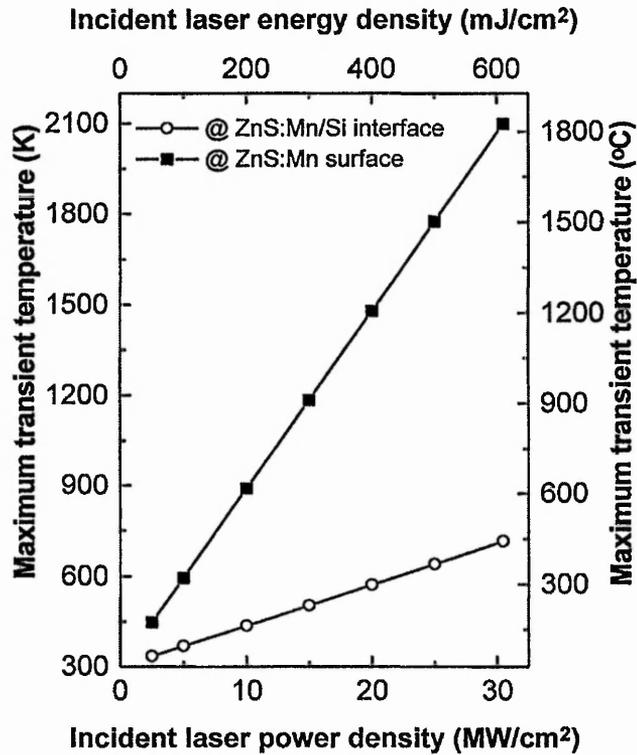
FIG. 3. Simulated maximal transient temperatures attained at the ZnS:Mn surface and the ZnS:Mn / Si interface as function of incident KrF laser power density. Their heating rates are 59 and 13.6 K/MW.cm^{-2}, respectively. The modelled rectangular laser pulse duration is 20 ns.

B. Photoluminescence analysis

Increase in photoluminescence for laser irradiated samples relative to non annealed samples were obtained with the specimens held under 150 psi of argon pressure as shown in Figures 4 and 5. As suggested by the thermal simulation, no melt-regrowth and eventual grain growth should occur below an impinging laser power density of 30.5 MW/cm^2. Moreover, transient photoluminescence measurements of similar laser annealed samples did not show any increase in decay time with annealing at laser power densities up to ~24 MW/cm^2.[15] This suggests that η_{rad} remains constant within this laser power density range. Hence, higher photoluminescence is mainly attributed to an increase of the number of active luminescent centres (N_L) within the ZnS host lattice or improved electron-hole pair generation and recombination rates. This increase is linearly dependent with the laser power density even in the range where the phase transition is expected (Fig. 5).

Double shot irradiation also shows a linear behaviour but at a higher improvement rate compared to single irradiation (Fig. 4). Since the action of several pulses cannot be additive due to the interval between them (nanosecond regime), it can be concluded that the structure formed on each shot influences subsequent coupling of the radiation to the samples. Therefore, as the laser power density is increasing, the double shot irradiation benefit from improved coupling due to changes induced by the initial shot.

Zinc sulphide sublimes before melting at normal pressure and Fig.4 highlights clearly the predicted sublimation when irradiating under one atmosphere. The loss of material is followed by photoluminescence reduction above the ablation threshold of ~7.5 MW/cm^2. This value is in fairly good agreement with that found when using a XeCl excimer source to process a ZnS target, at atmospheric pressure.[9]

A more detailed ablation investigation of the ZnS:Mn ablation mechanisms will be presented in Chapter 4. However, it is already interesting to note that the optical energy necessary for sublimation at atmospheric pressure ($p_{Ar} = p_{atm}$), is similar to the one necessary for photoluminescence improvement when $p_{Ar} = 150$ psi. Since the sublimation and transition temperatures are very close (Table I), one could presume that the allotropic transition of zinc sulphide may play a role in the activation of the Mn^{2+} ions.
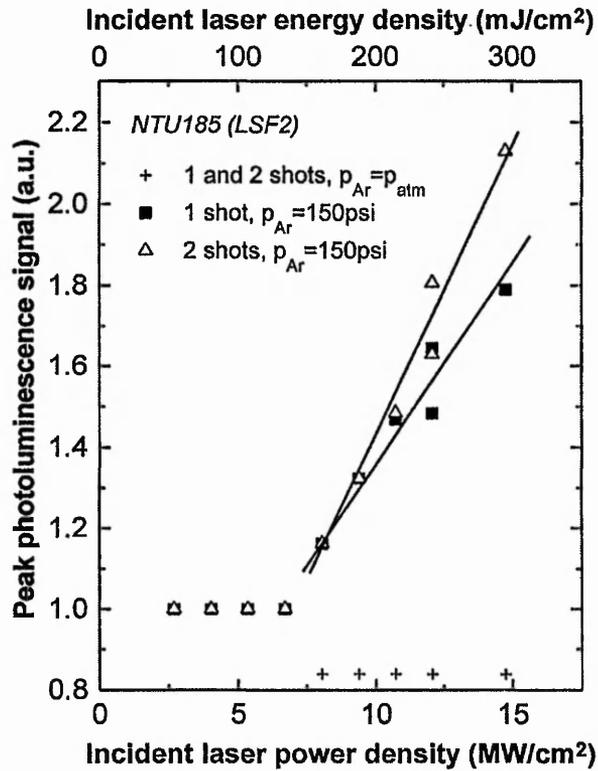
FIG. 4. Relative photoluminescence versus incident laser power density of 800 nm ZnS:Mn film deposited onto a Si wafer after annealing with a 20 ns pulsed KrF excimer laser. Single and double shot irradiation under atmospheric ($p_{Ar} = p_{atm}$) and 150 psi of Ar pressures. The photoluminescence was excited using a pulsed N_2 laser operating at 20 Hz and emitting at a wavelength of 337 nm. Below 7 MW/cm^2, the triangles, squares, and crosses overlap.
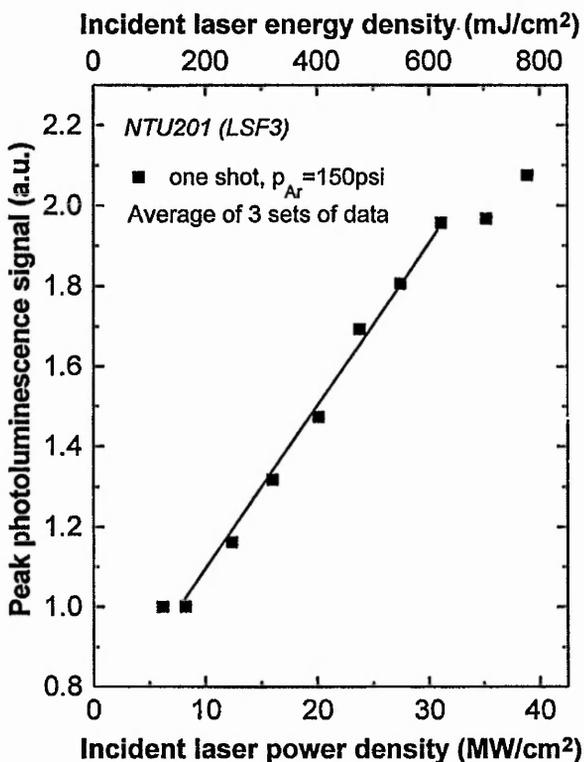
FIG. 5. Relative photoluminescence versus incident laser power density of 800 nm ZnS:Mn film deposited onto a Si wafer after annealing with a 20 ns pulsed KrF excimer laser. Single shot irradiation performed under 150 psi Ar pressure. Each datum point corresponds to the mean value measured from three separately annealed regions. The data points are linearly interpolated up to the simulated melting threshold of 30.5 MW/cm^2 (straight line). The photoluminescence was excited using a pulsed N$_2$ laser operating at 20 Hz and emitting at a wavelength of 337 nm.

V.   CONCLUSIONS

The most significant result to emerge from this study is the linear dependence between the photoluminescence improvement factor and the laser power density when irradiating beyond a threshold value and under an argon overpressure. Hence, it is demonstrated that the pulsed KrF laser annealing technique is suitable for activating the luminescent centres of TFEL phosphors.

Thermal simulation of the pulsed laser annealing suggests that temperatures attained at the phosphor surface and at the ZnS:Mn / Si interface are proportional to the impinging laser power density. Thus, the linear behaviour shown by calculation and experimentation may imply a linear correlation between the Mn^{2+} luminescence efficiency and the temperatures attained within the phosphor layer.

Finally, the thermal model suggests that the photoluminescence improvement is obtained in the solid state and that linearity is conserved during phase transition. In the following chapter, x-rays diffraction analysis will be used to probe the crystallographic transition.

REFERENCES

[1] H. S. Reehal, J. M. Gallego, and C. B. Edwards, Appl. Phys. Lett. **40**(3), 258 (1982).

[2] W. M. Cranton, PhD Thesis, University of Bradford, (1995).

[3] W. M. Cranton, D. M. Spink, R. Stevens, and C. B. Thomas, Thin Solid Films **226**, 156 (1993).

[4] L. E. Tannas, *Flat Panels Displays and CRTs* (Van Nostrand, Princeton, 1985), p. 260.

[5] H. S. Reehal and C.B. Edwards, Ann. Rep. Laser Facility Committee, SERC Rutherford and Appleton Labs, 2.17-2.18 (1981).

[6] S. Ozaki and S. Adachi, Jpn. J. Appl. Phys. **32**, 5008 (1993).

[7] P. M. Savani, M. Phil thesis, University of Bradford, 1982, p. 97.

[8] D. Sands, F. X. Wagner, P. H. Key, J. Appl. Phys. **85**, 3855 (1999).

[9] W. M. Cranton, P. H. Key, D. Sands, C. B. Thomas, F. X. Wagner, Appl. Surf. Sci. **96-98**, 501 (1996).

[10] P. Rack and P. Holloway, Mater. Sci. and Eng. **R21**, 171 (1998).

[11] S. de Unamuno and E. Fogarassy, Appl. Surf. Sci. **36,** 1 (1989).

[12] A. Addamiano and P.A. Dell, J. Phys. Chem. **61**, 1020 (1957).

[13] A. Addamiano and M. Aven, J. Appl. Phys. **31**, 36 (1960).

[14] *Handbook of Chemistry and Physics*, 78th ed., Edited by D. R. Lide (1997-1998).

[15] D. Koutsogeorgis, private communication.

CHAPTER 3: Crystallinity and surface morphology of laser annealed ZnS:Mn thin films grown on Si

I.   INTRODUCTION

In the previous chapter, a simple luminescent structure (800nm of ZnS:Mn deposited on Si), was annealed utilising a commercial KrF excimer laser and it was demonstrated that the photoluminescence signal is linearly enhanced with increasing laser power density. It was suggested that this improvement occurs in the solid state according to the thermal model of the laser processing, and to experimental results of previous work done on similar structures.[1]

The major goals of this chapter are to evaluate the viability of the thermal model for this simple structure of ZnS:Mn on Si, and to investigate the crystallinity and surface morphology produced by both conventional thermal annealing and by the novel pulsed laser annealing process. It is not intended here to strictly compare thermal and laser annealing mechanisms, since treatment times and the physical processes involved are different. However, via a discussion of the resultant effects of these two techniques i.e. the x-ray diffraction and surface morphology characteristics exhibited by the ZnS:Mn thin films, the thermal model can be assessed. The crystallinity and surface morphology of the as-grown and annealed films are investigated using x-ray diffraction (XRD) and atomic force microscopy (AFM) analyses. Also, for a thorough understanding and traceability of the pulsed laser annealing effects, the accurate measurement of impinging optical energy is crucial. Therefore, different commercially available energy-meters have been tested and cross calibrated in order to quantify the absolute laser fluences delivered to the samples.

II.   EXPERIMENTAL AND ANALYSIS CONDITIONS

A. Thin film deposition and thermal annealing

An 800nm thick ZnS:Mn thin film has been deposited onto a n-type single crystal (100) silicon wafer using the growth conditions described in Chapter 2. For reference, the deposition and sputtering target are respectively labelled as NTU228 and P116. (P116 is a commercial ZnS:Mn phosphor-powder, containing 0.45 wt% of Mn, from which a pressed sputtering target is produced.) To examine the effect of post-deposition annealing, the wafer was cleaved into twelve sections ($\sim$1 cm^2 each). This enabled direct comparison of thermal and pulsed laser annealing of samples grown under the same conditions.

Post-deposition thermal annealing was performed on four of the cleaved samples in vacuum (1x10^{-7} T) for 1 hour at temperatures of 400 °C, 500 °C, 600 °C, and at a maximum of 700°C. Limitation to 700 °C was due to thin film losses, by delamination at higher temperatures. During annealing and growth, rotary motion of the samples ensured spatial uniformity of the process.

B. Laser annealing

TITANIA, a high power KrF laser facility at the Rutherford Appleton Laboratory (RAL) was used for large area irradiation, delivering up to 220 mJ/cm^2 via the combination of three 120 mm diameter beams (Fig. 1). The three main beams were used to focus six 50 mm diameter sub-beams onto the wafer, and a 2 cm x 2 cm aperture at the target plane was used to provide uniform beam characteristics over this area of irradiation that is suitable for XRD analysis. A range of fluences is obtained by selecting 1 to 6 sub-beams.

Essential for this experiment is the quality of the beam and associated diagnostics. Figure 1 shows the optical arrangement for irradiation and laser beam diagnostics, i.e. for measurement of the beam uniformity, energy, and pulse duration (~20 ns).
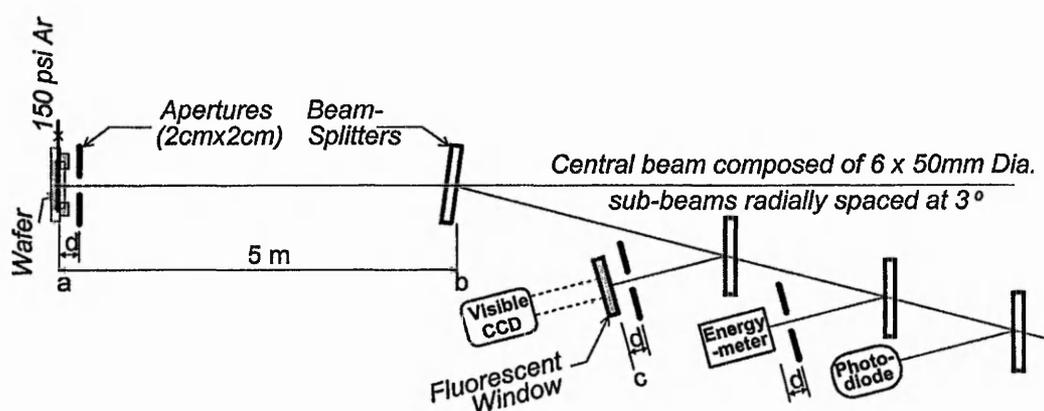
FIG. 1. Experimental arrangement for large area pulsed KrF laser irradiation using TITANIA Facility.

C. Laser beam diagnostics and calibration

On-line diagnostics were performed using four beam-splitters (Fig.1). Each beam-splitter is a fused silica plate that transmits ~92% and reflects ~8% (Fresnel reflections) of the incident beam. The Beam uniformity is determined via a CCD camera imaging system and a window that fluoresces when excited by UV light. Since the beam impinging on the wafer is the result of focusing, the optical paths (ab) and (bc) were set to be equal (Fig.1). The spatial uniformity of the energy distribution was determined to be better than ±10%. The temporal duration (τ_p) of the pulse was measured with a vacuum photo-diode and a digital storage oscilloscope. Small shot to shot variations in τ_p (~16%) and in the detailed pulse shape arise from variations in the output of the discharge laser, which provides the initial pulse for amplification, and from differences between the six beams, which lead to a dependence of the pulse shape on the number of beams being used.

Accurate and absolute measurements of impinging optical power density are critical for traceability, reproducibility, and a thorough analysis. This is a non-trivial problem for optical power densities of the magnitude investigated here, and cross calibration of energy meters is essential. Therefore, three commercially available energy-meters have been tested for this particular experiment: a Gentec ED200, a Scientech no. 103, and a Molectron J50. Using the on-line arrangement, calibration and comparison of the three energy meters was performed by substituting the wafer with the Scientech, the Gentec with the photo-diode and placing the Molectron at the energy-meter position. Consequently, direct comparison between each meter was possible on a single pulse irradiation.

Assuming 92% transmission of the beam splitters and pressure cell quartz window, the theoretical ratios between the signals measured on each of the energy meters are: Scientec/Molectron = 143.75 and Scientec/Gentec = 169.84. From the calibration system described previously, the measured mean ratios obtained with three different energy densities were Scientec/Molectron = 145.88±3 and Scientec/Gentec = 178.17±3. The Molectron and Scientech energy-meters agree well with the theoretical value of 143.75 (assuming perfect beam splitters). The Molectron was chosen for the pulsed laser annealing experiments owing to its high sensitivity at low detection levels, and compatibility with the Scientech system.

Table I summarises the energy-meter cross calibration results. The Scientech is taken as reference since it measures the energy directly impinging on the wafer. In this particular experiment, the Gentec meter consistently gave results between 10 and 25% higher than those measured via the other two meters. Hence, for the results presented here, the energy densities reported are those determined via the Molectron placed at the energy meter position as shown in Fig.1. A list of the measured irradiation fluences (area = 4 cm^2) and pulse duration with corresponding power densities (P_d), obtained by blocking one to five beams, is given in Table II.

TABLE I. Summary of the energy-meter cross calibration. "Relative measure" is the percentage difference between expected and experimental values.

Energy-meter	Sensitivity (mV/J)	Relative measure (%)
Scientec power-meter (serial no.103)	2.05	100
Molectron J50	2000	100
Gentec ED-200	9290	122.2

TABLE II. Results of incident laser energy (E) and pulse duration (τ_p) measurements and calculated energy density (E_d) with corresponding impinging laser power density (P_d).

E (J)	0.87	1.21	1.41	1.44	1.77	1.94	2.13
E_d (mJ/cm^2)	217	304	353	362	443	485	534
τ_p (ns)	20.16	19.7	22.5	23.3	21.1	22	22
P_d (MW/cm^2)	10.76	15.43	15.68	15.53	20.99	22.04	24.27

D. Crystallinity and surface morphology analysis

X-ray diffraction analyses were performed to investigate the crystallinity of the phosphor films, before and after annealing, using reflections from the CuKα_1 emission line (wavelength = 0.15405981 nm) into a Siemens D5000 diffractometer with front monochromator. The applied power of the x-ray tube was 35 KV x 25 mA, the angular step was 0.005° within the studied 25° to 68° range, and the quanta acquisition time was 5 seconds. All diffraction lines characteristics were obtained by a deconvolution programme using the Laurenzian approximation.

Surface morphologies of the as-grown, thermal and laser treated samples were studied via atomic force microscopy analysis, in contact mode, using the Nanoscope III microscope of Digital Instruments. The measurements were performed with no prior chemical etching of the surface.

III. RESULTS

A. Thermal model

Based on the simulation described in Chapter 2, Figures 2 and 3 show respectively the theoretical depth-dependent maximum temperature and the surface temperature transient behaviour of ZnS films deposited on Si substrates. Simulation was performed for fluences of 50, 100, 200, 300, 400, 500, and 610 mJ/cm^2, which compare with the experimental conditions used for laser annealing. Using constant values of $\tau_p = 20$ ns, the corresponding power densities delivered may be determined respectively as 2.5, 5, 10, 15, 20, 25, and 30.5 MW/cm^2. Resulting calculated temperature profiles (Fig. 2) exhibit the shapes of an absorbing media (non exponentially decaying), where the penetration depth ($1/\alpha$) of the light is small compared to the thermal diffusion length (L_d) i.e.,

$$1/\alpha < 2(D\tau_p)^{1/2}, \tag{1}$$

where $D = k/\rho C_s$ is the thermal diffusivity, and τ_p is the rectangular laser pulse duration. A direct consequence of this behaviour is the τ_p dependency, stressing the very essential need for accurate measurement of this parameter, as anticipated in the previous section. Using the parameters of single crystal cubic ZnS determined at room temperature ($k = 0.251$ W/cm.K; $C_s = 472$ J/kg.K; $\rho = 4.076$ g/cm^3),[2] with $\tau_p = 20$ ns; the calculated values of penetration depth and thermal diffusion length are respectively $1/\alpha = 30$ nm and $L_d = 1021$ nm.

In the case of an absorbing media, the heat source becomes a surface source and the heat propagation into the thin film is governed by its thermal characteristics. At the interface (Fig. 2), the slope changes of the temperature profiles are not clearly defined, highlighting that the Si wafer acts like a very soft heat sink. The theoretical temperature at the phosphor / substrate interface calculated for the whole experimental range of laser power density values i.e. from 10.76 to 24.27 MW/cm^2 (< 500 mJ/cm^2) is lower than 650 K (~380 °C).
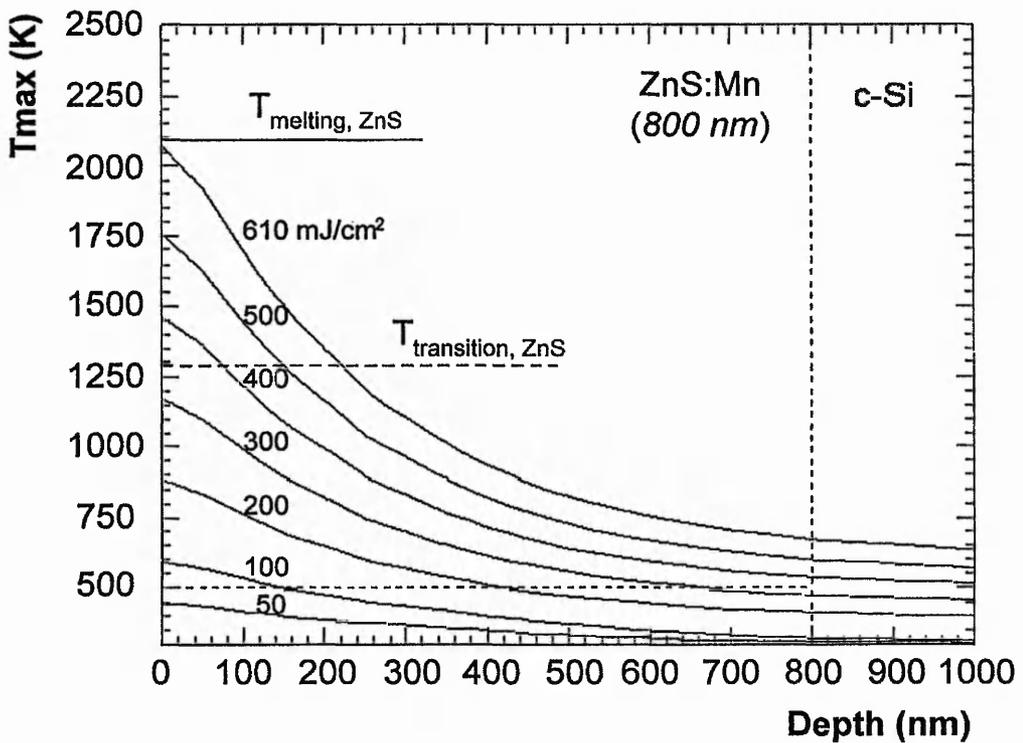
FIG. 2. Theoretical maximal temperature distribution profile as function of depth into 800 nm ZnS:Mn film deposited onto a Si wafer during irradiation with a 20 ns pulsed KrF excimer laser at various fluences.

Figure 3 highlights the simulated time-dependence of the surface temperature. Especially shown are the short heating and cooling times involved under various laser fluences, owing to the short irradiation time (~20 ns). For example, when irradiation conditions for the cubic to hexagonal phase transition is reached i.e. $T_{surface} = T_{transition}$, the curves drop quickly below the transition temperature.
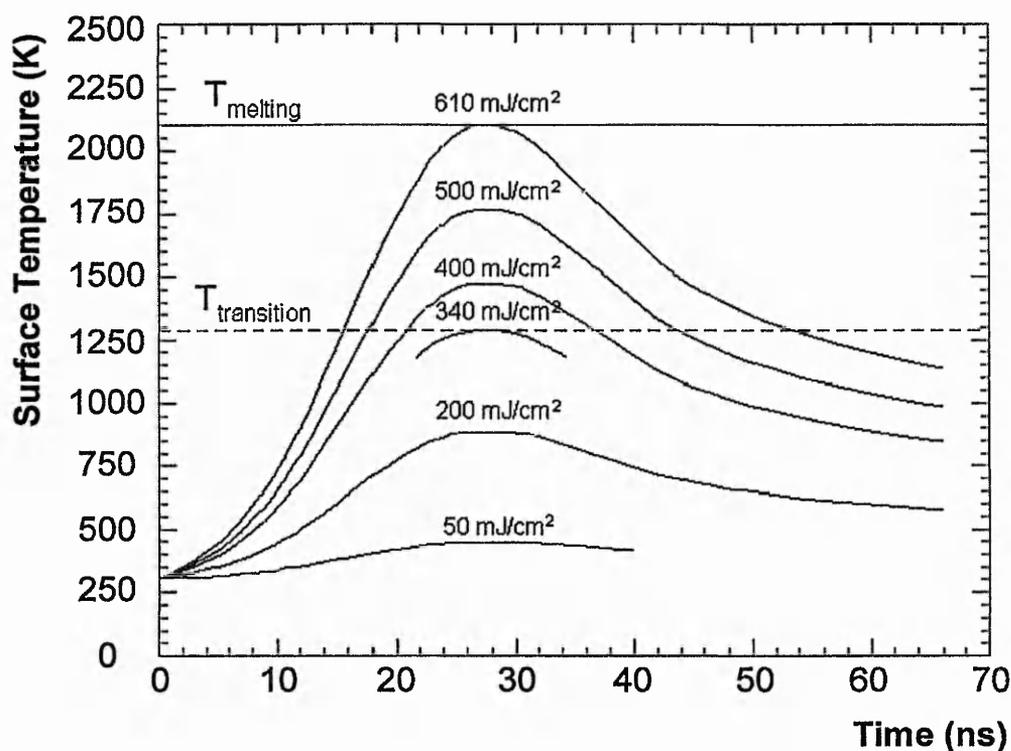
FIG. 3. Time dependent surface temperature profile of 800 nm ZnS:Mn film deposited onto a Si wafer during irradiation with a 20 ns pulsed KrF excimer laser at various fluences.

Figure 4 represents the effective time and effective transformation depth corresponding to values for $T_{surface} >= T_{transition}$. From about 20 MW/cm^2, the effective transformation time increases linearly up to the melting threshold and its value stays below 40 ns. The simulation indicates also that under the solid state conditions, the sphalerite to wurzite transformation should be confined within the first 250 nm of the ZnS:Mn thin film.
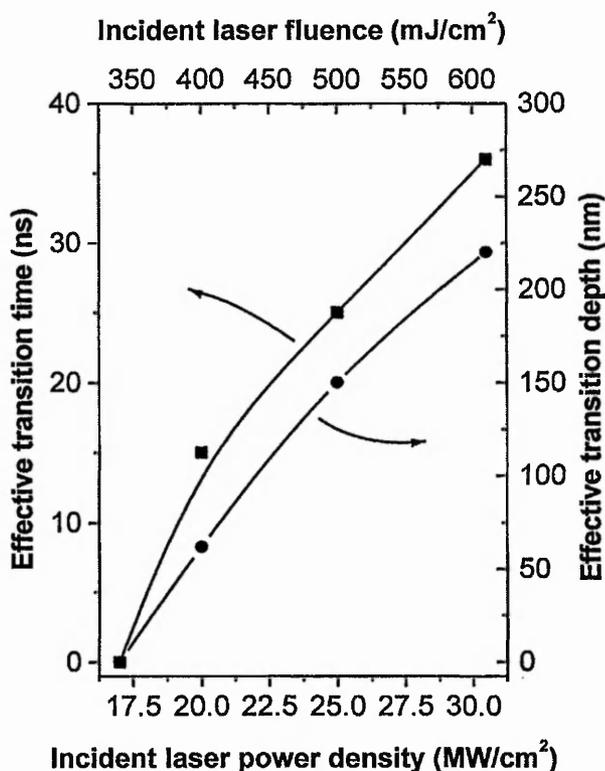
FIG. 4. Effective transition time and effective transition depth for sphalerite-wurzite transformation as function of incident laser power density and corresponding laser fluence. Curves are generated by computer algorithm and are included for clarity.

B. The crystallinity dependence on annealing conditions

Figure 5 shows the measured XRD patterns of non-annealed (NA), thermally annealed (700 °C) and pulsed laser annealed samples at various power densities (10.76 MW/cm^2, 15.53 MW/cm^2, 20.99 MW/cm^2, 22.04 MW/cm^2, 24.27 MW/cm^2). Due to the long deposition time, the as-grown sample is considered to be effectively annealed thermally at the 200 °C substrate temperature used during growth.

All the observed diffraction lines are identified in Table III. Line 9 represents the (400) reflection from the *c*-Si substrate that has not been fully measured [Fig. 5a] to avoid saturation of the detection system. Each of the lines 1,5, and 7 are made up of two unresolved lines from planes of nearly the same spacing and indicative of both cubic and hexagonal phases. Lines 2, 4, and 6 are distinctive of respectively (10.1), (10.2) and (10.3) hexagonal planes and line 3 involves the (200) plane reflections representative of only the cubic ZnS structure. It seems worthwhile to note that although the diamond and the sphalerite structures are geometrically identical, being both face centred cubic, the (200) reflection is forbidden in silicon owing to its higher symmetry, i.e. all atoms are the same.[3]
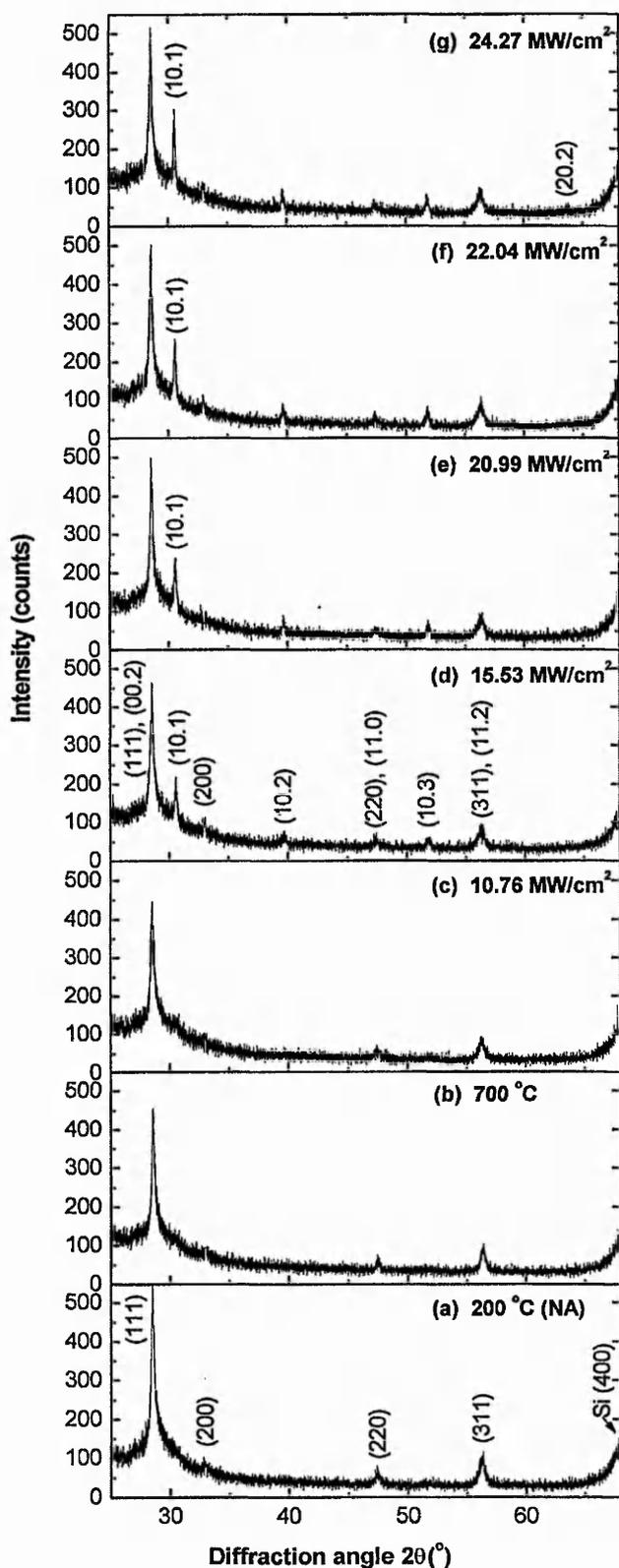
FIG. 5. XRD patterns of samples as deposited (NA) at 200 °C (a), thermally annealed at 700 °C (b), and pulsed laser annealed under incident laser power densities of 10.76 MW/cm² (c), 15.53 MW/cm² (d), 20.99 MW/cm² (e), 22.04 MW/cm² (f), and 24.27 MW/cm² (g).

TABLE III. Noticeable diffraction lines in XRD patterns corresponding to calculated diffraction angles ($2\theta_{cal}$) from α-ZnS (sphalerite), β-ZnS (wurzite), and Si. Lattice parameters in nm and established at 300K.

Lines	α-ZnS $(a = 0.54102)$[4]		β-ZnS $(a_{2H} = 0.38226, c_{2H} = 0.62605)$[5]		Si $(a = 0.5431)$[2]	
	hkl	$2\theta_{cal}$ (°)	*hkl*	$2\theta_{cal}$ (°)	*hkl*	$2\theta_{cal}$ (°)
1	111	28.56	00.2	28.49		
2			10.1	30.52		
3	200	33.09				
4			10.2	39.59		
5	220	47.50	11.0	47.53		
6			10.3	51.74		
7	311	56.36	11.2	56.36		
8			20.2	63.53		
9					400	69.13

Unfortunately, the ZnS (200) peak is too weak to quantitatively compare the two main ZnS structures for the absence of an analysable pure cubic line as reference. However, the lack of diffraction from any hexagonal planes denote that as-grown and thermally annealed ZnS:Mn structures are and remain predominantly cubic [see Figs 5(a) and 5(b)]. Consequently, the observed diffraction peaks are all attributed to the cubic forms i.e. (111), (220), and (311). Analysis of their diffraction characteristics do not reveal significant grain growth or reorientation which is in agreement with previous work.[6]

XRD patterns of samples exposed to laser irradiation with optical power density greater than 10.76 MW/cm^2 [see Figs. 5(d) to 5(g)] exhibit pronounced cubic to hexagonal transformation via the appearance of the hexagonal (10.1), (10.2) and (10.3) lines.

Since the diffraction lines 1, 5, and 7 (Table III) corresponding to both allotropes are difficult to attribute to one or the other form, their diffraction characteristics have not been studied. Nevertheless, by examining their intensity ratios as a function of laser power, the effect of pulsed laser annealing on both crystalline structures can be compared. It is observed that the intensity ratios of purely hexagonal lines to unresolved lines $I_{10.1}/(I_{00.2}, I_{111})$, $I_{10.3}/(I_{11.2}, I_{311})$, $I_{10.2}/(I_{00.2}, I_{111})$, and $I_{10.3}/(I_{00.2}, I_{111})$, represented by the solid lines in Figure 6 increase with laser power density. This demonstrates that the thin film becomes more hexagonal with increasing power density and that transformation occurs by reduction of the cubic structure.

Also shown on Fig. 6, is the plot of the ratios of purely hexagonal lines, $I_{10.2}/I_{10.1}$; $I_{10.3}/I_{10.2}$ and $I_{10.3}/I_{10.1}$, against laser power density. The decrease of these values with increasing laser power density suggested that the preferential wurzite growth orientation is determined by the planes of lower indices.
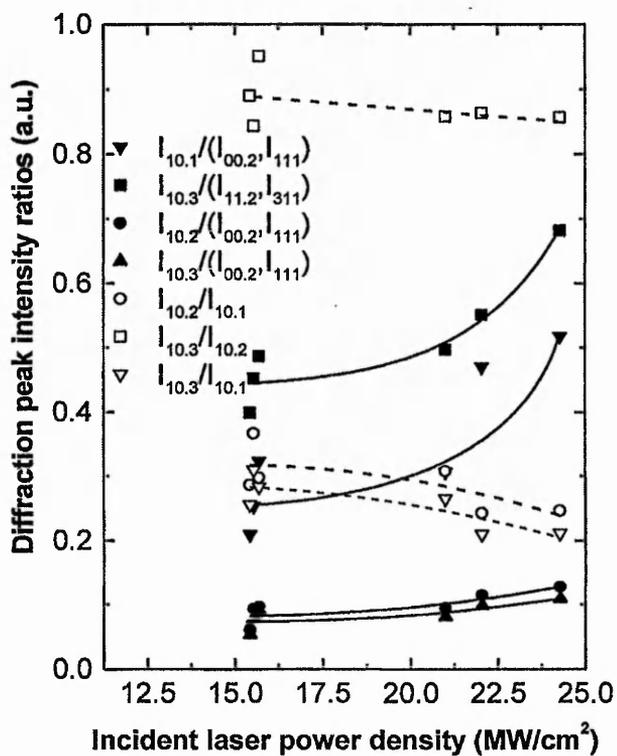
FIG. 6. Intensity ratios of purely hexagonal lines and unresolved lines as function of incident laser power density (solid lines). Intensity ratios of purely hexagonal lines as function of incident laser power density (dashed lines). Curves are generated by computer algorithm and are included for clarity.

In Figure 7, the diffraction characteristics of the (10.1) plane are investigated. Between about ~16 MW/cm^2 and ~21 MW/cm^2, the peak intensity $I_{10.1}$ is nearly constant before increasing rapidly beyond ~21 MW/cm^2 while the full width at half maximum (FWHM) and atomic spacing remain unchanged within experimental errors. Evidence of the crystalline quality improvement of the phosphor thin film is clearly recognised under higher irradiation power (> 22.02 MW/cm^2), since a secondary diffraction line can be recognised at around 63.63° [Fig. 5(g)], which corresponds to the (20.2) plane.
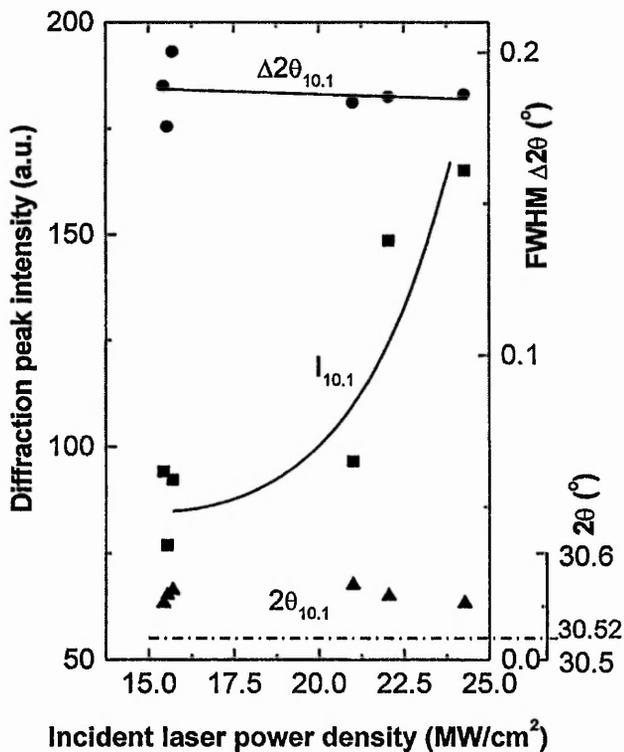
FIG. 7. (10.1) diffraction line characteristics as a function of incident laser power density. Dots = $\Delta 2\theta_{10.1}$ (FWHM), squares = $I_{10.1}$, triangles = $2\theta_{10.1}$. Horizontal axis line corresponds to the calculated diffraction angle in Table III. Curves are generated by computer algorithm and are included for clarity.

C. The surface morphology dependence on annealing conditions

A surface morphology comparison, using atomic force microscopy analysis, between as-grown samples and either thermally annealed or pulsed laser annealed samples is presented in Figure 8. Perspective surface representations of measured surface areas (3 μm x 3 μm) highlight clearly that the surface texture is nearly unchanged using the conventional thermal annealing technique up to a maximum treatment temperature of 700 °C [Fig. 8(b)]. On the other hand, a gradual surface improvement with increasing irradiation energy using pulsed laser annealing processing is displayed in Figs 8(c) and 8(d), which are representative of surfaces being irradiated under laser power densities of 15.68 MW/cm^2 and 24.27 MW/cm^2.

Results of the random mean square (RMS) interpolated over the whole analysed surfaces are also reported. An important reduction in surface roughness is obtained when the sample is irradiated with 24.27 MW/cm^2 of laser power density (RMS = 2 nm) compared to the as-grown (RMS = 10 nm) or thermal annealed (RMS = 12 nm) thin film. The top view of the sample with RMS = 2 nm (Fig. 9) is particularly interesting since the six sides of the hexagonal crystallites are clearly distinguishable. An average measurement of the hexagons mean-size is approximately 113 nm.

(a) Non-annealed.

RMS = 10 nm

(b) Thermally annealed (700 °C).

RMS = 12 nm

(c) $P_d = 15.68$ MW/cm^2.

RMS = 5 nm

(d) $P_d = 24.27$ MW/cm^2.

RMS = 2 nm
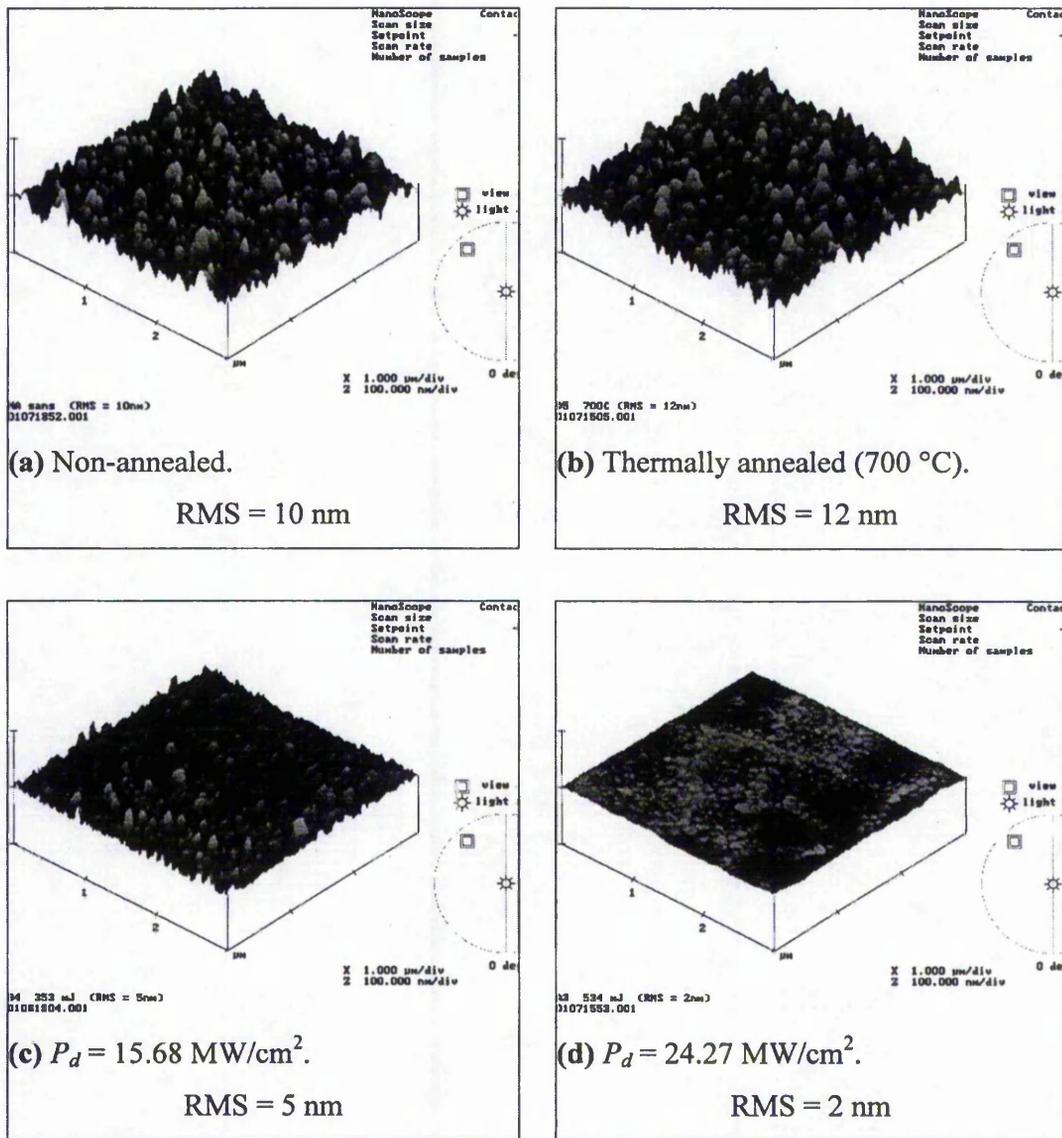
FIG. 8. Perspective representation of atomic force microscopy images of samples as-grown (a), thermally annealed at 700 °C (b), and pulsed laser annealed under 16.68 MW/cm^2 (c), and 24.27 MW/cm^2 (d) irradiation power density (P_d).
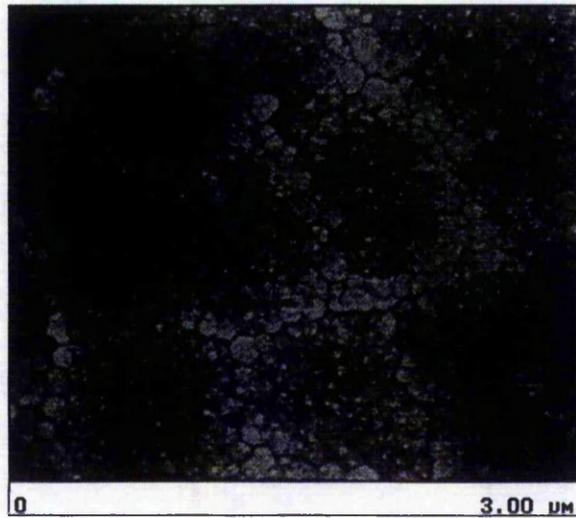
FIG. 9. Atomic force microscopy image (top view) of the pulsed laser annealed sample with 24.27 MW/cm^2 of irradiation power. Hexagonal crystallite shapes are clearly distinguishable within the 3 μm x 3 μm examined surface.

IV. DISCUSSION

A. Allotropic transition

As a general rule, it is often found that valence-bound solids can crystallise in several different structures for almost the same cohesive energy resulting in allotropic materials. For ZnS, the various crystalline forms obtained can all be maintained at room temperature without apparent risk of spontaneous conversion to the energetically most favoured one.[7] Thus, ZnS can exist at 300 K either in the zinc blende or wurzite form. That property is clearly highlighted by laser annealed samples that show hexagonal structures while thermal annealed samples exhibit preferentially the (111) oriented cubic structure.

The major difference in the XRD patterns of laser and thermal annealed samples is the formation of the wurzite structure, which is the most stable allotrope at high temperatures. This suggests strongly that the temperatures involved via laser processing exceed those of the conventional thermal treatment (in vacuum), which were limited to 700 °C due to delamination. Simulation of the maximal surface temperature attained using the lowest power density of 10.76 MW/cm^2 suggests an effective surface annealing temperature of ~660 °C, which conforms to the observed crystallographic structures (Fig. 5).

The diffraction peak intensities, corresponding to either the cubic or hexagonal structures, are indicative of the number of participating planes responsible

for constructive interference. Analysis of the (111) diffraction peak for samples thermally annealed at temperatures from 200 °C (as-grown) to 700 °C does not show significant variation in intensity, hence suggesting that the number of cubic crystallites remains unchanged within the phosphor layer.

However, the diffraction intensities of the (10.1), (10.2), and (10.3) hexagonal planes, "formed" by laser annealing, are increased with the enhanced irradiation power, and two distinctive formation rates (hexagonal peak intensity increase / laser power density increase) are observed below and above 21 MW/cm^2 (Figs. 6 and 7). More precisely, the cubic to hexagonal transformation appears to be stabilised from 16 MW/cm^2 to 21 MW/cm^2 and catalysed beyond and up to 24.27 MW/cm^2.

The stable transformation region is attributed to the small difference between the lattice formation energies of the two main crystalline forms i.e. cubic face-centred (sphalerite) and hexagonal close packing (wurtzite). It is supposed that the latter property becomes predominant when the samples are laser annealed at power densities close to the phase transition threshold. Also, the spatial and transient temperature distribution within the phosphor layer is non-homogeneous (Figs. 2 and 3). Therefore, neither structure is expected to have precedence in its formation, thus leading to the observed stable transformation region below 21 MW/cm^2. Confirmation of this hypothesis may be inferred from the work of Addamiano and Aven[8] who investigated the stability of pure hexagonal crystals (grown from the melt), and the transformation of the cubic zinc-blende structure. Indeed, they observed that within the temperature interval of 700 °C - 1150 °C, no full conversion

to the cubic phase was achieved.

The first hexagonal lines were detected for laser annealed samples at power densities between 10.76 MW/cm^2 and 15.43 MW/cm^2, which is below the simulated phase transition threshold of 17 MW/cm^2. Remember however that this simulated value was determined using the optical and thermal parameters of single crystal ZnS. Moreover, for polycrystalline thin films, as studied here, we would not expect such a sharp transition since the binding energies between atoms are less well defined. Evidently, the same is valid for the melting temperature and hence we expect a similar shift even without considering localised melting at grain boundaries. Nevertheless, according to the model, solid state and solid-liquid transitions are expected to occur respectively in the regions of 17 MW/cm^2 and 30.5 MW/cm^2. The fact that the calculated transition threshold lies within the stabilised transition region is encouraging for the viability of the model.

Within the whole laser power density range examined in the present study, the FWHM ($\Delta2\theta$), indicative of average grain size, remains constant (Fig. 7). Therefore, we attribute the increase in the formation rate of hexagonal planes to enhanced transformation within the thickness of the film. This would be consistent with the maximal temperature vs. depth simulation (Fig.2) and with the behaviour of the effective transition depth (Fig.4). Results plotted in Fig. 4 suggest also that the effective transformation time using our laser annealing conditions is less than 40 ns. This result combined with the FWHM studies suggest that the laser processing used is too fast to facilitate grain growth and that transformation occurs in the solid state without generation of a melting front. Note that the effective transformation time is

correlated to depth-temperature profiles and in-depth transformation rate. Furthermore, a recent thermal annealing study of ZnS thin films on sapphire exhibited significant cubic grain growth by annealing at temperatures of ~900 °C during periods >10 hours.[9] Hence, this is further evidence that our laser processing is too fast for grain growth since the laser generated temperatures within the phosphor film are undoubtedly greater than in the latter study as evidenced by the crystallographic transition ($T_{transition}$ = 1295 K).

Under some assumptions of the crystalline quality, the average crystal dimension L_c perpendicular to the reflecting planes may be determined using the Sherrer equation[10]

$$B(2\theta)=0.94\lambda/L_c\cos\theta. \tag{2}$$

Where $B(2\theta)$ is the full width in radians subtended by the half maximum intensity width of the pattern peak, λ the x-ray wavelength, and θ half of the diffraction angle.

Using Equ. (2), the average wurzite crystallite size within the 800 nm thin film has been calculated to be ~47 nm. A similar average grain size calculation of the non-annealed or thermally annealed cubic structures gives ~31nm. Note that an intrinsic increase of the crystallite dimension from the phosphor / substrate and throughout the phosphor layer is expected due to its non-uniform microscopic columnar nature.[11] This deposition characteristic would explain the bigger wurzite crystallite size since they are formed in the upper part of the ZnS:Mn thin film.

B. Surface morphology improvement

AFM analysis highlights that the cubic to hexagonal phase transformation induced a gradual surface morphology improvement of up to a factor of five, while the unaltered cubic form (non and thermally annealed) remained essentially unchanged. Similar surface improvements related to crystalline quality and reorientation were reported when pseudo-epitaxial ZnS films were grown on differently oriented Si substrates,[12,13] indicating that surface quality is directly related to crystalline ordering within the thickness of the thin film. Also demonstrated[12] was that the best single crystal films were obtained with a Si (100) substrate, which was also used for the present study.

The emergence of the hexagonal crystallite shapes at the surface, when the sample has been annealed at 24.27 MW/cm^2 (Fig. 9), result possibly from the well-oriented hexagonal structure (appearance of a secondary reflection peak in the diffraction pattern), and from the migration of voids and other defects to the column boundaries. Additionally, slight material removal via single pulse laser ablation is likely to occur under our laser annealing conditions.[14] Hence, it is possible that the supposed material loss may also take part in the surface smoothing effect.

V. CONCLUSIONS

As grown and thermally annealed phosphors up to 700 °C exhibit the zinc blende form. Using the novel pulsed laser annealing technique, it is suggested that allotropic transition from the cubic to hexagonal phase occurs between 10.76 MW/cm^2 and 15.43 MW/cm^2 of applied laser power density, i.e. below the calculated transition threshold of 17 MW/cm^2. Both the threshold shift and dual formation rate behaviour, as opposed to a sharp transition, may be explained by the polycrystalline nature of the as-grown film, the small difference in lattice formation energies of the two main crystalline forms, and the non-homogenous spatial and transient thermal distribution into the thin film. Also, it is important to emphasise that the simulations were performed based on the properties of single crystal ZnS for which the full range of optical and thermal parameters are known in its solid state phase, since such comprehensive data does not exist for polycrystalline thin films.

From XRD analysis, the FWHM related to crystallite size remains constant using both annealing techniques. Considering the processing temperatures and time factors involved, it is inferred that the pulsed laser annealing processing time is insufficient to increase the crystallite size and that allotropic transition occurs in the solid state. Hence, it is concluded that the intensity increase of the hexagonal close packed plane reflections is due to enhanced in-depth transformations, which correlates to the simulated in-depth temperature profiles generated during laser processing.

Finally, AFM analysis suggests that a gradual surface smoothing is concomitant to the phase transition.

REFERENCES

[1] H. S. Reehal, J. M. Gallego, C. B. Edwards, Appl. Phys. Lett. **40**, 258 (1982).

[2] *Handbook of Chemistry and Physics*, 78th ed., edited by D. R. Lide (1997-1998).

[3] D. B. Cullity, *Elements of X-ray Diffraction*, (Addison-Wesley, Reading, MA, 1978).

[4] J. C. Jamieson and H. H. Demarest, J. Phys. Chem. Solids **41**, 963 (1980).

[5] R. R. Reeber and G. W. Powell, J. Appl. Phys. **38**, 1531 (1967).

[6] A. F. Cattel and A. G. Cullis, Thin Solid Films **92**, 211 (1982).

[7] J. S. Blakemore, *Solid State Physics*, 2nd. ed. (Cambridge University Press, Cambridge, 1985), p. 10.

[8] A. Addamiano and M. Aven, J. Appl. Phys. **31**, 36 (1960).

[9] Z. Z. Bandic, E. C. Piquette, J. O. McCaldin, and T. C. McGill, Appl. Phys. Lett. **72**(22), 2862 (1998).

[10] B. E. Warren, *X-ray Diffraction* (Dover, New York, 1990), p. 253.

[11] L. E. Tannas, *Flat Panels Displays and CRTs* (Van Nostrand, Princeton, 1985), p. 260.

[12] T. G. R. Rawlins, J. Mater. Sci. **5**, 881 (1970).

[13] P. L. Jones, C. N. Litting, D. E. Mason, and V. A. Williams, Br. J. Appl. Phys., J. Phys. D **1**, 283 (1968).

[14] W. M. Cranton, P. H. Key, D. Sands, C. B. Thomas, and F. X. Wagner, Appl. Surf. Sci. **96-98**, 501 (1996).

CHAPTER 4: Ablation study on laser annealed ZnS:Mn / Y$_2$O$_3$ multilayers grown on Si

I.   Introduction

The photoluminescence and structural studies performed on laser and thermally annealed ZnS:Mn phosphors individually deposited on Si provided valuable knowledge of the laser annealing process and about the phosphor itself. Briefly, according to the results of Chapters 2 and 3, the pulsed laser treatment is a technique that heats the phosphor layer locally for very short times, and improves its luminescent properties during allotropic transformation.

The further step is now to use this novel annealing technique to process TFEL structures and perform electroluminescence analyses. However, to successfully transfer this technology to electroluminescent applications, it is essential to preliminary define the parameters which are needed to anneal the phosphor thin films with no, or minimal ablation.

As shown in Chapter 1, the basic TFEL structure is composed of a phosphor thin film sandwiched between two insulator layers. In the early stages of this PhD work, such full TFEL stacks, i.e., Y_2O_3 (300 nm) / ZnS (800 nm) / Y_2O_3 (300 nm) on Si, were laser processed using the experimental arrangements described in Chapters 2 and 3. Results of photoluminescence and surface profile measurements showed that before any luminescent improvement threshold was reached, the whole 300 nm thick upper dielectric layer was removed after single pulse irradiation. Since Y_2O_3 is transparent to KrF irradiation, $E_{g,Y2O3} \sim 6.0$ eV,[1] the total loss of the upper layer was attributed to the high phosphor surface temperatures attained during laser annealing

as described by the thermal model. Also, it is reasonable to think that the interfaces are the mechanically weakest points of a typical TFEL structure. Hence, it is believed that the upper interface breaks due to the generation of high temperature gradients, leaving the phosphor layer uncoated. Therefore, in the remaining laser annealing experiments, the phosphor layers will be laser annealed prior to upper insulator deposition.

The results of Chapter 2 suggest that the number of active luminescent centres within ZnS:Mn can be further increased by laser annealing the phosphor layer several times. Thus, the aim of this Chapter is to analyse and discuss the effects of multiple irradiation shots at various power densities on the laser ablation of a TFEL base layer, i.e. a stack of 800 nm of ZnS:Mn and 300 nm of Y_2O_3 thin films. Also considered is the evaluation of the remaining phosphor thickness obtained under the various annealing conditions since film thickness is directly related to electroluminescent characteristics of the fabricated devices e.g. threshold voltage and brightness.

The results of the thermal simulation based on single shot laser irradiation of the studied base layer are also presented for a better understanding of the ablation characteristic involved.

II. Experimental

A thin film of Y_2O_3 (300 nm) and a second layer of ZnS:Mn (800 nm) were successively sputtered onto a 4 inch (100) Si wafer-substrate using the growth conditions described in Chapter 2.

Laser processing was carried out using the arrangement shown in Chapter 2 and irradiation were performed under a static argon pressure of 150 psi. The impinging power density range varied from 8 MW/cm^2 (160 mJ/cm^2) to 49 MW/cm^2 (980 mJ/cm^2) with steps smaller than 5 MW/cm^2 (100 mJ/cm^2). The number of shots on single target areas varied from 1 to 20 with time delays between consecutive pulses longer than one second, ensuring complete thermal relaxation of the target.

Ablation depths were measured from the non laser-treated surface (as-grown) to the centre of the irradiated regions using a Tencor PII profilometer.

III. Thermal simulation of the laser processing

The thermal model of the KrF laser processing has been partially validated on the simple structure based on silicon coated with an 800 nm layer of ZnS:Mn (Chapters 2 and 3). The same model is used in the present study to obtain the maximal transient temperatures attained within the TFEL base layer. The optical and thermal parameters used for the simulation are listed in Table I. It is assumed that the as-grown polycrystalline ZnS:Mn and Y_2O_3 layers possess the same properties as the zinc blende ZnS and body centred bixbyite Y_2O_3 single crystals, respectively.

TABLE I. Parameters used to solve the one-dimensional thermal model. Thermal and optical properties are determined respectively at 300 K and for a 248 nm irradiation wavelength. R represents the reflectivity at normal incidence, α the optical absorption coefficient, k the thermal conductivity, C_s the specific heat, and ρ the density. $T_{transition}$ is the necessary temperature for the phase transition from the cubic to the hexagonal forms of the corresponding materials. (*) Values calculated using the real and imaginary parts or the refractive index of respectively 2.155 [2] and 5.6×10^{-6} [3].

	c-ZnS	c-Y_2O_3	c-Si [4]
R (⊥ to surface)	0.27 [5]	0.134 (*)	0.665
α (cm^{-1})	3.33×10^5 [5]	2.826 (*)	1.7×10^6
$T_{melting}$ (K)	$2100^{\pm 20}$ [6]	2710 [7]	1683
$T_{transition}$ (K)	1295 [8]	2640 [7]	-
$T_{sublimation}$ (K)	~1273 [9] (estimated value)	-	-
k (mW/cm.K)	251 [10]	133 [11]	1400
C_s (J/kg.K)	472 [10]	455.65 [12]	745
ρ (g/cm^3)	4.079 [10]	5.033 [1]	2.32

IV. Results

A. Thermal model

Figure 1 shows the spatial behaviour of the maximum temperatures reached within the stack of ZnS:Mn and Y_2O_3 layers after a single pulse laser irradiation of 20 ns.
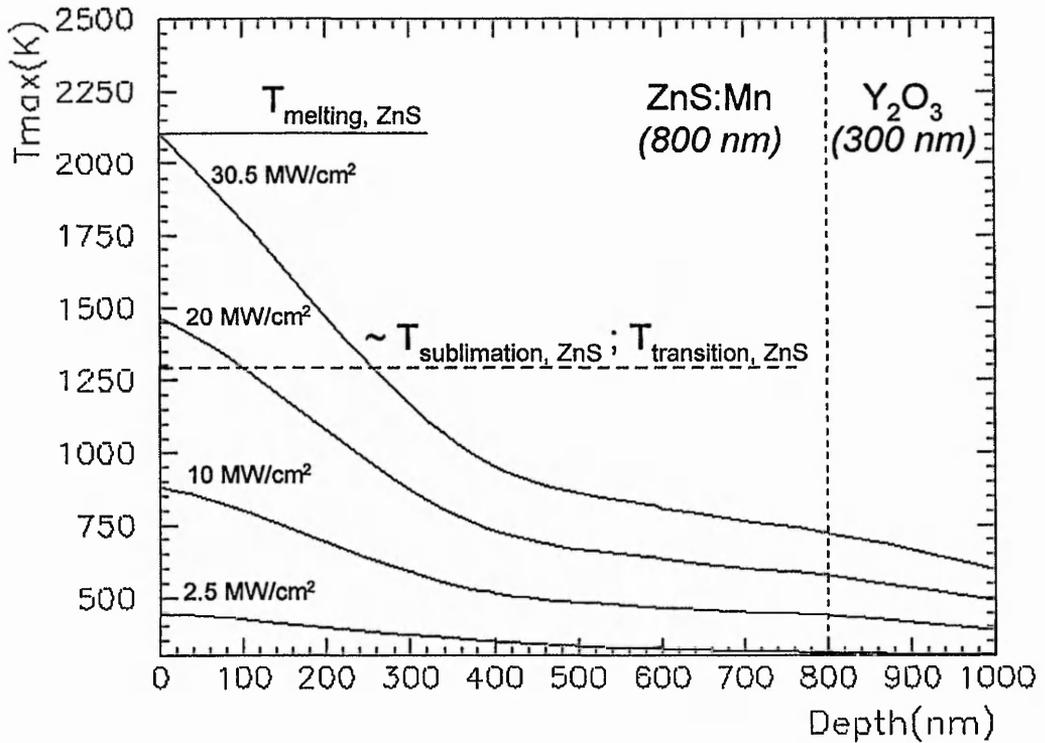
FIG. 1. Simulated maximal temperature distribution profile as a function of depth, for 800 nm thick ZnS:Mn and 300 nm thick Y_2O_3 thin films successively deposited onto a Si wafer, after a single irradiation from a 20 ns pulsed KrF excimer laser at various power densities.

From the data reported in Table I, surface temperatures of the phosphor layer corresponding to sublimation, cubic to hexagonal transition, and melting are estimated to be attained during laser annealing at power densities of, respectively, ~16.6 MW/cm^2, 17 MW/cm^2, and 30.5 MW/cm^2 (Fig. 1).

Note that the results of thermal modelling are unchanged whether simulating the laser irradiation in air at atmospheric pressure, or under 150 psi of Ar. The respective thermal conductivity of both target environments, determined at 300 K are: $k_{air\,(1\,bar)}$ = 0.261 mW/cm.K, and $k_{Ar\,(10..34\,bars)}$ ~0.26 mW/cm.K.[13,14]

B. Ablation depth and ablation rate analyses

The profile analysis of the laser processed regions did not highlight any material removal when 1 to 20 pulses were used at power densities of 8 MW/cm^2 or 15 MW/cm^2 and significant measurable ablation occurred only after three pulses of 20 MW/cm^2. Note that using the Tencor PII detection system, no significant ablation was measured using single pulses up to 38 MW/cm^2. From 38 MW/cm^2 to 49 MW/cm^2, the removed thickness was smaller than 80 nm.

Figure 2 shows the typical form of a profilometer scan measured across the centre of an ablated region. Scanning over the whole irradiated area showed that the ablated region has the form of a pit surrounded by a rim above the as-deposited surface (non laser processed). A geometrical calculation using the rim cross section (Figure 2) shows that it contains ~80% of the removed volume.
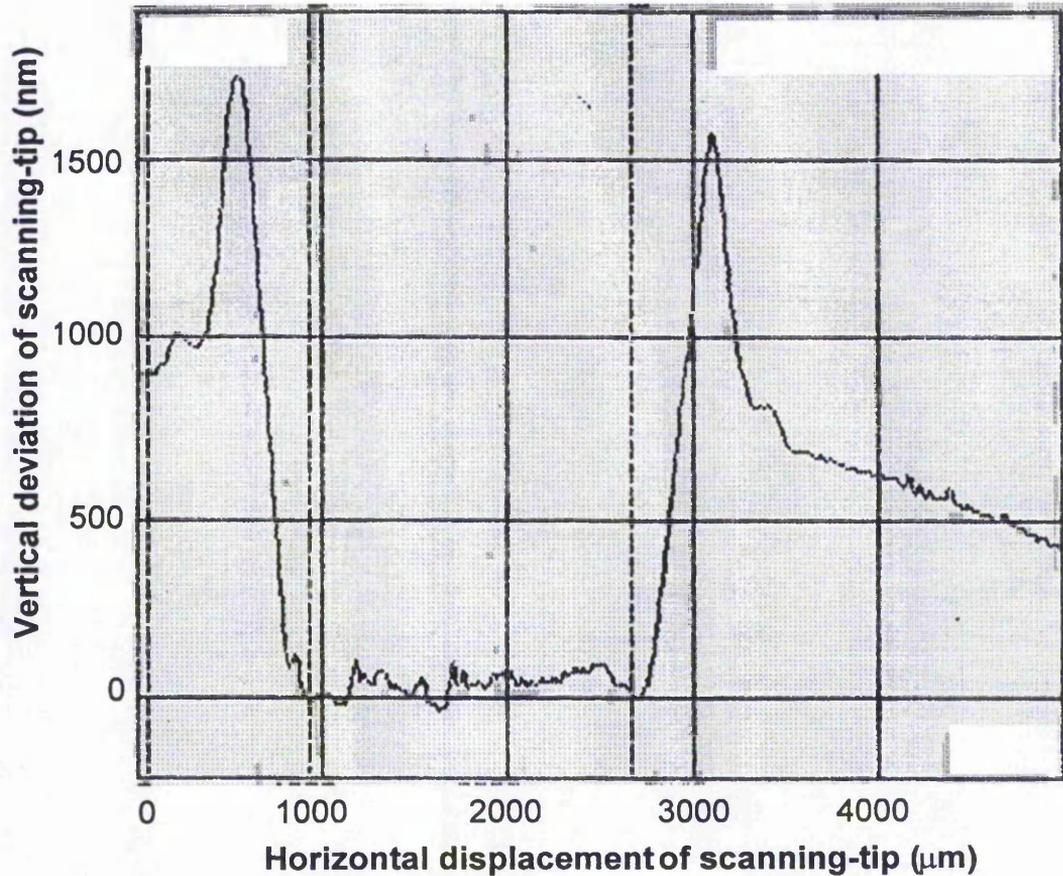
FIG. 2. Profilometer scan of a laser treated area with 20 pulses of 41 MW/cm^2. The observed rim surrounding the pit (shown in cross section) contains ~80% of the volume removed below the as-deposited surface.

Figures 3 and 4 represent the depth of material removed and the ablation rate (thickness of material removed per pulse) obtained with 3 to 20 shots of various laser power densities, respectively.
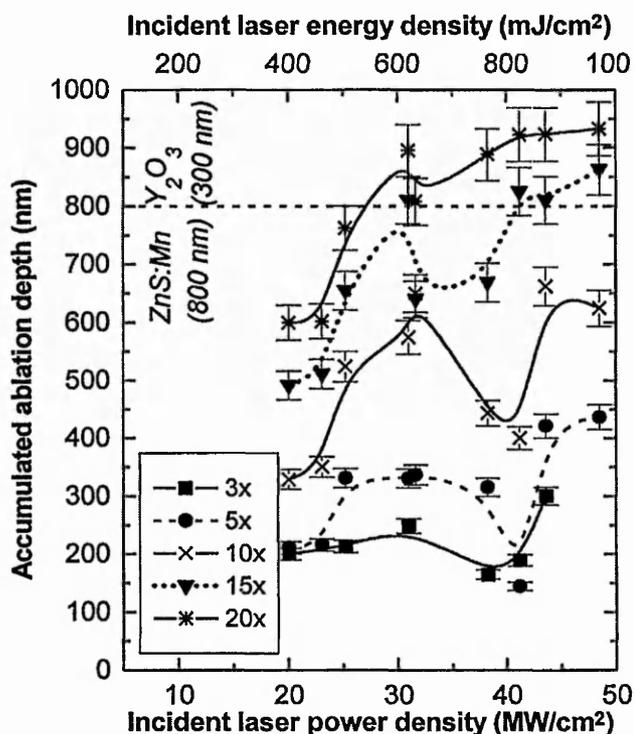
FIG. 3. Cumulative ablated depth plotted against the incident laser power density at a range of pulse numbers for a stack of 800 nm of ZnS:Mn and 300 nm of Y₂O₃. Curves for each specific number of pulses (3x, 5x, 10x, 15x, 20x) are fitted by B-splines and drawn for clarity.
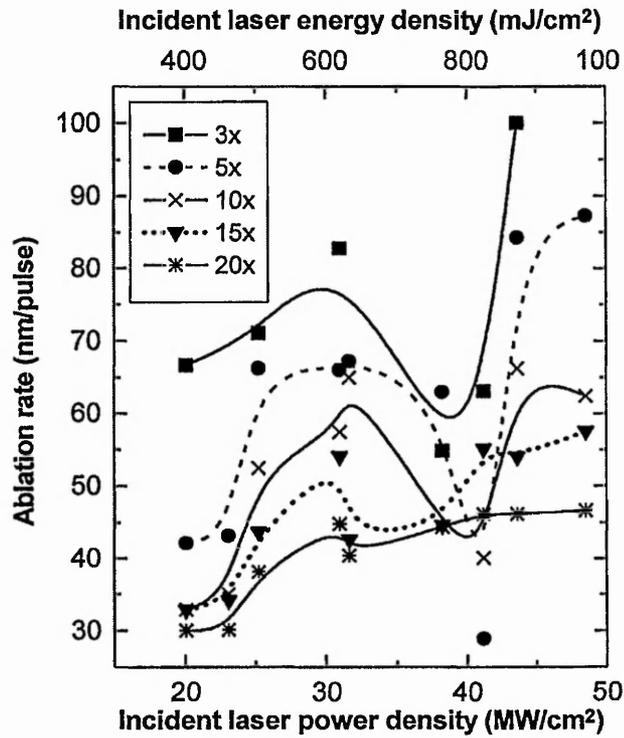
FIG. 4. Ablation rates as function of incident laser power density and energy density at a range of pulse numbers for a stack of 800 nm of ZnS:Mn and 300 nm of Y_2O_3. Curves for each specific number of pulses (3x, 5x, 10x, 15x, 20x) are fitted by B-splines and drawn for clarity.

In Figures 3 and 4, all the data representing a specific pulse number configuration i.e. 3x, 5x, 10x, 15x, or 20x, are quasi-constant from 20 MW/cm^2 to 23 MW/cm^2 before increasing to a maximum at ~31 MW/cm^2. Above ~31 MW/cm^2, a minimum is reached at ~40 MW/cm^2 for 3 to 10 pulses, which is shifting to ~32 MW/cm^2 at higher pulse repetitions.

Exceeding those minima, the accumulated ablated depth (Fig. 3) and ablation rate (Fig. 4) increase again with increasing laser power densities up to ~43 MW/cm^2. In Figure 3, it is interesting to note that up to 5 shots, the total depth removed under 20 MW/cm^2 is smaller than when nearly twice the power density is used, i.e. 41 MW/cm^2. Similarly, the whole 800 nm thick phosphor layer can be removed with 15 irradiations at 31 MW/cm^2 and only 640 nm with slightly higher power density, i.e. 32 MW/cm^2.

Figure 4 shows that, at constant laser power densities, the ablation rate decreases with number or pulses. Exceptions arise at around 40 MW/cm^2 where minima of lower and higher shot numbers do not overlap. Note that all minima and maxima described above are also exhibited when the ZnS:Mn thin film has been completely removed (see Fig. 3 curve 20x) since the measured total depth is an integration of the effects of all previous shots.

Results of the averaged ablation rates obtained from the different pulse numbers for various power densities are plotted in Figure 5. The average values have been obtained by (i) plotting the accumulated ablation depths as a function of pulse numbers for various power densities, and (ii) linearly extrapolating the curves to the origin (see example, inset into Figure 5). The slope of a linear interpolation is therefore equal to an ablation rate (averaged from all pulse configurations) for a given value of incident laser power density.

The data shown in figure 5 exhibits similar behaviours as those in Figures 3 and 4, i.e. quasi-constant from 20 MW/cm^2 to 23 MW/cm^2, maximum at ~31 MW/cm^2, and minimum between ~32 MW/cm^2 and ~40 MW/cm^2.

The quasi-constant region (constant ablation rate) and mimima region (reduction of the ablation rate) are attributed to the allotropic transition and melting of ZnS:Mn, which will be discussed in Section V.
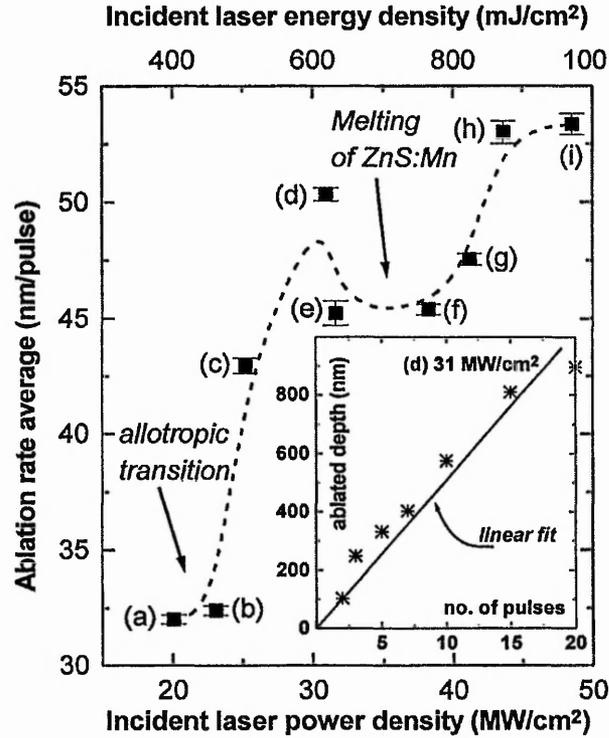
FIG. 5. Ablation rate linearly averaged for all pulse number configurations as function of incident laser power density and energy density. The data correspond to laser irradiations of (a) 20 MW/cm², (b) 23 MW/cm², (c) 25 MW/cm², (d) 31 MW/cm², (e) 32 MW/cm², (f) 38 MW/cm², (g) 41 MW/cm², (h) 43 MW/cm², (i) 49 MW/cm². Error bars correspond to the fitting errors with respect to the experimental values. The two distinctive curvature changes in the B-spline fitted dashed line are related to the allotropic transition (from cubic to hexagonal) and melting of ZnS:Mn.

Inset: example of a linear fit performed on experimental values, i.e. ablated depth vs. number of pulses, corresponding to the laser irradiation of (d) 31 MW/cm².

V.   Discussion

A. Ablation threshold and surface morphology

Due to the low sublimation temperature of ZnS (~1300 K), the phosphor layer is subject to ablation during excimer laser processing and material losses have been observed in the past, using XeCl lasers with the specimens held under argon pressures up to 150 psi.[9,15] Recently, D. Sands et al. concluded that sublimation is the controlling factor for the onset of XeCl laser ablation in ZnS thin films deposited on Si.[16] In the present study, no surface morphology modification has been established on laser treated regions with power densities of 8 and 15 MW/cm^2. Thus, we estimate the onset for ablation to be greater than 15 MW/cm^2 which does not disagree with the simulated power density necessary for surface sublimation i.e. ~16.6 MW/cm^2 (see Section IVA).

The observed rim surrounding the measured ablation pits is essentially believed to be due to material redeposition, as previously reported for ablation processes performed in air or under controlled atmosphere.[17] In the present study, more removed material is likely to stay closer to the pressurised surface, explaining that up to 80 % of the removed material is "relocated" at the pit edge. This feature should not be disregarded for practical applications since it may be a limiting factor for the spatial dimension of the laser treated region, i.e. laser beam size. Indeed, a smooth surface morphology of the remaining phosphor layer is required for post-annealing deposition of upper insulator and electrode layers, when fabricating TFEL devices.

B. Ablation characteristics

In Ref. 6, Addiamamo and Dell were able to melt ZnS under 150 psi of Ar pressure and determined a melting point of 2100±20 K. With our experimental conditions and according to our thermal model, we anticipate the melting of ZnS:Mn to start, at the surface, under a laser irradiation of 30.5 MW/cm^2. In Fig.5, this melting threshold corresponds to the observed reduction in ablation rate.

It has been previously demonstrated that the excimer laser ablation rate of ZnS thin films deposited on Si is linearly dependent upon surface temperature and heat distribution within the thin film.[18] Thus, when significant absorption of radiation is providing the latent heat of phase transformations, the surface temperature may be lower and a reduction in the ablation rates can be expected. Hence, according to the simulated surface melting condition, the minimum region seen on the averaged ablation rate data (between ~32 MW/cm^2 and ~40 MW/cm^2, Fig. 5) may be attributed to the phase change from solid to liquid (melting) within the phosphor layer. Following the same reasoning, the quasi-constant region (from 20 MW/cm^2 to 23 MW/cm^2, Fig. 5) is assigned to the cubic to hexagonal transition of ZnS:Mn which is predicted by the model to commence at the surface with an impinging laser power density of 17 MW/cm^2.

The non-monotonic behaviour exhibited in Fig. 5 suggests that the solid-solid and solid-liquid transformations affects differently the ablation rate of ZnS:Mn. Hence, the distinctive ablation rate reduction by melting could imply that more energy is needed for melting than for allotropic transition. Interestingly, the latter

supposition agrees with the experimental values, i.e. $\Delta_{melting,ZnS} H = 59700$ J/mol and

$\Delta_{transition,ZnS} H = 12857$ J/mol.[19]

Also, the extensions of the ablation rate decrease with increasing incident laser power may be related to the optical energy necessary for complete crystallographic transformation of the irradiated phosphor layer. Thus, the shift of the minima to lower power densities using 15 to 20 irradiations (Fig. 2, curves 15x and 20x) may be attributed to reduced ZnS:Mn thickness that require less energy for complete fusion.

The accumulated depths (Fig. 3) and ablation rates (Fig. 4) increase and decrease, respectively, with increasing number of laser pulses. This suggests that the phosphor thin film is more difficult to remove with increasing pit depth and that the first laser pulse impinging on a target area is more effective at removing material than the following pulses. In Ref. 9, a similar effect was reported using the 25 ns pulse duration of a XeCl laser to ablate ZnS thin films deposited on Si. It was demonstrated that the reduction of ablation rates can be attributed to optical interference effects at small film thickness (~50 nm), and to residual ZnS thicknesses smaller than the thermal diffusion length, thus allowing more heat conduction within the Si substrate. In the present work, the ablation rate reduction with increasing pit depth is seen with residual ZnS:Mn films thicker than 200 nm (e.g. using 3 to 10 pulses, Fig. 3). Hence, the optical interference effects can be excluded. Therefore, it is suggested that the reduction in material removal is due to a decrease of the phosphor temperature owing to more thermal conduction into the underlying layers, and/or due to enhanced redeposition effects with increasing pit depths.

In Figure 3, pits deeper than 800 nm are reported, meaning that some of the insulating layer is removed as well. Since Y_2O_3 is transparent to the KrF laser wavelength (Table I), it is proposed that its removal is due to heat conduction from the heated silicon substrate. However, its exact ablation mechanism is not well understood at the present time. Note that using our experimental conditions, c-Si is expected to melt at $\sim$25 MW/cm^2,[4] which is well below the power densities impinging on Y_2O_3 (see Fig. 3, curves 15x and 20x).

VI.   Conclusions

Evolution of the laser ablation characteristics of ZnS:Mn have been examined under various pulse numbers and laser power densities. Combining the ablation study and results of the thermal model, it is inferred that allotropic transition and melting of ZnS:Mn are responsible for reductions in ablation rate due to conversion of thermal energy to initiate the phase transformations. The effects of laser ablation on the luminescent properties of these samples will be examined in the next Chapter.

Finally, the simulated spatial temperature profiles generated by single pulse laser irradiation suggests that there is a minimal heat deposition at the phosphor / insulator interface, which is the premise behind using laser processing.

References

[1] W. J. Troff and M. E. Thomas, in: *Handbook of optical constants of solids II* (Academic Press, 1991), p. 1079.

[2] T. Tomiki, J. Tamashiro, Y. Tanahara, A. Yamada, H. Fukutani, T. Miyahara, H. Kato, S. Shin, and M. Ishigame, J. Phys. Soc. Jap. **55**, 4543 (1986).

[3] Y. Nigara, Jap. J. Appl. Phys. **7**, 404 (1968).

[4] S. de Unamuno and E. Fogarassy, Appl. Surf. Sci. **36**, 1 (1989).

[5] S. Ozaki and S. Adachi, Jpn. J. Appl. Phys. **32**, 5008 (1993).

[6] A. Addamiano and P. A. Dell, J. Phys. Chem. **61**, 1020 (1957).

[7] L. M. Lopato, B. S. Nigmanov, A. V. Shevchenko, and Z. A. Zaitseva, Inorg. Mater. **22**, 678 (1986).

[8] A. Addamiano and M. Aven, J. Appl. Phys. **31**, 36 (1960).

[9] W. M. Cranton, P. H. Key, D. Sands, C. B. Thomas, and F. X. Wagner, Appl. Surf. Sci. **96-98**, 501 (1986).

[10] *Handbook of Chemistry and Physics*, 78th ed., edited by D. R. Lide (1997-1998).

[11] *Thermophysical properties of matter, Vol. 2, Thermal conductivity of nonmetallic solids*, edited by Y. S. Touloukian (IFI/Plenum, NewYork-Washington, 1970).

[12] *Thermophysical properties of matter, Vol. 5, Specific heat of nonmetallic solids*, edited by Y. S. Touloukian (IFI/Plenum, NewYork-Washington, 1970).

[13] *American Institute of Physics Handbook*, 2nd ed., edited by E. Dwight (McGraw-Hill, New York, 1972).

[14] B. J. Bailey and K. Kellner, Physica **39**, 444 (1968).

[15] H. S. Reehal, J. M. Gallego, and C. B. Edwards, Appl. Phys. Lett. **40**, 258 (1982).

[16] D. Sands, P. Key, and J. Hoyland, Appl. Surf. Sci. **138-139,** 240 (1999).

[17] *Laser Processing and Chemistry*, ed. by D. Bauerle (Springer, 1996), p 207.

[18] D. Sands, F.X. Wagner, and P.H. Key, J. Appl. Phys. **85,** 3855 (1999).

[19] R.C. Sharma and Y.A. Chang, J. Phase Equilibria **17,** 261 (1996).

CHAPTER 5: Effects of multiple laser irradiations on the luminescence of ZnS:Mn / Y$_2$O$_3$ multilayers

I.   Introduction

In the previous chapter, the effects of multiple irradiations and incident laser power densities upon the surface ablation of ZnS:Mn based electroluminescent structures were investigated. Here, to conclude this study, both photoluminescence and electroluminescence analyses are performed on the same samples.

Thus, in this Chapter, both laser annealing and laser ablation effects on the luminescent properties of ZnS:Mn based TFEL devices can be discussed. Also, the photoluminescence and electroluminescence results are compared with those obtained from thermally annealed samples in vacuum for one hour, at temperatures of 450 °C, 500 °C, and 700 °C.

II.   Experimental procedure

The laser arrangement and processed samples are the same than in Chapter 4. For comparison, two cleaved areas of the wafer coated with the ZnS:Mn / Y₂O₃ multilayer were separately thermally annealed in vacuum for 1 hour at temperatures of 500 °C and 700 °C.

Figure 1 shows a schematic cross-section of the laser and thermally annealed samples.
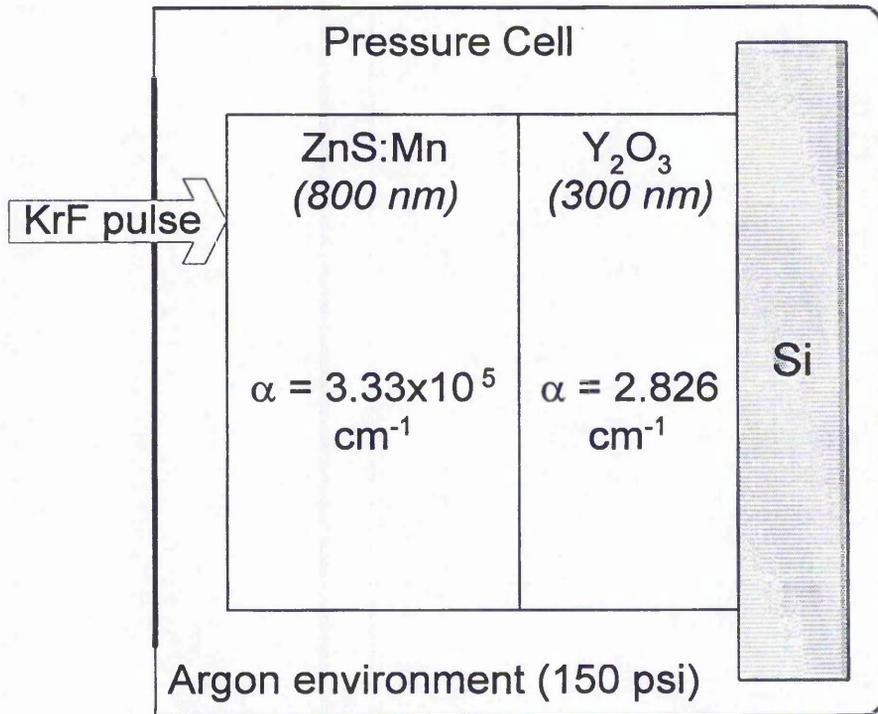
FIG. 1. Schematic cross-section of the pressure cell used for KrF laser processing and of the ZnS:Mn / Y_2O_3 multilayer deposited on a Si (100) substrate. α is the optical absorption coefficient determined for the KrF laser wavelength (see Chapter 4).

To fabricate TFEL devices, an upper insulator layer (300 nm of Y_2O_3) and an indium tin oxide (ITO) electrode were deposited after the thermal and laser treatments. The ITO electrode was grown by radio-frequency sputtering through a shadow mask which was designed to allow electrical probing of the individually laser and thermal processed regions (see Appendix B). For reference, this TFEL device wafer is called NTU323.

During thin film deposition, the substrate temperature was maintained at 200 °C for the insulator and phosphor thin films growth, and at 450 °C during the one hour deposition of the ITO electrode. In the following, we therefore consider the non-treated regions for the photoluminescence and electroluminescence analyses as being annealed respectively at 200 °C and 450 °C for one hour.

The photoluminescence spectra were recorded via a N_2-cooled CCD spectrometer and were obtained by directly exciting the as-grown and annealed ZnS:Mn thin films, prior to upper insulator deposition, using the 496.5 nm ($E_{excitation}$ ~2.5 eV, P ~1.25 mW) emission wavelength of a CW Argon ion laser. (The choice of sub-bandgap ($E_{g,ZnS}$ ~3.66 eV) photoluminescence analysis will be discussed in Section IV).

The fully fabricated TFEL devices were driven with a 5 kHz sinusoidal alternating current voltage and their electroluminescence brightness-voltage characteristics were measured with a Minolta LS-110 luminance-meter, using surface emission through the ITO upper electrode.

III.   Results

A.   Laser ablation of ZnS:Mn

Figure 2 shows the depth of material removed after 3 to 20 pulses of various laser power densities. Most of the data are reported from the ablation study of Chapter 4.
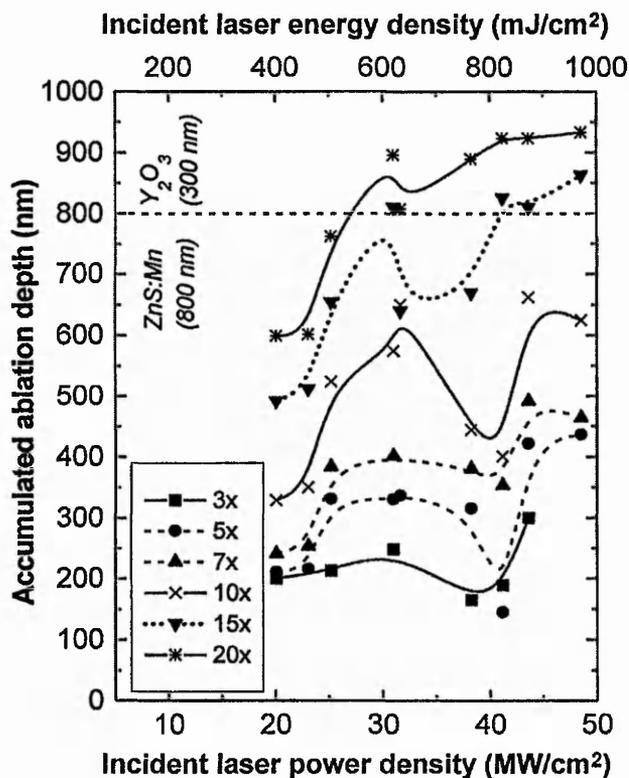
FIG. 2. Cumulative ablated depth plotted against the incident laser power density at a range of pulse numbers for a stack of 800 nm of ZnS:Mn and 300 nm of Y_2O_3 deposited on Si. Curves for each specific number of pulses (3x, 5x, 7x, 10x, 15x, 20x) are fitted by B-splines and drawn for clarity.

B. Photoluminescence analysis

Figures 3 and 4 show the maximal sub-bandgap photoluminescence signals, i.e. the peaks of the ZnS:Mn emission spectra (@ ~585 nm), emitted from the laser annealed samples as a function of irradiation pulse number and power density. (For comparison, the peak photoluminescence values obtained with the thermally annealed samples are shown as horizontal dashed lines).

All curves corresponding to specific pulse numbers (1x, 2x, 3x, 5x, in Fig. 3 and 7x, 10x, 15x, 20x, in Fig. 4) exhibit a sharp increase before reaching maximum photoluminescence values between 20 MW/cm^2 and 30 MW/cm^2. Above these maxima, the photoluminescence decreases drastically for all multiple pulse configurations whereas for single pulse irradiation (Fig. 3), it saturates at its maximum value, which also corresponds to that obtained by the sample thermally annealed at 500 °C during one hour.

Using pulsed laser processing, a major increase in photoluminescence is obtained with two pulses at 30 MW/cm^2 and the resultant photoluminescence signal is improved by 360 %, 67 %, and 19 % with respect to samples thermally annealed at 200 °C (as-grown), 500 °C, and 700 °C. From 3 to 5 irradiations, the maximum photoluminescence improvement is similar to that obtained with two pulses (Fig. 3) but above 7 pulses, it reduces with increasing pulse number (Fig.4).
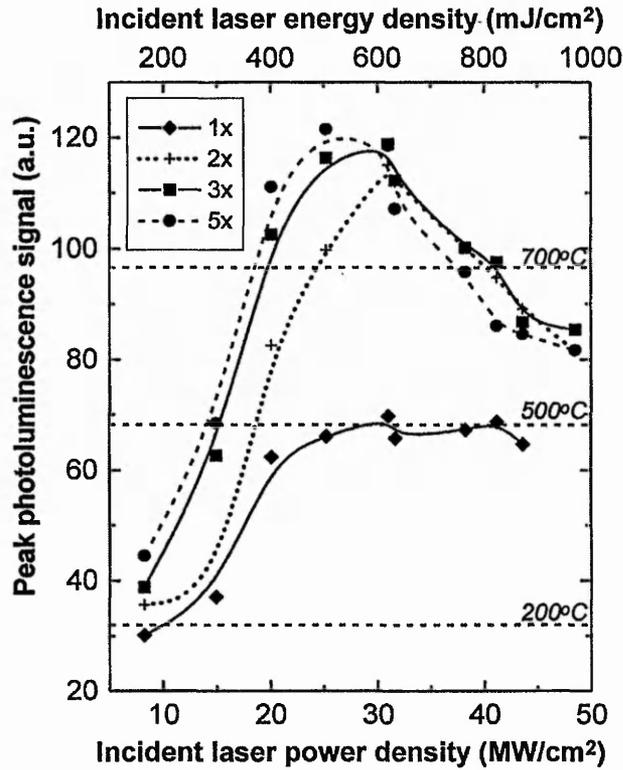
FIG. 3. Maximal photoluminescence signals measured from the ZnS:Mn emission spectra vs. incident laser power density for various pulse numbers. The photoluminescence was excited by an argon ion laser emitting at a wavelength of 496.5 nm. Curves for each specific number of pulses (1x, 2x, 3x, 5x) are fitted by B-splines and drawn for clarity. Horizontal dashed lines correspond to the peak photoluminescence values obtained form samples thermally annealed at 200 °C (as-grown), 500 °C, and 700 °C for 1 hour.
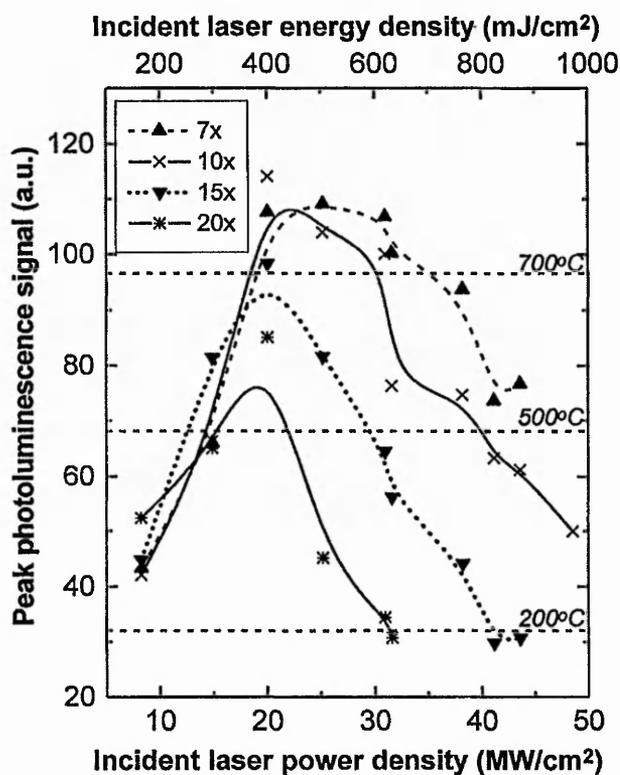
FIG. 4. Maximal photoluminescence signals measured from the ZnS:Mn emission spectra vs. incident laser power density for various pulse numbers. The photoluminescence was excited by an argon ion laser emitting at a wavelength of 496.5 nm. Curves for each specific number of pulses (7x, 10x, 15x, 20x) are fitted by B-splines and drawn for clarity. Horizontal dashed lines correspond to the peak photoluminescence values obtained form samples thermally annealed at 200 °C (as-grown), 500 °C, and 700 °C for 1 hour.

C. Electroluminescence analysis

The brightness-voltage (B-V) characteristics of thermally and laser annealed samples with 8 MW/cm^2 are plotted in Figure 5. The thermally annealed samples at 450 °C, i.e. the ITO deposition temperature, and at 500 °C exhibit equal maximum brightness. However, the B-V characteristic of the sample annealed at 500 °C (before top dielectric and ITO deposition) is softer and its threshold voltage (V$_{th}$) is lower. In comparison, the laser annealed sample with 7 irradiations at 8 MW/cm^2 shows better device performance characteristics, i.e. a steeper B-V response and a higher maximum brightness. At this laser power density, the device performances are improved when irradiating from 3 to 7 pulses and degrade with higher number of impinging pulses.

In figure 6, the investigated laser power density is 15 MW/cm^2. As shown, single or double pulses do not have significant effects on the B-V response as compared to the thermally annealed sample at 450 °C. However, when using 7 pulses or more, the device performances are degraded as opposed to the results of Figure 5, which showed maximum brightness with 7 pulses of 8 MW/cm^2.

To examine the latter degradation effect, Figure 7 shows the B-V characteristic of laser annealed samples that were irradiated 7 times with varying incident laser power densities. Above 8 MW/cm^2, the B-V response and V$_{th}$ are respectively softened and reduced with increasing power density, and as excepted from Figures 5 and 6, the maximum brightness is concomitantly decreased. However, for samples that were expected to melt according to the thermal model, i.e. those irradiated with 31

MW/cm^2, this behaviour is not exhibited. Indeed, although their threshold voltage is drastically reduced and the B-V response softened, these samples are brighter than those annealed at 15 MW/cm^2 and 23 MW/cm^2.
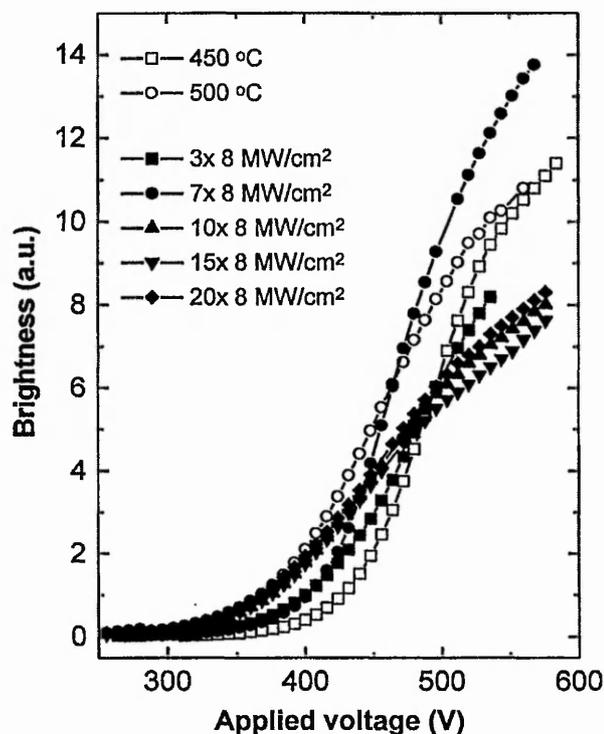
FIG. 5. Brightness-Voltage characteristics of samples thermally annealed at 450 °C and 500 °C (prior to top dielectric and ITO depositions), and samples laser annealed with 3, 7, 10, 15, and 20 irradiations of 8 MW/cm^2.
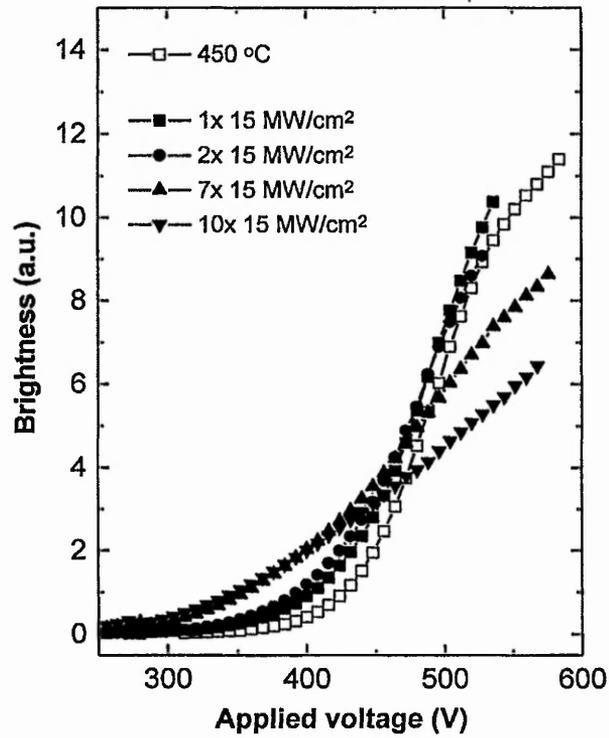
FIG. 6. Brightness-Voltage characteristics of samples thermally annealed at 450 °C, and samples laser annealed with 1, 2, 7, and 10 irradiations of 15 MW/cm^2.
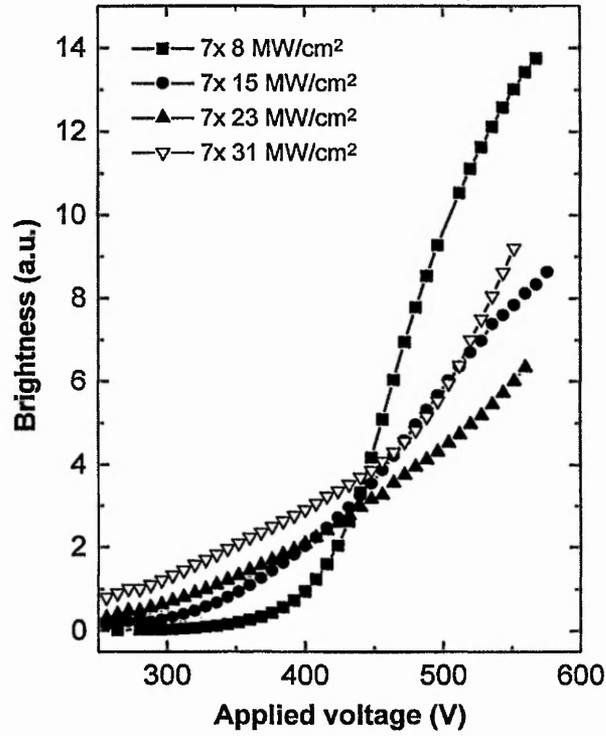
FIG. 7. Brightness-Voltage characteristics of samples laser annealed with 7 irradiations of 8 MW/cm^2, 15 MW/cm^2, 23 MW/cm^2, and 31 MW/cm^2.

IV.   Discussion

In the following, the results of the ablation study and of the thermal model presented in Chapter 4 are used to discuss the photoluminescence and electroluminescence analyses. Also, there is particular emphasis on the samples that are expected to melt according to the thermal model, i.e. when irradiated with a laser power density $>=30.5$ MW/cm^2.

A.   Sub-bandgap photoluminescence of ZnS:Mn

Zinc sulphide is transparent to visible light due to its large bandgap ($E_{g,ZnS}$ ~3.6 eV), and consequently to the 496.5 nm ($E_{exitation}$ ~2.5 eV) emission wavelength of a CW Ar$^+$ laser. Since the aim of this work is to compare the luminescent characteristics of samples with varying ZnS:Mn thickness, sub-bandgap photoluminescence ($E_{excitation}$ < $E_{g,ZnS}$) was preferred to upper-bandgap photoluminescence ($E_{excitation}$ > $E_{g,ZnS}$) since the former does not depend on the optical absorption length of the excitation light.

Below 3.5 eV, the absorption spectrum of ZnS:Mn exhibits five peaks that correspond to the five lowest excited states of Mn^{2+} in ZnS.[1,2] In fact, Ohba, et. al.,[1] determined the luminescence quantum efficiencies for these five excited states (2.32 eV, 2.49 eV, 2.66 eV, 2.90 eV, 3.16 eV) and concluded that the lowest three have the highest efficiencies since the radiative decay from these excited states is loss free. Hence, when using photon energies of ~2.5 eV (Ar$^+$ laser) we can assume that the

photoluminescence signals result from direct excitation of Mn centres which should be only proportional to the number of active Mn centres and not a function of non-radiative recombination paths, e.g. due to a modification in the point defects concentration.[3]

The sub-bandgap photoluminescence and ablation analyses performed on the laser processed samples highlight that there is an optimum laser power density per pulse configuration (Figs. 3 and 4) and that maximum photoluminescence signals were measured from ablated samples (Figs. 2). Hence, the optimum condition is a competition between activating as much Mn^{2+} as possible and losing the minimum of phosphor material via sublimation (Chapter 4). The nature of this competitive process is more precisely due to the fact that the thermal ablation mechanism is related to the maximum surface temperature attained during the 20 ns pulse irradiation (Chapter 4), whereas the photoluminescence signal depends more on the heat deposited within the whole ZnS:Mn layer. Consequently, although more material may be removed under higher irradiation number and/or power densities, more Mn^{2+} may also be activated owing to higher in-depth temperature profiles.

Finally, multiple irradiation shows photoluminescence improvement as compared to single irradiation implying that more Mn^{2+} are actively incorporated within the ZnS host lattice when irradiating a pre-laser treated area. A similar behaviour was exhibited with the ZnS:Mn layer directly deposited on Si (Chapter 2).

B. Electroluminescence characteristics

Electroluminescence in TFEL devices arises from four successive mechanisms which are reported as (i) tunnel emission of electrons from the phosphor / insulator interfaces, (ii) ballistic acceleration followed by impact excitation of the Mn^{2+} ions, (iii) luminescence decay of the Mn^{2+} centres, and (iv) re-trapping of the electrons at the anodic interface (Chapter 1). The device performances are therefore strongly related to: (a) the nature of the interfaces, i.e. the source of electrons, (b) the crystalline quality of the active layer which determines the carrier transport, and (c) the efficiency of the luminescent centres.

For the present study, another important parameter to consider is the remaining phosphor thickness after each laser pulse since it is directly related to: (i) the electric field redistribution and hence, V_{th}, (ii) the total number of active Mn ions, i.e. maximum brightness, and (iii) the B-V slope i.e. interface states modification due to enhanced interfacial temperatures for multiple irradiations when previous pulses have reduced the phosphor layer thickness.

However, the electroluminescence characteristics of the laser annealed samples with 8 and 15 MW/cm^2 (Figs. 5 and 6) should not be thickness dependent since the onset for ablation was estimated to be >15 MW/cm^2 (Chapter 4). At these lower power densities, the photoluminescence signal increases monotonically with increasing number of pulses (Figs. 3 and 4). Hence, the increase in number of active Mn^{2+} within ZnS implied by the photoluminescence results would be consistent with improved maximum electroluminescence brightness when irradiating the sample

from 3 to 7 times with 8 MW/cm^2 (Fig. 5). Nevertheless, although the photoluminescence still improves with higher power density and number of pulses, the electroluminescence signals decrease and the B-V curves are softened accordingly.

From the sub-bandgap photoluminescence discussion, it is believed that multiple irradiation at constant power density generates more in-depth structural modification due to enhanced heating within the phosphor thin film. Consequently, an improved structural quality of the phosphor material is also expected which should enhance the transfer probability of the electron energy to the luminescent centres.[4,5]

However, the temperature will also rise at the phosphor / insulator boundary, which has been discussed to be responsible for the TFEL performance limitation at high annealing temperatures (Chapter 1). More precisely, this temperature dependent modification of the interface has been shown to affect the interface state density profile and un-pin the Fermi level,[6] which may be responsible for the reduction in V_{th} leading to softer B-V characteristics.[7]

The brightness and V_{th} reductions are even more pronounced for thinned samples (ablation) as seen in Fig. 7 where higher temperatures are produced at the interface and where the electric field is redistributed through a thinner phosphor layer (see Fig. 2).

According to the knowledge gathered so far, when irradiating 7 times a sample with increasing laser power density, the maximum brightness is not expected to increase. However, this is not the case when using a laser power density of 31 MW/cm^2 (Fig. 7) that correspond to the simulated surface melting threshold, i.e. 30.5

MW/cm^2 (Chapter 4).

In the past, laser melting of ZnS:Mn deposited on Si was shown to increase the grain size and to remove defects within the phosphor layer.[8] This may further improve the excitation and radiative efficiencies of Mn ions within the ZnS host lattice,[4] which may explain the increase of electroluminescence brightness despite the discussed detrimental heating effects at the electronic interface.

V. Conclusions

The effects of multiple pulse KrF irradiations on a ZnS:Mn based structure have been probed by sub-bandgap photoluminescence and electroluminescence analyses. First, it was demonstrated that the optimum laser processing parameters for maximum photoluminescence signal reside in the competition between annealing and ablation, i.e. between increasing the number of active luminescent centres and removing phosphor material.

Unfortunately, the performances of the fully fabricated TFEL devices did not exhibit the improvements predicted from the photoluminescence study. It is inferred that for electroluminescent applications, a concomitant modification of the electronic interface and ablation effects are the major limitations of the investigated multiple pulse irradiation technique. The B-V characteristics of TFEL devices irradiated with single pulses will be presented in Chapter 7.

Finally, electroluminescence characteristics of laser annealed samples with laser power densities of 31 MW/cm^2 may provide further evidence towards the simulated surface melting threshold of ZnS:Mn, i.e. 30.5 MW/cm^2.

References

[1] Y. Ohba, M. Mizuta, and H. Kukimoto, J. Lumin. **28**, 111 (1983).

[2] P. Jaszcyn-Kopec, J. P. Pinceaux, M. Zigone, J. M. Kennedy, and A. Stadtmuller, Solid State Commun. **32**, 473 (1979).

[3] A. F. Cattel and A. G. Cullis, Thin Solid Films **92**, 211 (1982).

[4] H. Xian, P. Benalloul, C. Barthou, and J. Benoit, Jpn. J. Appl. Phys. **33**, 5801 (1994).

[5] R. H. Horng, D. S. Wuu, and J. W. Yu, Mater. Chem. and Phys. **51**, 11 (1997).

[6] W. M. Cranton, PhD. thesis, University of Bradford (1995).

[7] W.M. Cranton, R. Stevens, C.B. Thomas, A.H. Abdullah and M.R. Craven, Poc. IEE Colloquium on Materials for Displays (1995).

[8] H. S. Reehal, J. M. Gallego, and C. B. Edwards, Appl. Phys. Lett. **40**, 258 (1982).

CHAPTER 6: Thermal annealing effects upon the interface structure of ZnS:Mn / Y_2O_3 multilayers

I.   INTRODUCTION

As suggested in Chapter 1, the electronic nature of the phosphor / insulator interface plays an important role in TFEL device performance, and in the last Chapter, this issue has been raised again when using multiple pulse laser processing of ZnS:Mn based TFEL structures. Consequently, it further highlights the importance of knowing and controlling the annealing effects upon TFEL interfaces.

However, while much material science studies have been reported on the effect of deposition temperature[1,2,3,4] and thermal annealing[5,6,7] upon the phosphor thin film, there has been little emphasis upon the phosphor / insulator electronic interface, and in particular on the structural modifications of the insulating layer due to annealing. The few research groups who investigated the heating effects upon the electronic interfaces suggested that a density modification of interfacial energy states is responsible for device performance saturation at annealing temperatures >=500 °C.[8,9,10] This scarcity of electroluminescence studies performed at temperatures >=500 °C may reflect the fact that much TFEL research is concerned with displays fabricated on glass substrates, which limits the maximum thermal annealing temperatures to ~500 °C. Here, however, the studied devices are fabricated on silicon substrates that melt at ~1410 °C,[11] which permits higher treatment temperatures. Hence, in order to study the effects of annealing in greater detail, the crystalline modifications of the phosphor / insulator multilayers are examined in an attempt to explain the modifications in electro-optical performance that result at temperatures >=500 °C.

Presented in this Chapter are the results of x-ray diffraction, photoluminescence, and electroluminescence analyses of thermally annealed TFEL structures. The annealing effects on crystallinity and lattice misfit between the insulator and phosphor layers are correlated to luminescent performance and modifications of the interface. Additionally, the crystalline structure of the phosphor layer is quantitatively examined when it is directly deposited on Si or on Si coated with Y_2O_3.

II. EXPERIMENTAL

A. Thin film deposition and thermal annealing

The $ZnS:Mn$ / Y_2O_3 multilayer deposition and the thermal annealing procedure has been described in Chapter 5.

The various depositions and annealing characteristics of the samples used in this Chapter are listed in Table I.

TABLE I. Deposition and thermal annealing conditions used for the present study. All structures deposited by radio-frequency sputtering onto Si (100) substrates.

Ref.	Structure	Annealing temp.(°C)
NTU228	800 nm ZnS:Mn	200,400,500,600,700
NTU398	100 nm Y_2O_3	500
NTU259	300 nm Y_2O_3 / 800 nm ZnS:Mn	200,300,400,500,600
NTU161	300 nm Y_2O_3 / 800 nm ZnS:Mn / 300 nm Y_2O_3	400,500,600,700

Samples NTU228 and NTU398 are respectively, 800 nm of ZnS:Mn and 100 nm of Y_2O_3 single layers deposited on Si. These samples enabled the separate structural analysis of the two materials composing the TFEL devices grown in our laboratory. Samples NTU259 are composed of the two first layers of the basic TFEL devices developed at TNTU, i.e., multilayers of ZnS:Mn (800 nm) and Y_2O_3 (300 nm) deposited on Si, allowing a simultaneous study of their crystallinity and lattice dependence on thermal annealing temperature. Samples NTU161 are fully fabricated TFEL devices used for photoluminescence and electroluminescence analyses at varying thermal annealing temperatures.

B. X-ray diffraction, electroluminescence, and photoluminescence

X-ray diffraction (XRD) analyses were performed to investigate the crystallinity of the samples NTU228, NTU398, and NTU259, using reflections from the CuKα₁ emission line (wavelength = 0.15405981 nm) into a Siemens D5000 diffractometer with front monochromator. The applied power of the x-ray tube was 35 KV x 25 mA and the angular step was 0.005° within the studied 25° to 62° range. The quanta acquisition time was 5 seconds for NTU228 (see Chapter 3), and 20 seconds for NTU398 and NTU259.

Electroluminescence and photoluminescence emission of thermally annealed samples were studied on the NTU161 structure. The TFEL device was driven with a constant sine wave frequency of 5 kHz and brightness was measured via a Minolta LS110 luminance meter, using the light emitted from an exposed edge on the devices.[10]

Photoluminescence measurements were performed using a 20 Hz pulsed N$_2$ laser emitting at 337 nm ($E_{excitation}$ ~3.68 eV). The peak photoluminescence intensities were recorded via an EG&G PARK OMA spectrometer.

III.   RESULTS

A. X-ray diffraction analysis

Figure 1 shows selected diffraction angles (27-32° and 55-57°) within the XRD patterns of the samples NTU228, NTU398, and NTU259. Here, it is to be borne in mind that NTU228 [Fig. 1(a)] and NTU398 [Fig. 1(b)] represent the diffraction patterns of the phosphor and insulating layers individually deposited on Si, and NTU259 represent the diffraction patterns obtained from the ZnS:Mn /Y$_2$O$_3$ multilayers deposited on Si as a function of annealing temperature [see Figs. 1(c)-1(g)].
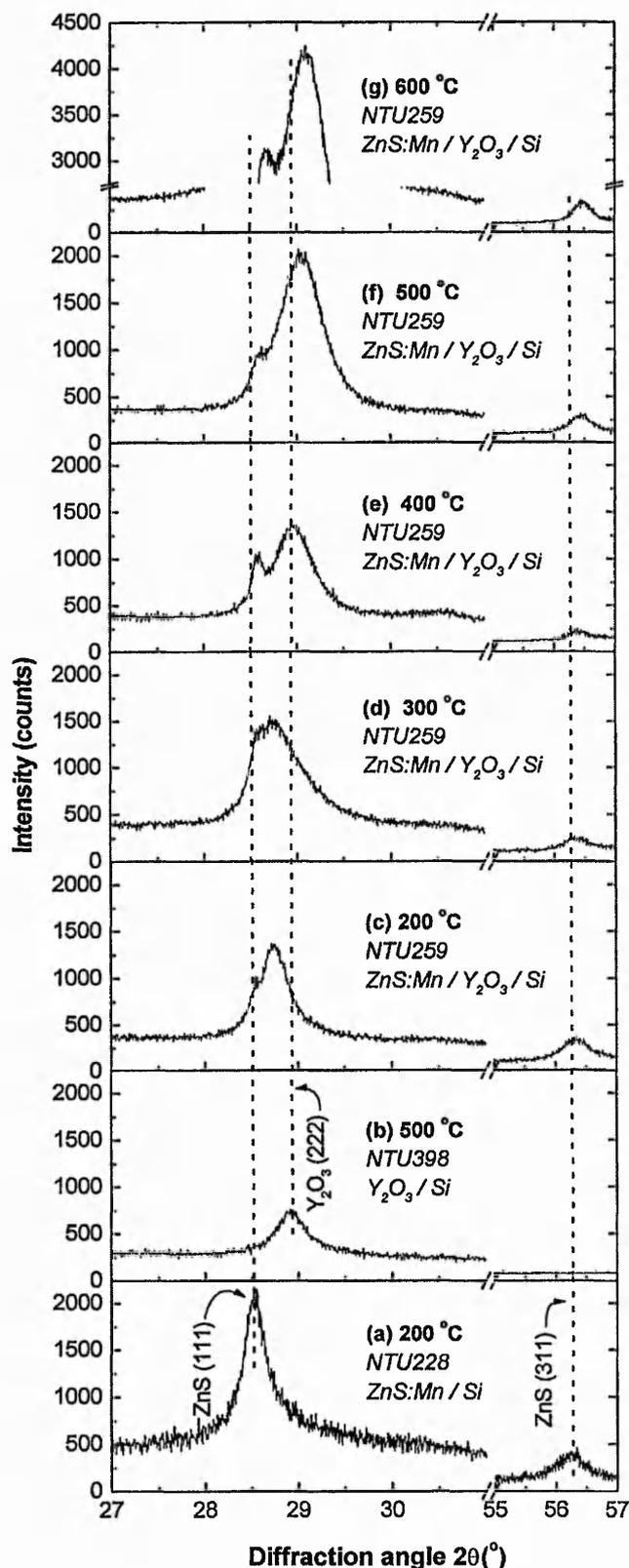
FIG. 1. Partial XRD patterns of thermally annealed thin films as: 800 nm of ZnS:Mn annealed at 200 °C (deposition temperature) (a), 100 nm of Y_2O_3 annealed at 500 °C (b), multilayers of ZnS:Mn (800 nm) / Y_2O_3 (300 nm) annealed at 200 °C (deposition temperature) (c), 300 °C (d), 400 °C (e), 500 °C (f), 600 °C (g). The horizontal dashed lines correspond to the approximate positions of the diffraction lines ZnS (111), Y_2O_3 (222), and ZnS (311) observed in Figs. 1(a) and 1(b).

The data in Fig. 1(a) are reported from Chapter 3, and have been corrected for a quanta acquisition time of 20 seconds.

In Chapter 3, it was observed that the ZnS:Mn films directly grown on Si exhibit predominantly the zinc-blende structure with a preferred <111> orientation. Accordingly, the observed diffraction peaks in Fig. 1(a) are attributed to the cubic (111) and (311) reflection planes. The thermal annealing effects on the crystallinity of ZnS:Mn were also investigated and it was concluded that thermal treatments up to 700 °C for 1 hour do not induce grain growth or recrystallisation of ZnS:Mn when grown onto Si (100) substrates. This conclusion was found to be in agreement with the work from Cattel and Cullis[12] who investigated similar films and substrates.

A further analysis of these diffraction lines showed that the d-spacings of the phosphor lattice, directly deposited on Si, monotonically decreases with annealing temperatures from 200 °C to 700 °C.

The diffraction pattern of the Y_2O_3 thin film deposited on Si (100) is partially shown in Fig. 1(b). The diffraction plane (222) is the only one responsible for significant constructive interference observed within the investigated diffraction angle range, i.e, 25°-62°. The calculated diffraction line positions and intensities of Y_2O_3 from the Joint Committee on Powder Diffraction Standards (JCPDS) have been presented elsewhere.[13] Briefly, in its powder form, the normalised theoretical intensities of the three main diffraction planes (222), (400), and (440) are 1, 0.4, and 0.44, respectively, and their positions are at 29.52°, 33.78°, and 48.53°, respectively. In the present study, the (400) and (440) lines do not appear in the diffraction pattern, which implies a radical difference between theoretical and experimental relative intensities. Hence, it is evidenced that the sputtered cubic bixbyite Y_2O_3 structure is

preferably oriented in the <222> direction.

The approximate position of the diffraction lines observed in Fig. 1(a) and Fig. 1(b) are plotted as vertical dashed lines for reference to the following examination.

Figures 1(c) to 1(g) represent the XRD patterns of the ZnS:Mn / Y₂O₃ multilayers thermally annealed from 200 °C to 600 °C for 1 hour.

A first qualitative examination of the XRD patterns suggests that the absolute intensity of the ZnS (111) diffraction peak does not change from 200 °C to 500 °C (~1000 counts), and is increased at 600 °C (~3000 counts). Similarly, the absolute intensity of the Y₂O₃ (222) diffraction peak stays constant from 200 °C to 400 °C (~1500 counts), and increases from 500 °C (~2000 counts) to 600 °C (>4000 counts).

Secondly, it is observed that the diffraction angles $2\theta_{111,ZnS}$, $2\theta_{222,Y2O3}$, and $2\theta_{311,ZnS}$ shift to higher scattering angles with increasing annealing temperature. In addition, the overall shape modifications of the superposed ZnS (111) and Y₂O₃ (222) diffraction lines suggest that $2\theta_{222,Y2O3}$ increases more rapidly than $2\theta_{111,ZnS}$ [see Figs. 1(e)-1(g)].

In order to study these effects further, the diffraction curves involving both the ZnS (111) and Y₂O₃ (222) lines were deconvoluted using the Laurenzian approximation.

Figures 2 and 3 show the quantitative annealing temperature effect on the integrated intensities and diffraction angles of respectively the ZnS (111) and Y₂O₃ (222) lines. The integrated intensity analysis was preferred to maximum intensity since the former is more characteristic of the individual specimens.[14] Here, it is

confirmed that the integrated intensity increase occurs above 400 °C and above 500 °C for respectively the ZnS (111) and Y$_2$O$_3$ (222) diffraction lines, and that their diffraction angles increase with annealing temperature.

The larger tick marks on the diffraction angle ordinates in Figs. 2 and 3 correspond to the calculated values of respectively $2\theta_{111,ZnS}$ and $2\theta_{222,Y2O3}$, which were determined using the single crystal lattice constants $a_{ZnS} = 0.54102$ nm[15] and $a_{Y2O3} = 1.0604$ nm[16] (see Equations 1 and 2 in section IIIB). It is thereby suggested that with increasing annealing temperature, the atomic positions within the sputtered Y$_2$O$_3$ crystallites tend to match the perfect crystalline arrangement (Fig. 3) whereas the ZnS:Mn lattice tends to deviate from its undoped single crystal lattice structure (Fig. 2).

Note that the summation of the two computed Lorenzian approximations fit very well with the experimental diffraction curves from Figure 1 as displayed by the magnitude of the error bars.

Additionally, the horizontal dots in Figure 2 represent the integrated intensity value of the ZnS (111) diffraction line corresponding to the structure NTU228 [Fig. 1(a)]. This value was reported to be independent on the thermal annealing conditions investigated here (Chapter 3). From this direct comparison between NTU228 and NTU259 (Fig. 2), it is obvious that there is a drastic difference in the degree of <111> orientation and annealing effects when 800 nm of ZnS:Mn are directly deposited on Si or on Si coated with 300nm of Y$_2$O$_3$.
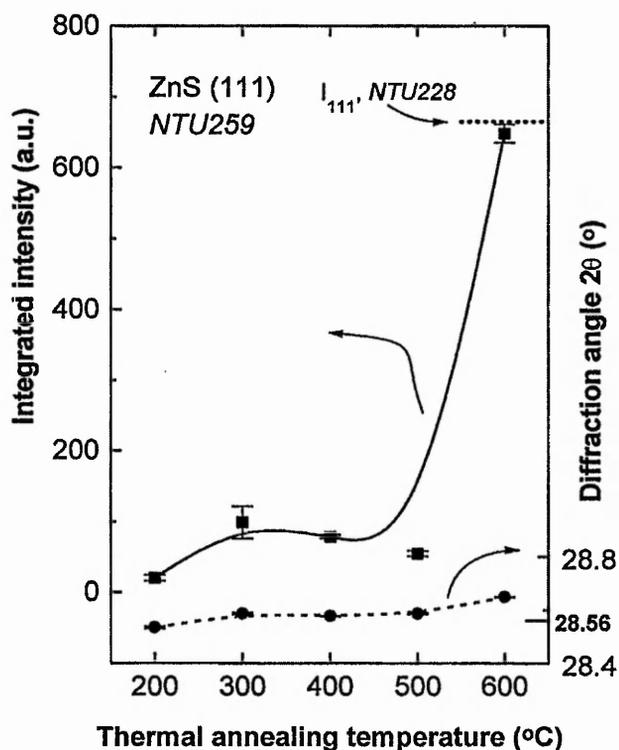
FIG. 2. ZnS (111) diffraction line characteristics as a function of thermal annealing temperature. Data obtained from XRD peak deconvolutions of ZnS:Mn (800 nm) / Y_2O_3 (300 nm) multilayers deposited on Si (100). Curves are generated by computer algorithm and are included for clarity. The diffraction angle value of 28.56° corresponds to the calculated (111) diffraction angle of single crystal ZnS. Horizontal dots represent the constant integrated intensity of a 800 nm thick ZnS:Mn thin film deposited on Si (100) and annealed at temperatures from 200 °C to 700 °C.
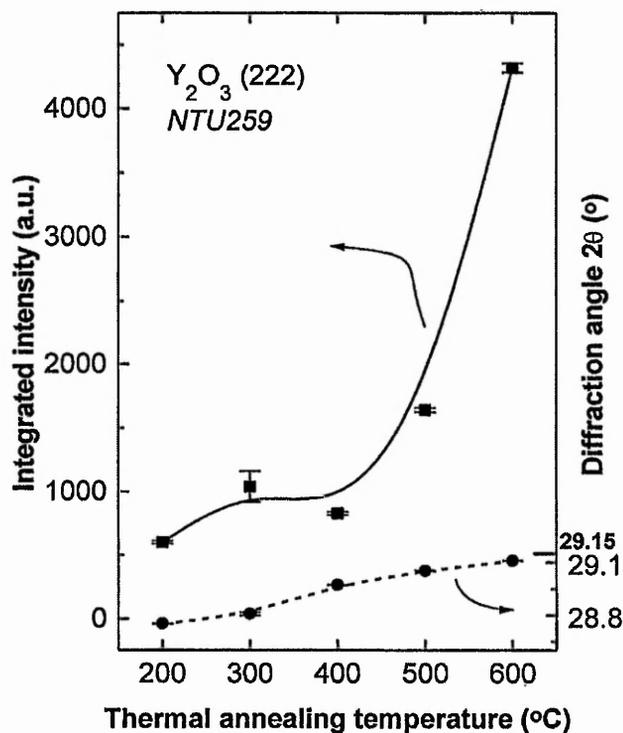
FIG. 3. Y_2O_3 (222) diffraction line characteristics as a function of thermal annealing temperature. Data obtained from XRD peak deconvolutions of ZnS:Mn (800 nm) / Y_2O_3 (300 nm) multilayers deposited on Si (100). Curves are generated by computer algorithm and are included for clarity. The diffraction angle value of 29.15° corresponds to the calculated (222) diffraction angle of single crystal Y_2O_3.

B. Lattice constant calculations

The investigated ZnS:Mn and Y_2O_3 lattices both have cubic structures. Hence, the lattice constants are calculated from the measured diffraction angles using the Bragg law

$$n\lambda = 2d_{hkl}\sin\theta_{hkl}, \tag{1}$$

and the plane spacing equation for cubic structures

$$(1/d_{hkl})^2 = (h^2+k^2+l^2)/a^2, \tag{2}$$

where n is the order of reflection, λ is the x-ray emission wavelength, d_{hkl} is the distance between adjacent planes of Miller indices hkl, θ_{hkl} is half of the diffraction angle, and a is the lattice constant of the cubic structure.[14]

Since there exist a lattice site at the centre of the cubic bixbyite Y_2O_3 cell,[17,18] the lattice misfits between the insulating and phosphor layers are determined as

$$1 - (a_{Y2O3}/2a_{ZnS}). \tag{3}$$

Table II shows the results of the calculated lattice constants and lattice misfits using the diffraction angles of the ZnS:Mn (111) and Y_2O_3 (222) lines measured from the thermally annealed NTU259 samples (see Figs. 2 and 3).

TABLE II. Results of the phosphor / insulator lattice misfit $1 - (a_{Y2O3}/2a_{ZnS})$ calculated for the thermally annealed NTU259 samples. $2\theta_{111,ZnS}$ and $2\theta_{222,Y2O3}$ are the measured diffraction angles of the ZnS:Mn (111) and Y₂O₃ (222) lines. $d_{111,ZnS}$ and $d_{222,Y2O3}$ are their interplanar spacings. a_{Y2O3} and a_{ZnS} are the determined lattice constants of the insulator and phosphor layer respectively.

NTU259		Thermal annealing temperature (°C)				
		200	300	400	500	600
$2\theta_{222,Y2O3}$	(°)	28.75	28.80	28.97	29.05	29.10
$2\theta_{111,ZnS}$	(°)	28.53	28.58	28.57	28.58	28.64
$d_{222,Y2O3}$	(nm)	0.31026	0.30967	0.30795	0.30712	0.30652
$d_{111,ZnS}$	(nm)	0.31256	0.31200	0.31210	0.31200	0.31134
a_{Y2O3}	(nm)	1.0747	1.07272	1.06677	1.06389	1.06181
a_{ZnS}	(nm)	0.54136	0.54039	0.54057	0.54039	0.53925
$1 - (a_{Y2O3}/2a_{ZnS})$	(%)	0.73	0.74	1.32	1.56	1.54

Clearly, the lattice misfit between the ZnS:Mn / Y₂O₃ multilayers is affected by the thermal treatment. Indeed, it is shown to stay constant from 200 °C to 300 °C before increasing sharply from 300 °C to 500 °C until doubling its initial value.

C. Photoluminescence and electroluminescence analysis

Figure 4 illustrates the photoluminescence (PL) and electroluminescence (EL) characteristics of the NTU161 samples thermally annealed from 200 °C to 700 °C. The plotted PL signals are measured at the maximum of the Mn^{2+} emission spectra and the electroluminescence intensities are conventionally measured at an operating potential that is 40 Volts above threshold voltage.

Both PL and EL intensities are shown to improve with annealing temperatures up to 500 °C. Above 500 °C, the maximum photoluminescence intensity increases sharply whereas the electroluminescent brightness saturates. A supplementary PL study of the NTU259 samples exhibits the same PL behaviour.
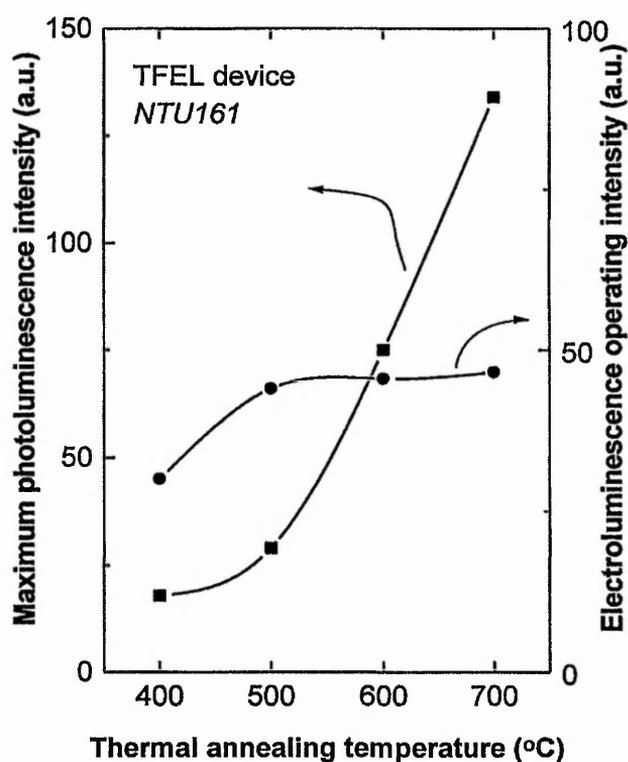
FIG. 4. Maximum photoluminescence intensity and electroluminescence operating intensity as a function of thermal annealing temperature. The photoluminescence was excited by a pulsed N_2 laser emitting at a wavelength of 337 nm. The TFEL device was driven at a constant sine wave frequency of 5 kHz and the operating intensity was measured at 40 Volts above threshold voltage.

IV. DISCUSSION

A. Crystallinity dependence on substrate and annealing

Thermally annealed ZnS:Mn thin films directly deposited on Si did not recrystallise at temperatures up to 700 °C, whereas those grown onto Y_2O_3 recrystallise at 600 °C (Fig. 2). Hence, this is direct evidence that the effects of thermal annealing on the crystallinity of sputtered phosphor layers depend on the substrate used during growth.

The integrated intensity of a diffraction line is function of the amount of lattice planes that fulfil the Bragg law. Hence, the direct comparison of the integrated intensities of the ZnS (111) lines (Figure 2) suggest that the as-grown phosphor layer is less well oriented and of worse crystalline quality when it is deposited on Y_2O_3 (NTU259) and not directly on Si (NTU228).

This is not surprising considering the differences between the theoretical lattice misfits of ZnS on Si, and ZnS on Y_2O_3, which are respectively, ~0.4% and ~2%.[17,19] Moreover, the Si substrate used is monocrystalline whereas the radio-frequency sputtered Y_2O_3 thin film is highly polycrystalline. It is also sensible to assume that the effectiveness of the thermal annealing process increases with the degree of imperfection of the treated structure. Thus, the observed recrystallisation mentioned above might be related to the crystalline quality of the as-grown phosphors, which has been discussed to be highly substrate dependent.

A second factor that may contribute to the recrystallisation of the phosphor

layer at 600 °C is the recrystallisation of the underlying insulator thin film itself. In fact, Y_2O_3 recrystallises at 500 °C and more significantly at 600 °C (Fig.3). In Ref. 17, Y. Nakanishi et al., reported that the orientation of Y_2O_3 influences that of ZnS. Hence, one could suppose that a reorientation of the Y_2O_3 lattice might favour that of the phosphor layer as well.

A further annealing effect on the ZnS:Mn / Y_2O_3 multilayers (NTU259) is the decrease of their lattice constants (Table III). A possible explanation for this is that thermal annealing causes an increase in density. From Equations 1 and 2, θ_{hkl} is proportional to $1/a$ for cubic systems, and since the volume of a cubic cell is a^3, the density ρ is also proportional to $1/a$. Thus, Fig. 3 shows that the sputtered Y_2O_3 structure tends to match the lattice constant and density of its single crystal form. Therefore, the density increase with increasing treatment temperature may be related to defects and stress removal within the sputtered crystallites.

B. Photoluminescence intensity dependence on annealing

From the PL results presented in Fig. 4, it is clear that the luminescent quality of the ZnS:Mn thin films is improving with increased thermal annealing temperature. This is indicative of improved luminescence efficiency of the phosphor material, which is the premise behind the standard TFEL annealing process. In Chapter 5, a sub-bandgap PL analysis ($E_{excitation} < E_{g,ZnS}$) performed on similar structures did not show a sharp luminescent efficiency increase at annealing temperatures above 500 °C as seen on Fig. 4. In Chapter 5, it was discussed that since the second lowest excited state of Mn^{2+} in ZnS was excited, the PL signals resulting from direct excitation of Mn^{2+} centres should only be proportional to the number of active Mn centres and not a function of non-radiative recombination paths, e.g., due to a modification in the point defects concentration. Hence the sharp increase in PL seen on Fig.4 is not attributed to a sharp increase in the number of luminescent centres.

In the present study however, the excitation energies used are greater than the ZnS bandgap ($E_{g,ZnS} \sim 3.6$ eV). Hence, the PL efficiency is likely to dependent on the crystallinity since it involves mechanisms such as electron-hole pair generation and recombination, and energy transfer to luminescent centres.[20] Therefore, it is believed that the sharp increase in PL seen on Fig. 4 is due to the recrystallisation of the phosphor layer (Fig. 2) and probably related to reduced point defects and non-radiative recombination as suggested by Cattel and Cullis.[12]

C. Electroluminescence intensity dependence on annealing

The direction of the electric field accelerating the electrons within a TFEL phosphor is perpendicular to the film surface, i.e., the cross-sectional direction. Y. Nakanishi and G. Shimaoka concluded that the ZnS:Mn films consisting of a single fibre structure with the [111] axis nearly perpendicular to the substrate and good crystallinity in the cross-sectional direction give the best EL results.[1] They also reported that deterioration in the ZnS (111) orientation increases grain boundaries in the films that decrease the electron mean free path.

Accordingly, the improvement in the (111) orientation of our annealed ZnS:Mn phosphor (Fig. 2) will increase the electron mean free path, i.e. reduce their energy loss through collisions with stacking defects in the active layer.

Moreover, in Section IVB, we suggested that the number of point defects, favouring non-radiative recombination, are decreased after a thermal treatment at 600 °C which should further increase the device performance.[21]

Also, detailed EL decay-time studies by H. Xian, et al., have shown that the excitation and radiative efficiencies of TFEL devices are increased when improving the crystallinity of the active layers.[7]

In the present study, the electroluminescence analysis shows that the TFEL device performance is improved as the annealing temperature is raised from 400 °C to 500 °C, which is consistent with the reported luminescent properties improvement of the phosphor layer, i.e. PL increase (Fig. 4). However, from 500 °C to 700 °C, the EL operating intensity saturates despite the beneficial recrystallisation effects on the luminescent and electronic properties of the active layer as discussed above, and the

increased number of active Mn^{2+} ions (See Section IVB).

A modelling of this behaviour by W. M. Cranton, et al., based on electrooptic characteristics, indicates that this EL saturation is due to a modification of the interface states density at the phosphor / dielectric boundary.[10] Other research groups who investigated the thermal annealing effects upon bottom and upper interfaces via polarisation measurements arrived to the same conclusion.[8,9]

The high annealing temperatures resulting in EL saturation correspond to the maximum $ZnS:Mn$ / Y_2O_3 lattice misfit values reported in Table III. Obviously, the lattice misfit plays an important role in the nature of the electronic interface since it generally contributes to formations of, for example, dislocations, defects, and dangling bonds. Such increase in dangling bonds and defects may generate a more uniform interfacial electron energy distribution and un-pin the Fermi level of $ZnS:Mn$ which was suggested to be crucial for the generation of so-called hot electrons (see Chapter 1).

In other words, it is suggested that the increase in lattice misfit may reduce the amount of electrons reaching optical energies and thus, reduces the performance of TFEL devices.

Finally, a further annealing effect at temperatures >=500 °C, is the recrystallisation of the insulator layer in the <111> direction (Fig.3) which was related to defects and stress removal. This is consistent with recent dielectric measurements that showed an increase in the Y_2O_3 breakdown strength with increasing annealing temperatures >=500 °C.[22]

V.   SUMMARY

The dependence of thermal annealing temperatures on the crystallinity, photoluminescence, and electroluminescence properties of TFEL structures was systematically investigated. The main results are summarised as follows:

(i) The insulating and phosphor thin films constituting the TFEL devices are preferentially oriented in their <111> direction. The extend of preferred growth in the <111> direction is lower when ZnS:Mn is deposited on the sputtered Y_2O_3 layer than when directly deposited on Si (100).

(ii) Thermally annealing the ZnS:Mn / Y_2O_3 multilayers generates recrystallisation of both layers at temperatures of respectively 500 °C and 600 °C. The lattice misfit between both layers increases with annealing and reaches its maximum value with treatment temperatures >=500 °C.

(iii) Upper band-gap photoluminescence analysis shows that the luminescence properties of the phosphor layer improve sharply above 500 °C due to recrystallisation.

(iv) The performance of our TFEL device saturates at 500 °C although the electronic and luminescent properties of the active layer are improved. It is suggested that the lattice misfit increase modifies the morphology of the phosphor / insulator interface, which reduces the number of potential hot electrons.

REFERENCES

[1] Y. Nakanishi and G. Shimaoka, J. Vac. Sci. Technol. A **5** (4), 2092 (1987).

[2] S. Takata, T. Minami, and T. Miyata, Thin Solid Films **193/194**, 481 (1990).

[3] H. Xian, P. Benalloul, C. Barthou, and J. Benoit, Thin Solid Films **248**, 193 (1994).

[4] J. A. Ruffner, R. T. Tuenge, S. Sun, P. D. Grandon, P. F. Hlava, Thin Solid Films **310**, 123 (1997).

[5] H. Venghaus, D. Theis, H. Oppolzer and S. Schild, J. Appl. Phys. **53**(6), 4146 (1982).

[6] T. Matsuoka, J. Kuwata, M. Nishikawa, Y. Fujita, T. Tohida, and A. Abe, Jpn. J. Appl. Phys. **27**(4), 592 (1988).

[7] H. Xian, P. Benalloul, C. Barthou, and J. Benoit, Jpn. J. Appl. Phys. **33**, 5801 (1994).

[8] T. Matsuoka, M. Nishikawa, J. Kuwata, Y. Fujita, T. Tohida, and A. Abe, Jpn. J. Appl. Phys. **27**(8), 1430 (1988).

[9] A. Aguilera, S. Bhaskaran, A. Garcia, D. Parker, W. Wu, J. C. McClure, and V. P. Singh, SID **94** Digest, 452 (1994).

[10] W. M. Cranton, R. Stevens, C. B. Thomas, A. H. Abdullah, and M.R. Craven, Poc. IEE Colloquium on Materials for Displays, 1995.

[11] *Handbook of Chemistry and Physics*, 78ᵗʰ ed., edited by D. R. Lide (1997-1998).

[12] A. F. Cattel and A. G. Cullis, Thin Solid Films **92**, 211 (1982).

[13] K. Onisawa, M. Fuyama, K. Tamura, K. Taguchi, T. Nakayama, Y. A. Ono, J. Appl. Phys. **68** (2), 719 (1990).

[14] D. B. Cullity, *Elements of X-ray Diffraction* (Addison-Wesley, Reading, MA,

1978).

[15] J. C. Jamieson and H. H. Demarest, J. Phys. Chem. Solids **41,** 963 (1980).

[16] W. J. Troff and M. E. Thomas, in: *Handbook of optical constants of solids II,* edited by E. D. Palik (Academic Press, 1991) p. 1079.

[17] H. Fukumoto, T. Imura, and Y. Osaka, Appl. Phys. Lett. **55** (4), 360 (1989).

[18] Y. Nakanishi, Y. Fukuda, Y. Hatanaka, and G. Shimaoka, Appl. Surf. Sci. **48/49,** 297 (1991).

[19] E. A. Mastio, W. M. Cranton, C. B. Thomas, E. Fogarassy, and S. de Unamuno, Appl. Surf. Sci. **139,** 35 (1999).

[20] R. Scheps, J.Lumin. **42,** 295 (1988).

[21] H. Sasakura, H. Kobayashi, S. Tanaka, J. Mita, T. Tanaka, and H. Nakayama, J. Appl. Phys. **52** (11), 6901 (1981).

[22] M. Sethu, private communication.

CHAPTER 7: Pulsed laser annealing for high efficiency thin film electroluminescent devices

I. INTRODUCTION

Following an initial period of investigation to determine the optimum experimental arrangement, multiple pulse laser irradiations of ZnS:Mn thin films have been demonstrated to provide drastic enhancements of photoluminescence but limited improvement of electroluminescence (Chapter 5).

Hence, the previous Chapter was aimed to study the effects of thermal annealing on the crystalline structure of TFEL devices in order to investigate their limitations on performance resulting from processing at high temperatures. It was found that the insulating and phosphor layers recrystallise at annealing temperatures of respectively 500 °C and 600 °C, and that their lattice misfit doubles at processing temperatures >=500 °C. Thus, according to the results presented in Chapter 1, the lack of improvement in electroluminescence beyond an annealing temperature of 500 °C was tentatively attributed to a modification of interface states density resulting from a lattice misfit increase between the phosphor and dielectric thin films.

In the present Chapter, these latter recrystallisation and lattice misfit results are used to assess the thermal effects generated by single pulse laser irradiation. These results will also be related to those obtained from the simulated surface and interface maximal temperatures attained during pulsed KrF laser annealing. Finally the concept and feasibility of the novel pulsed laser annealing method will be demonstrated by comparing the electroluminescence characteristics of both thermally and laser annealed TFEL devices.

II.   EXPERIMENTAL

A. Thin film deposition and annealing treatments

The depositions are based on ZnS:Mn (800 nm) / Y_2O_3 (300 nm) multilayers which were radio-frequency sputtered onto 4 inch Si (100) wafer-substrates within an argon pressure of 3 mTorr (see Chapter 2). Two such similarly coated wafers were used to study separately the crystalline and electroluminescent characteristics of the TFEL structures. The wafers are referred to as NTU259 and NTU324, respectively.

The wafer labelled as NTU259 was used in Chapter 6 to examine the thermal annealing effects on crystallinity. The post-deposition thermal annealing was performed in vacuum (1×10^{-7} Torr) for one hour on cleaved samples at treatment temperatures up to 600 °C. For the present study, other cleaved samples of the same wafer (NTU259) were laser annealed under 150 psi (~10.34 bars) of argon pressure, using the TITANIA facility at the Rutherford Appleton Laboratory. The TITANIA arrangement described in Chapter 3 provided energy densities up to 1026 mJ/cm^2 within an irradiation area of 2 cm × 2 cm. Small variation in the temporal duration (τ_p) arose using TITANIA and the power densities corresponding to the energy densities 130 ($\tau_p = 20.3$ ns), 473 ($\tau_p = 23.6$ ns), 578 ($\tau_p = 23$ ns), and 1026 mJcm^2 ($\tau_p = 21$ ns), are respectively 6, 20, 25, and 48 MW/cm^2.

Laser annealing of the wafer NTU324 was performed using a commercial KrF laser (see Chapter 2). To fabricate laser processed TFEL devices, an upper insulator

layer (300 nm of Y_2O_3) was grown after laser irradiation, followed by an indium tin oxide (ITO) electrode deposited by radio-frequency sputtering through a shadow mask. The design of the mask enabled electrical probing of the individually laser annealed and as-deposited regions.

During thin film deposition, the substrate temperature was maintained at 200 °C for the insulator and phosphor thin films growth, and at 450 °C during the one hour deposition of the ITO electrode. Hence, in the following, it is considered that the non-annealed regions for the XRD analysis (NTU259) and electroluminescence analysis (NTU324) are thermally annealed respectively at 200 °C and 450 °C for one hour.

B. X-ray diffraction and electroluminescence measurements

XRD patterns of the samples labelled NTU259 were obtained using reflections from the $CuK\alpha_1$ emission line (wavelength = 0.15405981 nm) into a Siemens D5000 diffractometer with front monochromator. The applied power of the x-ray tube was 35 KV × 25 mA, the angular step was 0.005 ° within the studied diffraction angle range (25° - 62°), and the quanta acquisition time was 20 seconds.

The NTU324 TFEL devices were driven with a constant sine wave frequency of 5 kHz. Electroluminescent brightness versus drive voltage were measured via a Minolta LS110 luminance meter placed at right angle to the samples to measure top-out emission through the ITO electrode.

III. RESULTS

A. Thermal simulation of the laser processing

Based on the results of the thermal simulation that were presented in Chapter 4, Figure 1 shows the calculated maximal transient temperatures attained at the phosphor layer surface and at the phosphor / insulator interface, as a function of incident laser power density.
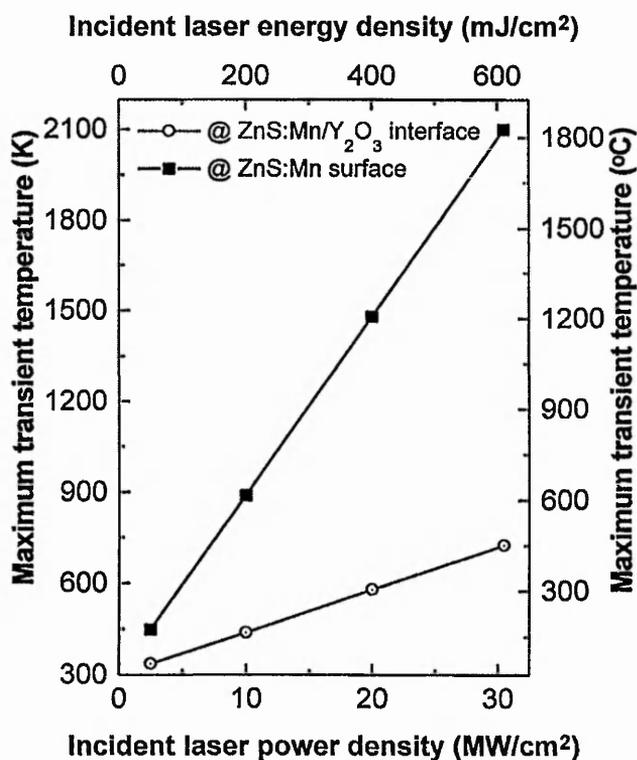
FIG. 1. Simulated maximal transient temperatures attained at the ZnS:Mn surface and the ZnS:Mn (800 nm)/ Y_2O_3 (300 nm) interface as function of incident KrF laser power density. The modelled rectangular laser pulse duration is 20 ns.

Both surface and interface temperatures are increasing linearly with laser power density, and their heating rates are 59 and 13.9 K/MW.cm^{-2}, respectively. In Chapter 2, the same simulated linear behaviour was exhibited when the phosphor was directly deposited on Si. The values of the heating rates at the ZnS:Mn surface and ZnS:Mn / Si interface were found to be 59 and 13.6 K/MW.cm^{-2}, respectively. Hence, under similar annealing conditions, the temperature attained at the phosphor / insulator interface is predicted to be slightly higher then the temperature attained at the phosphor / silicon interface. This is not surprising since the Y$_2$O$_3$ insulator is acting as a thermal buffer layer i.e. $k_{Si} > k_{ZnS} > k_{Y2O3}$ (k: thermal conductivity), (see Table I, Chapter 4).

Table I summarises the simulated surface and interface temperatures attained with the present experimental pulsed laser annealing conditions. According to the thermal model, the critical interface temperature of ~500 °C, at which changes of interface states density may occur (Chapter 1), is not reached even if the surface melts. It is important to recall that thermal simulations were based on the properties of single crystal ZnS and were not performed beyond the melting threshold since no empirical data exist for the optical and thermal properties in its liquid state.

TABLE I. Simulated maximal transient temperatures attained at the ZnS:Mn surface and the ZnS:Mn (800 nm)/ Y$_2$O$_3$ (300 nm) interface during KrF laser processing at varying incident laser power densities (P_d).

P_d	(MW/cm^2)	6	17	20	25	30.5
$T_{surface}$	(°C)	381	1030	1207	1502	1826
$T_{interface}$	(°C)	110	263	305	374	451

B. X-ray diffraction analysis

Figure 2 shows selected diffraction angle ranges (27-32° and 55-57°) within the XRD patterns of thermally and laser annealed NTU259 samples. To facilitate visual comparisons, the XRD patterns of thermally annealed samples at temperatures of 600 °C, 500 °C, and 200 °C (deposition temperature) are reported from Chapter 6 [see Figs. 2(a)-(c)].

In Chapter 6, the observed diffraction lines within Figs. 2(a) to 2(c) were attributed to the predominantly cubic ZnS structure, i.e. ZnS (111) and ZnS (311), and to the cubic bixbyite Y_2O_3 structure, i.e Y_2O_3 (222). Their approximate positions measured from the as-deposited sample [Fig. 2(c)] are represented as vertical dashed lines for reference.

As mentioned in the introduction, it was found that the insulating and phosphor layers recrystallise at annealing temperatures of respectively 500 °C and 600 °C [see Figs. 2(a)-2(b)]. Also, the diffraction angles $2\theta_{111,ZnS}$, $2\theta_{222,Y2O3}$, and $2\theta_{311,ZnS}$ were observed to shift to higher scattering angles with increasing annealing temperatures, which was attributed to increases in thin film densities due to stress and defect removal.

Additionally, the $2\theta_{222,Y2O3}$ values were found to increase more rapidly than the $2\theta_{111,ZnS}$ values which induced an increase in the lattice misfit between the phosphor and dielectric thin films.
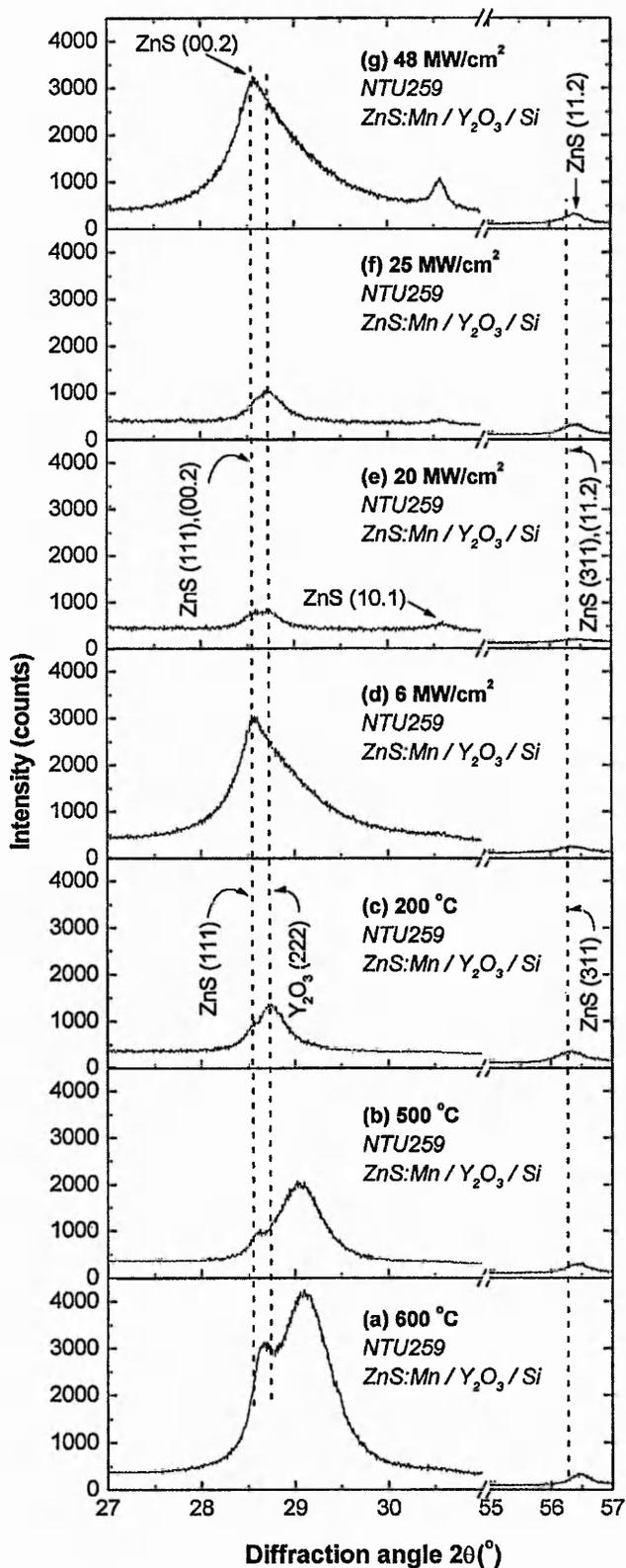
FIG. 2. XRD patterns of samples thermally annealed at 600 °C (a), 500 °C (b), 200 °C (deposition temperature) (c), and pulsed laser annealed under incident laser power densities of 6 MW/cm² (d), 20 MW/cm² (e), 25 MW/cm² (f), and 48 MW/cm² (g).

Figures 2(d) to 2(g) represents the partial XRD patterns of the pulsed laser annealed ZnS:Mn / Y_2O_3 multilayers with varying impinging laser power densities.

Firstly, a qualitative examination of the complete XRD pattern suggests that the phosphor layer remains predominantly cubic when irradiated with a laser power density of 6 MW/cm^2 [Fig. 2(d)], for the lack of noticeable diffraction from any hexagonal planes. Moreover, the absolute intensity of its cubic ZnS (111) diffraction peak is increased (~3000 counts) compared to the ZnS (111) intensity of the as-deposited sample (~1000 counts) [Fig. 2(c)].

On the other hand, the XRD patterns of the samples annealed at laser power densities of 20 and 25 MW/cm^2 exhibit the ZnS (10.1) diffraction line [see Figs. 2(e)-(f)] which is representative of the hexagonal form of zinc sulphide. As a further evidence for this hexagonal structure formation, it is noted that within the full diffraction angle range (25°-62°), the hexagonal ZnS (10.2) and ZnS (10.3) lines appear as well. Hence, the previously observed ZnS diffraction lines in Figs 2(a) to 2(d) are identified as ZnS (111),(00.2) and ZnS (311),(11.2) since they may now be made up of two unresolved lines from planes of nearly the same spacing and indicative of both cubic and hexagonal phases (see Chapter 3).

By increasing the incident laser power density up to 48 MW/cm^2 [Fig. 2(g)], the ZnS (10.1) peak increases strongly as well as the other ZnS diffraction lines whose absolute intensities are of the order of those seen in Fig. 2(d). Hence, it is anticipated that the phosphor layer becomes predominantly hexagonal as opposed to predominantly cubic and all observed ZnS diffraction lines are attributed to the hexagonal structure, i.e., ZnS (00.2) and ZnS (11.2).

Furthermore, in a manner similar to that observed for the thermally annealed samples, the diffraction angles corresponding to the laser annealed phosphor shift to higher scattering angles with increasing laser power density [see $2\theta_{311,ZnS}$, $2\theta_{311,11.2,ZnS}$, and $2\theta_{11.2,ZnS}$ in Figs. 2(d)-(g)]. However, the laser annealing treatment does not affect the position of the Y_2O_3 (222) line as distinctively as the thermal annealing process [see $2\theta_{222,Y2O3}$ in Fig. 2], which will lead to smaller lattice misfits between the ZnS:Mn and Y_2O_3 layers.

Also, the absolute maximum intensity of the Y_2O_3 (222) line is undoubtedly smaller with laser processing (<3000 counts) [Figs. 2(d)-(g)] than the intensity measured on thermally annealed samples up to a temperature of 600 °C (>4000 counts) [Fig. 2(a)]. This may suggest that using laser power densities up to 48 MW/cm^2, the processing temperatures attained within the insulator layer are lower than 600 °C.

In the following, the diffraction characteristics of both phosphor and insulating structures will be quantitatively investigated in order to investigate the thermal effects of pulsed laser annealing. Hence, the diffraction curves involving the ZnS (111), ZnS (00.2), and Y_2O_3 (222) lines within Figs. 2(d) and 2(g) were deconvoluted using the Laurenzian approximation. Note that since the diffraction curves involving the unresolved lines ZnS (111),(00.2) in Figs. 2(e) and 2(f) are difficult to process numerically, the samples irradiated with laser power densities of 20 and 25 MW/cm^2 were not investigated quantitatively.

Table II summarises the deconvoluted diffraction characteristics of thermally and laser annealed samples. Also reported are the results of the lattice parameters and lattice misfit calculations which have been formulated in the thermal annealing study

(Chapter 6).

However, the lattice misfit calculation of the laser annealed samples needs further precautions since by definition, the phosphor lattice parameters to consider for the ZnS:Mn / Y_2O_3 lattice misfit calculation are the lattice constants of the crystallites close to the interface. Yet, due to the non-homogeneous temperature profiles within the phosphor layer during pulsed KrF laser annealing (see Chapter 4), the phosphor crystallites at the interface are likely to have different lattice constants to those in the bulk of the ZnS:Mn layer. Hence, for this particular exercise, the lattice constant of the non laser annealed ZnS:Mn structure (as-deposited) is used to calculate the lattice misfits of laser annealed samples.

In Table II, it is shown that the $2\theta_{222,Y2O3}$ values measured from laser annealed samples are smaller than the $2\theta_{222,Y2O3}$ value measured after a thermal treatment at 500 °C. Consequently, the lattice misfit of the ZnS:Mn / Y_2O_3 multilayer irradiated with the maximum laser power density of 48 MW/cm^2 is smaller than the lattice misfit determined from the thermally annealed structure at the critical temperature of 500 °C. Furthermore, for the discussion in Section IVB, it is important to emphasis here that the so calculated lattice misfits are more likely to be greater than the real values since the measured diffraction angles corresponding to the phosphor lattice are shifting to higher scattering angles with increasing laser power density (Table II).

Finally, the computed integrated intensities $I_{111,ZnS}$, $I_{00.2,ZnS}$, and $I_{222,Y2O3}$ confirm the laser recrystallisations of the ZnS:Mn and Y_2O_3 structures using laser power densities of 6 and 48 MW/cm^2.

TABLE II. Results of the diffraction characteristics and phosphor / insulator lattice misfit $1 - (a_{Y2O3}/2a_{ZnS})$ determined for the thermally annealed and laser annealed NTU259 samples. $2\theta_{111,ZnS}$ and $2\theta_{222,Y2O3}$ are the measured diffraction angles of the ZnS:Mn (111) and Y_2O_3 (222) lines. $d_{111,ZnS}$ and $d_{222,Y2O3}$ are their interplanar spacings. $I_{111,ZnS}$ and $I_{222,Y2O3}$ are the integrated intensities of their deconvoluted diffraction lines. $I_{00.2,ZnS}$ is the integrated intensity of the deconvoluted ZnS (00.2) diffraction line. a_{Y2O3} and a_{ZnS} are the determined lattice constants of the insulator and phosphor layer respectively. (*) Lattice misfits calculated using the phosphor lattice parameter of the thermally annealed sample at 200 °C (as-deposited).

NTU259		Thermal annealing temp. (°C)			P_d (MW/cm^2)	
		200	500	600	6	48
$I_{222,Y2O3}$	(a.u.)	599±2	1642±17	4320±36	1903±80	2394±89
$I_{111,ZnS}$	(a.u.)	20±4	54±4	648±13	1114±45	-
$I_{00.2,ZnS}$	(a.u.)	-	-	-	-	1383±50
$2\theta_{222,Y2O3}$	(°)	28.75	29.05	29.10	28.92	28.94
$2\theta_{111,ZnS}$	(°)	28.53	28.58	28.64	28.56	-
$d_{222,Y2O3}$	(nm)	0.31026	0.30712	0.30652	0.30843	0.30820
$d_{111,ZnS}$	(nm)	0.31256	0.31200	0.31134	0.31229	-
a_{Y2O3}	(nm)	1.0747	1.06389	1.06181	1.06843	1.06764
a_{ZnS}	(nm)	0.54136	0.54039	0.53925	0.54074	-
$1 -$						
$(a_{Y2O3}/2a_{ZnS})$	(%)	0.73	1.56	1.54	1.31 (*)	1.39 (*)

C. Electroluminescence analysis

TFEL devices based on the NTU324 wafer deposition were laser annealed by single pulse irradiation of 13, 14, 17, 23, 26, 30, 36, 37, 39, and 44 MW/cm^2. No significant improvement of the device performance was measured below 17 MW/cm^2. From 17 MW/cm^2 to 44 MW/cm^2, the electroluminescence brightness was improved by 200% to 400% compared to thermally annealed devices at 450 °C.

Figure 3 shows the best result obtained by single pulse laser processing which is compared to the brightness-voltage characteristics of the thermally annealed NTU324 TFEL structures. Unequivocally, the electroluminescence performance of the laser annealed structure, using a single shot of laser irradiation at 44 MW/cm^2, is improved compared to equivalent devices thermally annealed at 450 °C for 1 hour. In fact, the laser processed device exhibits a sharper turn-on slope and its brightness (not saturated) is more than fourfold the saturation brightness obtained with the conventional thermal treatment.
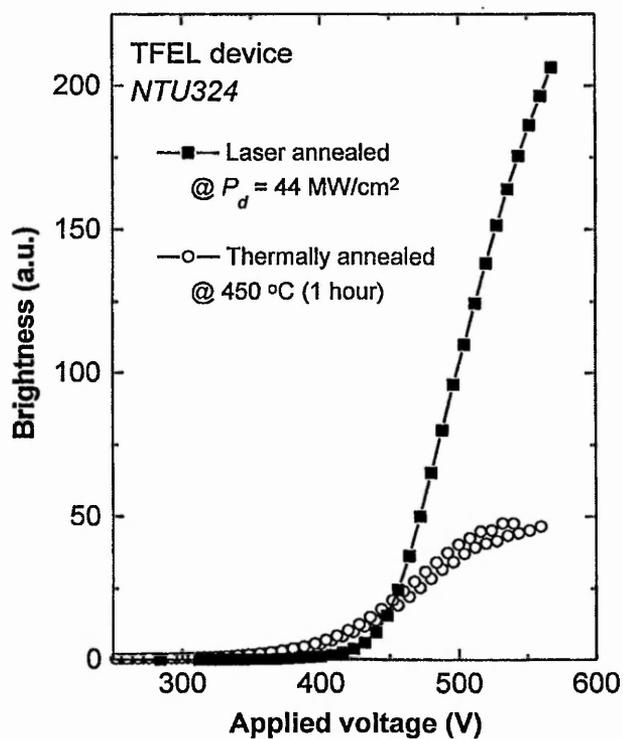
FIG. 3. Brightness-Voltage characteristics of samples thermally annealed in vacuum at 450 °C during 1 hour, and KrF pulsed laser annealed with one pulse irradiation of 44 MW/cm^2. Devices driven by a 5 kHz sine wave.

IV. DISCUSSION

A. Structural dependence on laser annealing conditions

In Chapter 6, it was reported that ZnS:Mn recrystallises at a thermal annealing temperature of 600 °C when deposited on Y_2O_3 (Table II) whereas no recrystallisation was measured when ZnS:Mn was directly deposited on Si and annealed at temperatures up to 700 °C (see Chapter 3). This dependence of thermal recrystallisation on substrate was attributed to a poorer crystalline quality of the as-grown phosphor deposited on Y_2O_3 compared with direct growth on Si. Interestingly, a similar substrate dependence on laser recrystallisation is also confirmed by the results presented in Chapter 3. Indeed, no structural modification of the ZnS:Mn coated Si samples was measured with TITANIA irradiations at ~10 MW/cm^2 whereas here, the XRD results show recrystallisation of the ZnS:Mn / Y_2O_3 multilayers irradiated with a laser power density of 6 MW/cm^2 (Table II).

At this latter laser power density, the Y_2O_3 layer recrystallises as well, suggesting that the surface and interface temperatures attained are respectively, >600 °C and >500 °C (Table II). However, the $2\theta_{111,ZnS}$ and $2\theta_{222,Y2O3}$ values obtained by laser processing are smaller than the values obtained by thermal annealing at 500 °C during 1 hour (Table II). This may be due to shorter treatment times and higher cooling rates involved with nano-second pulsed laser annealing as demonstrated in Chapter 3. Hence, although treatment temperatures of the order of those used with thermal annealing may be reached, the laser annealing process may be less effective

for stress and defect removal within the deposited structures, which has been ascribed to increases in lattice constants and densities (Chapter 6).

The simulated surface and interface temperatures attained using a laser power density of 6 MW/cm^2 are respectively, 381 °C and 110 °C (Table I), which are too low according to the XRD analysis (Table II). Here it is important to remember that the thermal simulation was performed using the optical and thermal parameters of ZnS and Y$_2$O$_3$ single crystals that most probably differ from those of our polycrystalline thin films. More specifically, considerable non-uniform structures have been reported at the phosphor / insulator boundary, i.e., within the so-called dead layer (~50 nm thick).[1,2,3]

The XRD patterns of samples exposed with laser power densities of 20 and 25 MW/cm^2 [see Figs. 2(e)-(f)] exhibit the cubic to hexagonal transformation which conforms with the simulated transition threshold of 17 MW/cm^2 (Table I). From the discussion above, it may be surprising that with laser annealing conditions generating temperatures within the phosphor layer greater than 1030 °C ($T_{transition,ZnS}$), no Y$_2$O$_3$ recrystallisation is observed. It is believed that this behaviour is inherent to the allotropic transition itself due to the thermal energy used during the solid state transformation (latent heat). In the previous ablation rate study (Chapter 4), it was suggested that when significant absorption of radiation is providing the latent heat of phase transformation, the surface temperature might be lowered as well. Moreover, in Chapter 3, the hexagonal lattice planes formation, within the ZnS:Mn structure directly deposited on Si, was demonstrated to occur by reduction of the cubic form, e.g. a decrease of the ZnS (111) peak intensity. Hence, the fact that the preferential

growth in the <111> direction is not increased at laser power densities of 15 and 20 MW/cm^2 is a further consequence of the phase transition.

When higher irradiation levels are used, i.e., 48 MW/cm^2 [Fig. 2(g)], both the phosphor and insulator layers recrystallise, i.e., new grains are formed that fulfil the Bragg diffraction law.[4] Thus, it is believed that the excess of optical energy generates both the phase transition and formation of new wurzite crystallites within ZnS:Mn. According to the results of the thermal model, the maximal surface temperature attained using 48 MW/cm^2 should exceed the melting point of ZnS:Mn (Section IIIA). A study of the average crystallite diameter within the phosphor layer using the Sherrer equation[5] did not show significant grain growth. This suggests that the predicted laser melt-regrowth process may remain close to the surface while the effective phase transition and recrystallisation depths increase (see Chapter 3).

Finally, the cubic to hexagonal phase transition coincides with the increase in photoluminescence seen in Chapter 5. This may confirm that the improvement in the host environment for the dopant ions results from the induced solid state transformation as suggested in Chapter 2.

B. The performance of laser annealed TFEL devices

In the past, various approaches have been taken to treat the phosphor layer at high temperatures without damaging the commonly used glass substrate. One of such approach has been shown by H. S. Reehal and J. M. Gallego[6] who investigated nanosecond pulsed laser melting, under high inert gas pressure, to diffuse and activate pre-implanted Mn ions within the ZnS lattice. Another application of the laser melt-regrowth approach was suggested by Johnson, et al., who proposed to melt the zinc sulfide layer using a CW laser with high power density.[7] However, while both methods may be relevant for d.c. electroluminescence, the problem with both approaches is that the substantial improvement of the device is obtained by generating a deep melt front that may reduce the interface states in an a.c. operated device. Very recently, to overcome this problem, Y. F. Kononets investigated low-power pulsed ultraviolet radiation, below laser annealing threshold, to photo-stimulate below-defect annealing processes and impurity diffusion within ZnS:Mn.[8] However, so far, the reported electroluminescence intensity obtained using the latter treatment technique are less than 15% better than the intensities obtained from the initial (as-grown) TFEL structures.

In the present work, TFEL device brightness obtained by pulsed KrF laser annealing can be increased by at least 400% compared to the brightness of a device thermally annealed at 450 °C. Using this technique, improvements of the device performance occured at laser power densities between 14 and 17 MW/cm^2. In Chapter 5, the sub-bandgap photoluminescence analysis of similar thermally and laser annealed structures show that the number of active Mn^{2+} ions increase sharply

above 15 MW/cm^2 before reaching a maximal value from ~20 MW/cm^2 to ~50 MW/cm^2. According to the photoluminescence dependence on thermal annealing temperature shown in Chapter 5, the amount of active Mn^{2+} ions exhibited by a thermally annealed phosphor at 450 °C should be smaller by less than 30% compared to a thermally annealed phosphor at 500 °C. Hence the drastic differences between the electroluminescence results obtained by thermal and single pulsed laser processing are not attributed to solely the improved number of active luminescent centers.

In agreement with the results of the preliminary study of ZnS:Mn directly deposited on Si (See Chapters 2 and 3), and with the XRD and thermal model results shown in the present Chapter, it is evidenced that the photoluminescence and electroluminescence improvements are exhibited by devices composed of phosphor layers possessing a distinctive hexagonal structure. Consequently, it could be supposed that the hexagonal form of zinc sulphide might be more efficient for electroluminescence applications than its cubic form, but to the author's knowledge, no such evidence has been reported and it is premature to draw that conclusion.

As suggested in Chapter 2, the allotropic transition of ZnS may play a role in the activation of the Mn^{2+} ions by laser annealing. In Chapter 3, the short processing times involved in pulsed laser annealing were reported to inhibit solid-state grain growth although suitable processing temperatures were attained within the phosphor layer according to previous work. Similarly, it might be possible that these short processing times inhibit solid-state Mn^{2+} activation, e.g., via solid-state diffusion[9] processes. Consequently, it is supposed that the onset for luminescent improvement

coincides with the threshold for solid-state phase transition, which may provide the lattice rearrangement conditions necessary for impurity activation. Hence, it is inferred that by favouring the transition between the two stable allotropes of the ZnS lattice, the dopant ions can be efficiently laser activated without the obligation of melting the entire thin film as in Ref. 6. Moreover, the XRD study shows that the lattice misfit values obtained by pulsed KrF laser annealing up to power densities of 48 MW/cm^2 are lower than the value obtained by thermal annealing at the critical temperature of 500 °C. Therefore, it is preferably supposed that the improved TFEL performance achieved by pulsed laser annealing is due to the provision of high luminescent efficiencies of the phosphor layer without detrimental modifications at the electronic interface, i.e., of the interface states density.

Finally, the sputtering technique used for the deposition of our phosphor films provides high growth rates at substrate temperature of ~200 °C. At this substrate temperature, the as-grown sputtered zinc sulphide films are polytype (with a preferential cubic structure), which may lead to defect formations and unstable properties within the TFEL device structures.[10,11] Hence, this issue may be of further interest for the development of the laser annealing processing since such a technique may provide a post-deposition annealing method for obtaining monotype (wurzite) phosphors.

V. CONCLUSION

In agreement with the thermal model of the laser-matter interaction and previous results, it is suggested that the pulsed laser annealing technique improves the luminescent efficiencies of thin film electroluminescent phosphors by generating an in-depth solid state phase transition. Moreover, the XRD characteristics analysis of thermally and laser annealed devices, demonstrates that the KrF laser processing generates high annealing temperatures within the phosphor layer but without detrimental heating effects at the insulator boundaries. It is also suspected that the short processing times involved during pulsed laser annealing are also advantageous in preserving a suitable lattice misfit between the phosphor and insulator layers.

Thus, the TFEL performance is improved, exhibiting high brightness as well as sharp turn-on slopes that are important requirements for matrix addressing.

To conclude, these results are in agreement with the lattice misfit model and validate the viability of this novel laser treatment technique as an alternative to conventional thermal annealing.

REFERENCES

[1] A. N. Krasnov, R. C. Bajcar, and P. G. Hofstra, J. Crystal Growth **194**, 53 (1998).

[2] H. Venghaus, D. Theis, H. Oppolzer and S. Schild, J. Appl. Phys. **53**(6), 4146 (1982).

[3] Y. Takeuchi, Y. Okuno, T. Nakamura, K. Ishino, A. Ishida, and H. Fujiyasu, Jpn. J. Appl. Phys. **31**, 1391 (1992).

[4] D. B. Cullity, *Elements of X-ray Diffraction* (Addison-Wesley, Reading, MA, 1978).

[5] B. E. Warren, *X-ray diffraction* (Dover, New York, 1990), p. 253.

[6] H. S. Reehal and J. M. Gallego, C. B. Edwards, Appl. Phys. Lett. **40,** 258 (1982).

[7] Johnson, U.S. Pat. No. 4 442 136, published Oct. 1984.

[8] Y. F. Kononets, Tech. Phys. Let. 24 (1998) 124.

[9] J. M. Hurd and C. N. King, J. Electronic Materials **8**, 879 (1979).

[10] L. E. Tannas, *Flat Panels Displays and CRTs* (Van Nostrand, Princeton, 1985), p. 260.

[11] M. A. Herman, *Optoelectronic Materials and Devices* (1981), p. 144.

CHAPTER 8: Conclusions and Further work

I.   Conclusions

The crystalline study of laser annealed ZnS:Mn phosphors, either deposited on Si or on Si coated with Y_2O_3, showed that single pulse KrF laser irradiation generates an in-depth crystallographic phase transition within ZnS:Mn, which is suggested to be concomitant with the density increase of active luminescent centres. The calculated thermal diffusion length of ZnS:Mn (~1021 nm) is of the order of its thickness (800 nm) and according to the thermal model, little heating effects are expected at the underlying interfaces during the solid state phase transition.

Although modifications of buried interfaces are difficult to assess experimentally, XRD results obtained from thermally and laser annealed samples permitted to probe the heating effects generated by laser processing at the ZnS:Mn / Y_2O_3 interface. It was concluded that if temperature is a crucial annealing factor for TFEL applications, annealing time is of equal importance. Indeed, in the early stages of this work, it was shown that although high temperature profiles can be generated within the phosphor layer by laser annealing, high heating and cooling rates restrain grain growth. Moreover, this time dependent annealing effect on crystallinity was suggested to play a further role at the phosphor / insulator interface since it prevents detrimental lattice misfit increase when single pulse laser irradiation are used. Therefore, such laser annealed TFEL devices can benefit of the increase of active Mn^{2+} ions, explaining enhanced electroluminescent efficiencies.

Concerning the thermal model developed at PHASE laboratory, good agreements were met between the simulated surface temperature and experimental

observations. However, the predicted temperatures at the phosphor / insulator interface are low according to experimental XRD observations. These differences are suggested to occur from the use of unsuitable thermal parameters and/or from non-uniform structures within the polycrystalline thin films.

To conclude, from a technological viewpoint, the benefits achieved from this programme are undoubtedly highlighted by the improvement of laser annealed TFEL device performance compared to conventional treatment.

Scientifically, this study has been of equal importance, examining as it does, the dependence of annealing on the interface structure and its related effects on B-V characteristics. This, in an area that is far from being understood, and which historically has been approached from an empirical basis.

II.   Further work

As mentioned in the introductory chapter, a major objective of the future TFEL development is to extend its technology to encompass full colour display applications, which requires high device performance so that the low efficiency blue phosphors, such as ZnS:Tm,F may be efficiently used. Green and red emission using ZnS host lattices are available by filtering the broad band emission of the ZnS:Mn phosphor. The reported electroluminescent efficiency of ZnS:Tm,F phosphors is ~1% of that obtained for the filtered ZnS:Mn phosphor.[1] However, for full colour display applications, the relative luminance levels required are 66% of green, 27% of red, and only 8% of blue,[2] suggesting that blue ZnS:Tm,F phosphors can be

realistically employed if the overall TFEL device efficiency is improved.

By single pulse KrF laser processing, the electroluminescence brightness of ZnS:Mn has been increased by a factor greater than 4 compared to conventional thermal treatment, and laser processing will be shortly tested for full colour applications. Nevertheless, this novel annealing technique is far from being optimised. Indeed, the sub-bandgap photoluminescence analysis and the ablation study (Chapters 4 and 5) suggest that using multiple laser irradiation, the density of activated luminescent centres can still be increased further by a factor of at least 2 (see page 5-7). However, a concomitant modification of the electronic interface was inferred to limit the multiple pulse irradiation technique. Hence, it is suggested that to further improve the electroluminescent characteristics by benefiting from the increased number of active Mn^{2+} ions within the ZnS host lattice, a better heat conducting insulator layer may be used and/or multiple irradiations with decreasing power densities for the successive pulses.

To limit the loss of material by laser ablation, i.e. to increase the ablation threshold, one could also try to lower the substrate temperature during laser irradiation in order to favour higher cooling rates, reducing surface sublimation. More, the gas pressure may be further increased and/or the environment medium may be modified altogether. For example, gas or liquids having higher thermal conductivity and/or higher densities may be employed. Moreover, it would be also desirable to use a reactive medium containing sulphur, such as H_2S gas, since it has been shown that processing of TFEL phosphors within H_2S can greatly enhance the luminescent properties of ZnS films.[3]

From a more scientific approach, more insight into the effects of laser processing would be gained by performing:

(i)   Pulsed electroluminescence measurements to assess the laser annealing effects on the electron injection behaviour from the lower and upper phosphor / insulator interfaces.

(ii)   Transient photoluminescence and electroluminescence analyses of thermally and laser annealed samples prior to and after laser processing in order to evaluate the effects of both annealing methods on radiative efficiencies.

(iii)   Reflection of high energy electron diffraction (RHEED) and/or low angle XRD analyses to identify surface melting effects and eventual grain melt-regrowth effects.

(iv)   Scanning electron microscope (SEM) and/or scanning transmission electron microscope (STEM) investigations to identify microstructure changes generated by laser annealing.

(v)   Polarisation and angular measurements of the emitted luminescence as a function of crystallinity and surface morphology.

Some of these investigations are presently being undertaken by D. Koutsogeorgis who is working on this exciting project within his PhD research programme.

References

[1] P. Rack and P. Holloway, Mater. Sci. and Eng. **R21**, 171 (1998).

[2] L. E. Tannas, *Flat Panels Displays and CRTs* (Van Nostrand, Princeton, 1985).

[3] C. Tsakonas and C. B. Thomas, J. Appl. Phys. **78** (9), 3979(1995).

APPENDIX A: Conversion factors

The following table gives various conversions factor for luminance and pressure units used in this work.

To convert from	To	Multiply by
Foot-lambert (fL)	Candela / square meter	3.426259
	Lambert	1.076391×10^{-3}
Pound-force/square inch (psi)	Atmosphere	0.068046
	Bar	0.0689476
	Pascal	6894.76

Reference: *Handbook of Chemistry and Physics*, 78th ed., edited by D. R. Lide (1997-1998).

APPENDIX B: Shadow mask designs for ITO depositions

The two following drawings represent the designs used to manufacture the ITO shadow masks. The external dimensions of the mask perfectly fit the 4-inch wafers used for thin film depositions enabling accurate alignment. They were designed to generate ITO dots with square (4mm x 4mm) or circular (1 mm Diam.) geometry.
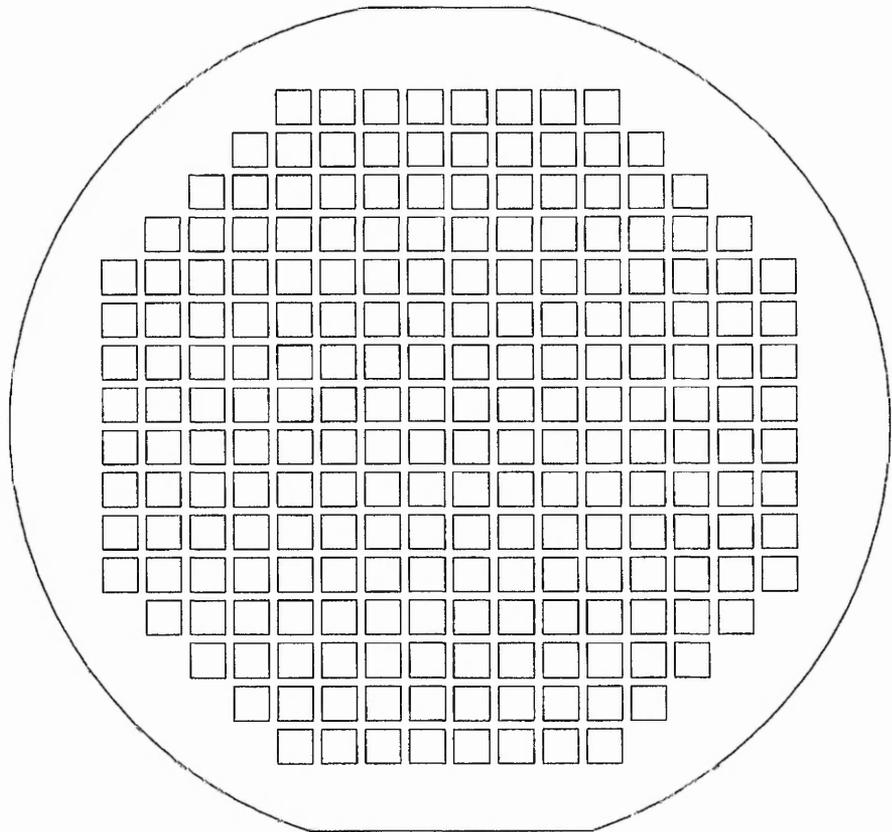
4 mm x 4 mm dots
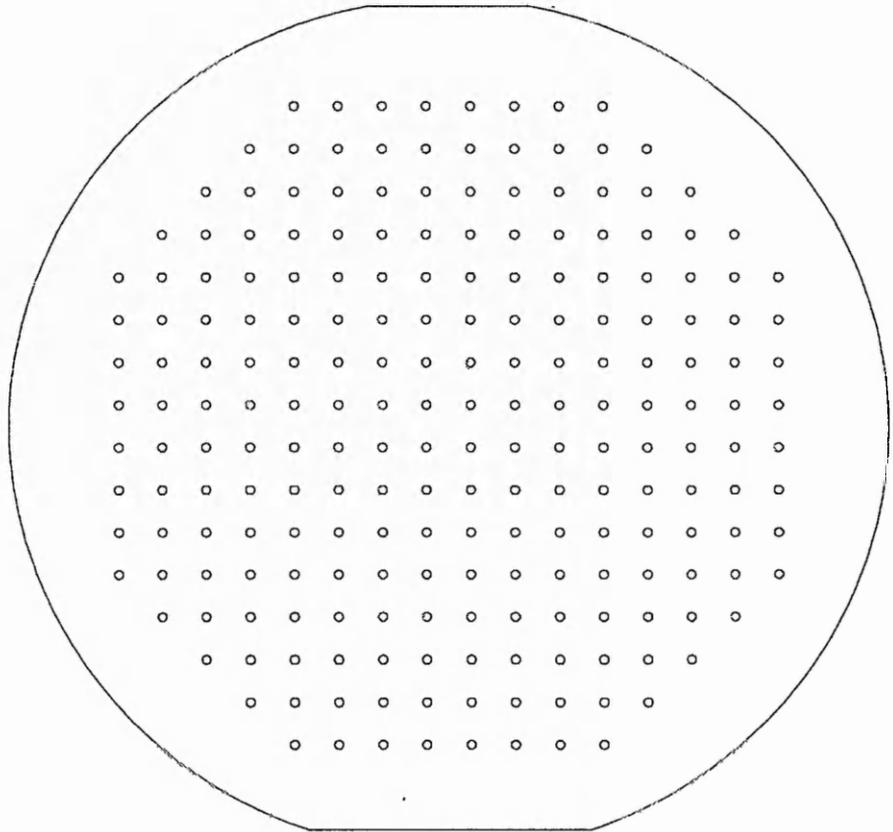
1 mm Diam. dots

PUBLISHED ARTICLES

The effects of KrF pulsed laser and thermal annealing on the crystallinity and surface morphology of radiofrequency magnetron sputtered ZnS:Mn thin films deposited on Si

E. A. Mastio,[a) M. R. Craven, W. M. Cranton, and C. B. Thomas
*Department of Electrical and Electronic Engineering, The Nottingham Trent University, Burton Street,
Nottingham NG1 4BU, England*

M. Robino
*Groupe d'Optique Non-Lineaire et d'Optoelectronic, Institut de Physique et Chimie des Materiaux
de Strasbourg, UM 380046, CNRS-ULP-ECPM, 23 rue du Loess, F-67037 Strasbourg Cedex, France*

E. Fogarassy
Laboratoire PHASE (UPR du CNRS no. 292), BP 20, 67037 Strasbourg Cedex 2, France

Thin films of ZnS:Mn (800 nm) have been deposited by rf magnetron sputtering onto 100 mm diam n-type single-crystal (100) Si wafers. Specifically for use as active layers in thin film electroluminescent devices, the films need a postdeposition annealing treatment to enhance their luminescent properties. Inherent to the later process step are structural modifications of the phosphor layer which form the basis of this study. Both pulsed laser and thermal postannealing techniques have been investigated. Reported are the induced crystalline and surface morphology modifications via x-ray diffraction and atomic force microscopy analysis. As-grown and thermally treated films were cubic in nature and no significant grain growth or reorientation occurred while heating up to 700 °C. Pulsed ($\sim$ 20 ns duration) KrF laser treated samples were annealed at power densities from 10.76 to 24.27 MW/cm^2 under 10.34 bar of argon pressure. Beam quality and diagnostics were emphasized during laser irradiation with particular attention brought to energy and pulse duration measurements. It has been demonstrated that at the power densities used, a gradual phase transition from cubic to hexagonal is occurring while the average crystallite size remains constant. Surface analysis highlights concomitance between the phase transition and the smoothening of the irradiated surface. A one dimensional thermal model of the pulsed laser annealing process shows that a surface temperature for crystalline ZnS equating to the transition temperature should be reached at 17 MW/cm^2, significantly below the numerically evaluated melting threshold of 30.5 MW/cm^2. Combining experimental and theoretical results, it is concluded that the phase transition occurs in the solid state. © *1999 American Institute of Physics.* [S0021-8979(99)05817-X]

I. INTRODUCTION

Thin films of zinc sulphide doped with manganese (ZnS:Mn) are of importance in the field of inorganic electroluminescence, particularly as the active layer in alternating current thin film electroluminescent (ACTFEL) devices.[1] The basic structure of the ACTFEL device is a phosphor layer, e.g., ZnS:Mn, sandwiched between two insulating thin films, e.g., Y_2O_3, $BaTiO_3$, etc. The stack of films is usually grown on glass or on silicon wafers as in the present work.

Electroluminescence arises from three successive mechanisms which are reported as tunnel emission of electrons from the phosphor–insulator interfaces followed by ballistic acceleration and impact excitation of the luminescence centers, e.g., manganese ions in ZnS:Mn. Device performances are therefore strongly related to: (i) the nature of the interfaces, i.e., the source of electrons, (ii) the crystalline quality of the active layer which determines carrier mobility, and (iii) the efficiency of the luminescent centers which determines the useful visible emission.

A critical manufacturing step of these devices is an annealing process, which is required to activate the dopant ions. Such annealing is typically performed by conventional thermal heating in a vacuum, at temperatures up to 500 °C for periods of typically 1 h.[2] Although higher processing temperatures would be of interest for higher luminescent efficiencies, there are limitations on the upper temperature range by either the type of substrate used or by the detrimental thermal substrate modifications of the interfaces. The latter has been shown to reduce excitation efficiencies when annealing at temperatures in excess of 500 °C.[3] Based on these limitations, it was proposed that the use of pulsed laser annealing could provide a more effective means of heat treating the phosphor thin films for ACTFEL devices.[4] By use of suitable wavelengths, it is intended to optimize the process so that the energy is dissipated primarily within the bulk of the ZnS thin films, with minimal effect upon the insulating layer(s) and hence the interface region(s). Previous investigations of a simple luminescent structure (800 nm of ZnS:Mn deposited on Si),[5] utilizing a commercial KrF excimer laser for pulsed laser annealing has demonstrated a lin-

---

a)Electronic mail: mastio@phase.c-strasbourg.fr

ear photoluminescence enhancement with increasing laser fluence. It was suggested that this improvement occurs in the solid state according to: (i) a thermal model of the laser processing[5] and (ii) the experimental results of previous work done on similar structures.[6]

The major goals of this article are to validate the thermal model for this simple structure of ZnS:Mn on Si, and to investigate the crystallinity and surface morphology produced by both conventional thermal annealing and the novel pulsed laser annealing process. It is not intended here to strictly compare thermal and laser annealing mechanisms since treatment times and the physical processes involved are different. However, via a discussion of the resultant effects of these two techniques, i.e., the diffraction and surface morphology characteristics produced in the ZnS:Mn thin films, we are able to partially validate the model. The crystallinity and surface morphology of the as-grown and annealed films are investigated using x-ray diffraction (XRD) and atomic force microscopy (AFM) analysis.

Finally, for a thorough understanding and traceability of the pulsed laser annealing effects, the accurate measurement of impinging optical energy is crucial. Therefore, different commercially available energy meters have been tested and cross calibrated in order to quantify the absolute laser fluences delivered to the samples.

II. EXPERIMENTAL AND ANALYSIS CONDITIONS

A. Thin film deposition and annealing

800 nm thick polycrystalline ZnS:Mn thin films were sputtered onto polished n-type single crystal (100) silicon wafers, from a pressed powder ZnS:Mn target. The Mn concentration of the source material is 0.45 wt %, i.e., $\sim 2.45 \times 10^{20}$ ions/cm^3. Growth was performed in an argon atmosphere at 3 mT using a cluster magnetron radio frequency deposition system, described previously.[7] An interferometric monitor was used to determine the film thickness during growth. The final thickness of 800 nm has been established by profile measurements from edges of the thin film to the noncoated Si areas, using a Dektak II surface profilometer. Its uniformity is determined to be better than $\pm 5\%$ across the 4 in. wafer. The substrate temperature was maintained at 200 °C during the 2 h deposition time. For reference, the deposition and target are, respectively, referred to as NTU228 and P116. To examine the effect of postdeposition annealing, the wafer was cleaved into 12 sections (~ 1 cm^2 each). This enables direct comparison of thermal and pulsed laser annealing of samples grown under the same conditions.

Postdeposition thermal annealing was performed on four of the cleaved samples in vacuum (1×10^{-7} T) for 1 h at temperatures of 400, 500, 600, and at a maximum of 700 °C. Limitation to 700 °C was due to thin film losses by delamination at higher temperatures. During annealing and growth, rotary motion of the samples ensured spatial uniformity of the process.

To achieve efficient absorption of the laser irradiation in the thin film, it is necessary to irradiate with photons of energy greater than the band gap (~ 3.66 eV for ZnS), since at lower energy these films are optically transparent.[8] With
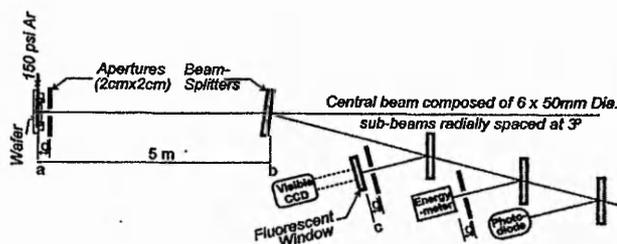

FIG. 1. Experimental arrangement for large area pulsed KrF laser irradiation using Titania Facility.

KrF laser emission of 249 nm corresponding to ~ 4.98 eV, the optical absorption coefficient α has been determined to be 3.33×10^5 cm^{-1} for crystalline ZnS and 3.15×10^5 cm^{-1} for polycrystalline ZnS:Mn thin films.[9,10] Irradiation of the samples was performed under 150 psi ($=10.34$ bar) of Ar pressure to prevent atmospheric contamination and either laser sublimation or ablation[11,12] due to the low ZnS vapor pressure at atmospheric pressure. The pressure cell (Fig. 1) in which the wafer was mounted is attached to a motorized micropositioning stage that facilitates irradiation of different areas of the sample for comparative analysis of relative laser power density.

TITANIA, a high power KrF laser facility at the Rutherford Appleton Laboratory (RAL) was used for irradiation, delivering up to 220 mJ/cm^2 via the combination of three 120 mm diam beams. The three main beams were used to focus six 50 mm diam subbeams onto the wafer, and a 2×2 cm aperture at the target plane was used to provide uniform beam characteristics over this area of irradiation. A range of fluences is obtained by selecting 1–6 subbeams. Essential for this experiment is the quality of the beam and associated diagnostics. Figure 1 shows the optical arrangement for irradiation and laser beam diagnostics, i.e., for measurement of the beam uniformity, energy and pulse duration (~ 20 ns).

B. Laser beam diagnostics and calibration

On-line diagnostics were performed using four beamsplitters. Each beamsplitter is a fused silica plate that transmits $\sim 92\%$ and reflects $\sim 8\%$ (Fresnel reflections) of the incident beam. The beam uniformity is determined via a charge coupled device camera imaging system and a window that fluoresces when excited by UV light. Since the beam impinging on the wafer is the result of focusing, the optical paths (ab) and (bc) were set to be equal (Fig. 1). The spatial uniformity of the energy distribution was determined to be better than $\pm 10\%$. The temporal duration τ_p of the pulse was measured with a vacuum photodiode and a digital storage oscilloscope. Small shot to shot variations in τ_p and in the detailed pulse shape arise from variations in the output of the discharge laser, which provides the initial pulse for amplification, and from differences between the six beams, which lead to a dependence of the pulse shape on the number of beams being used. Accurate and absolute measurements of impinging optical power density are critical for traceability,

TABLE I. Summary of the energy meter cross calibration. "Relative measure" is the percentage difference between expected and experimental values.

Energy meter	Sensitivity (mV/J)	Relative measure (%)
Scientec power meter (serial no.103)	2.05	100
Molectron J50	2000	100
Gentec ED-200	9290	122.2

reproducibility, and a thorough analysis. This is a nontrivial problem for powers of the magnitude investigated here, and cross calibration of energy meters is essential. Therefore, three commercially available energy meters have been tested for this particular experiment: a Gentec ED200, a Scientech No. 103, and a Molectron J50. Using the on-line arrangement, calibration and comparison of the three energy meters was performed by substituting the wafer with the Scientech, the Gentec with the photodiode and placing the Molectron at the energy meter position. Consequently, direct comparison between each meter was possible with a single shot. Assuming 92% transmission of the beamsplitters and pressure cell quartz window, the theoretical ratios between the signals measured on each of the energy meters are: Scientec/Molectron= 143.75 and Scientec/Gentec= 169.84. From the calibration system described previously, the measured mean ratios obtained with three different energy densities were Scientec/Molectron= 145.88±3 and Scientec/Gentec= 178.17±3. The Molectron and Scientech energy meters agree well with the theoretical value of 143.75 (assuming perfect beamsplitter). The Molectron was chosen for the pulsed laser annealing experiments owing to its high sensitivity at low detection levels, and compatibility with the Scientech system.

Table I summarizes the energy meter cross calibration results. The Scientech is taken as a reference since it measures the energy directly impinging on the wafer. In our particular experiment, the Gentec meter consistently gave results between 10% and 25% higher than those measured via the other two meters. Hence, for the results presented here, the energy densities reported are those determined via the Molectron placed at the energy meter position as shown in Fig. 1. A list of the measured irradiation fluences (area $= 4$ cm^2) and pulse duration with corresponding power densities P_d, obtained by blocking one to five beams, is given in Table II.

C. Crystallinity and surface morphology analysis

X-ray diffraction analyses were performed to investigate the crystallinity of the films, before and after annealing, us-

ing reflections from the Cu $K\alpha_1$ emission line (wavelength $=0.154\,059\,81$ nm) into a Siemens D5000 diffractometer with front monochromator. The applied power of the x-ray tube was 35 kV$\times$25 mA, the angular step was 0.005° within the studied 25°–68° range, and the quanta acquisition time was 5 s. All diffraction line characteristics were obtained by a deconvolution program using the Laurenzian approximation.

Surface morphologies of the as-grown, thermal and laser treated samples were studied via AFM analysis, in contact mode, using the Nanoscope III microscope of Digital Instruments. The measurements were performed with no prior cleaning or chemical etching of the surface.

III. RESULTS

A. Thermal simulation of the PLA processing

Simulation of the thermodynamic effect of KrF pulsed laser annealing on 800 nm thick thin films of ZnS on Si has been performed by numerically solving the one dimensional heat flow equation[13]

$$C_s \rho \frac{\partial T(x,t)}{\partial t} = \frac{\partial}{\partial x}\left(k \frac{\partial T(x,t)}{\partial x}\right) + S(x,t), \quad (1)$$

where C_s represents the specific heat, ρ is the density and k is the thermal conductivity of the different layers. The temperature T and heat generation S are functions of space and time. The heat generation can be described as

$$S(x,t) = P_d(t)\alpha(1-R)\exp(-\alpha x), \quad (2)$$

where $S(x,t)$ depends on the optical absorption α and surface reflectivity R of the material. $P_d(t)$ is the time dependent power density of the laser beam. Based on the simulation, Figs. 2 and 3 show, respectively, the theoretical depth-dependent maximum temperature and the surface temperature transient behavior of ZnS films deposited on Si substrates. Simulation was performed for fluences of 50, 100, 200, 300, 400, 500, and 610 mJ/cm^2, which compare with the experimental conditions used for laser annealing. Using constant values of $\tau_p = 20$ ns, the corresponding power densities P_d delivered may be determined, respectively, as 2.5, 5, 10, 15, 20, 25, and 30.5 MW/cm^2.

The predicted surface melting point and phase transition temperature from the cubic to hexagonal structure for single crystal ZnS are $T_{\text{melting}} = 2100$ K and $T_{\text{transition}} = 1295$ K, respectively.[14,15] Using these temperatures as reference points, we can determine the expected laser power density required for solid–liquid and cubic (sphalerite) to hexagonal (wurzite) phase transitions; i.e., respectively, 30.5 and 17 MW/cm^2 (610 and 340 mJ/cm^2). However, it is important

TABLE II. Results of incident laser energy E and pulse duration τ_p measurements and calculated energy density E_d with corresponding impinging laser power density P_d.

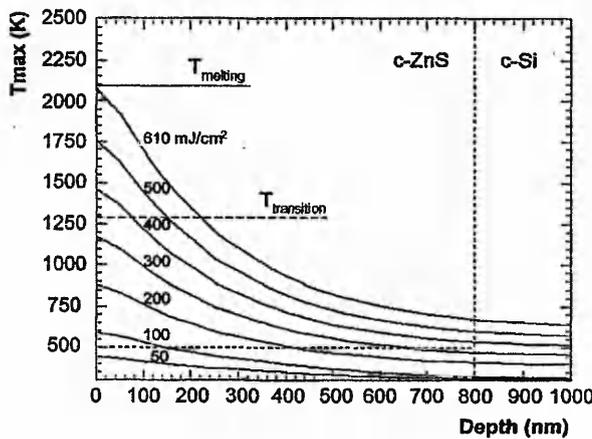| E (J)	0.87	1.21	1.41	1.44	1.77	1.94	2.13
E_d (mJ/cm^2)	217	304	353	362	443	485	534
τ_p (ns)	20.16	19.7	22.5	23.3	21.1	22	22
P_d (MW/cm^2)	10.76	15.43	15.68	15.53	20.99	22.04	24.27

FIG. 2. Theoretical maximal temperature distribution profile as function of depth into 800 nm ZnS film deposited onto a Si wafer during irradiation with a 20 ns pulsed KrF excimer laser at various fluences.

to stress that the simulations were performed based on the properties of single crystal ZnS for which the full range of optical and thermal parameters are known in its solid state phase,[5] since such comprehensive data does not exist for polycrystalline thin films. Assumptions used to perform the simulations were:

(i)   no significant difference between optical and thermal properties of the poly-ZnS:Mn phosphor and a single crystal c-ZnS layer;
(ii)   no temperature dependence of thermal properties;
(iii)   omission of the necessary transformation energy for phase transition, i.e., latent heat;
(iv)   no edge effects, since the width of the laser beam is much greater than the heated sample thickness;
(v)   perfect laser beam uniformity and constant rectangular laser pulse duration (20 ns); and
(vi)   homogeneous thin film composition.

Resulting calculated temperature profiles (Fig. 2) exhibit the shapes of an absorbing media (nonexponentially decay-
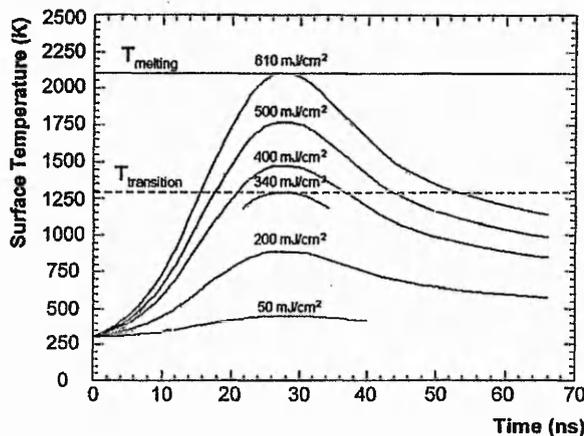

FIG. 3. Time dependent surface temperature profile of 800 nm ZnS film deposited onto a Si wafer during irradiation with a 20 ns pulsed KrF excimer laser at various fluences.
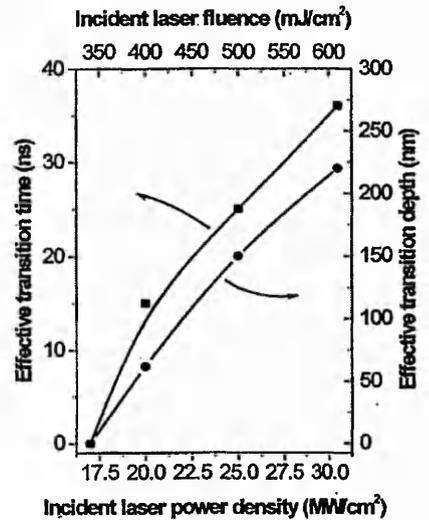

FIG. 4. Effective transition time and effective transition depth for sphalerite–wurzite transformation as function of incident laser power density and corresponding laser fluence. Curves are generated by computer algorithm and are included for clarity.

ing), where the penetration depth ($1/\alpha$) of the light is small compared to the thermal diffusion length L_d, i.e.,

$$1/\alpha < \sqrt{2D\tau_p}, \tag{3}$$

where $D=k/\rho C_s$ is the thermal diffusivity, and τ_p is the rectangular laser pulse duration. A direct consequence of this behavior is the τ_p dependency, stressing the very essential need for accurate measurement of this parameter, as anticipated in Sec. II. Using the parameters of single crystal cubic ZnS determined at room temperature ($k=0.251$ W/cm K; $C_s=472$ J/kg K; $\rho=4.076$ g/cm³),[16] with $\tau_p=20$ ns the calculated values of penetration depth and thermal diffusion length are, respectively, $1/\alpha=30$ nm and $L_d=722$ nm. The theoretical temperature at the phosphor–substrate interface calculated for the whole experimental range of laser power density values, i.e., from 10.76 to 24.27 MW/cm² (<500 mJ/cm²) lies within 400–600 °C.

Figure 3 highlights the simulated time dependence of the surface temperature. Especially shown are the short heating and cooling times involved under various laser fluences, owing to the short irradiation time (~20 ns). For example, when irradiation conditions for the cubic to hexagonal phase transition is reached, i.e., $T_{surface}=T_{transition}$, the curves drop quickly below the transition temperature. Figure 4 represents the effective time and effective transformation depth corresponding to values for $T_{surface}>=T_{transition}$. From about 20 MW/cm², the effective transformation time increases linearly up to the melting threshold and its value stays below 40 ns. The simulation indicates also that under solid state conditions, the sphalerite to wurzite transformation should be confined within the first 250 nm of the ZnS thin film.
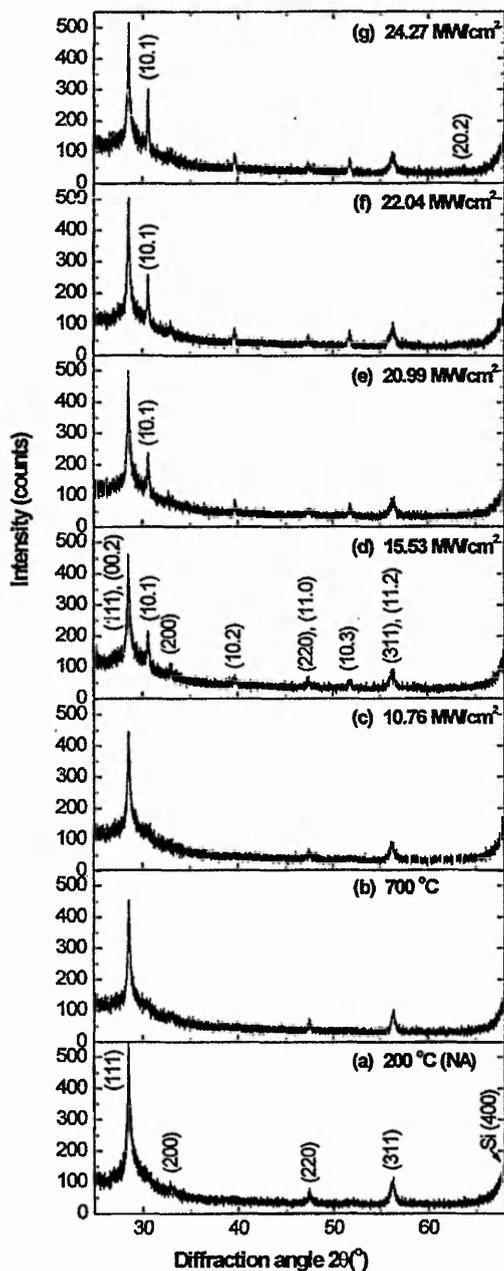
FIG. 5. XRD patterns of samples as-deposited (NA) at 200 °C (a), thermally annealed at 700 °C (b), and pulsed laser annealed under incident laser power densities of 10.76 MW/cm² (c), 15.53 MW/cm² (d), 20.99 MW/cm² (e), 22.04 MW/cm² (f), and 24.27 MW/cm² (g).

B. Experimental observations of the crystallinity dependence on annealing conditions

Figure 5 shows the measured XRD patterns of nonannealed (NA), thermally annealed (700< °C) and pulsed laser annealed samples at various power densities (10.76, 15.53, 20.99, 22.04, and 24.27 MW/cm²). Due to the long deposition time, the as-grown sample is considered to be effectively annealed thermally at the 200 °C substrate temperature used during growth. All the observed diffraction lines are identified in Table III. Line 9 represents the (400)

reflection from the c-Si substrate that has not been fully measured [Fig. 5(a)] to avoid saturation of the detection system. Each of the lines 1, 5, and 7 are made up of two unresolved lines from planes of nearly the same spacing and indicative of both cubic and hexagonal phases. Lines 2, 4, and 6 are distinctive of, respectively, (10.1), (10.2), and (10.3) hexagonal planes and line 3 involves the (200) plane reflections representative of only the cubic ZnS structure. It seems worthwhile to note that although the diamond and the sphalerite structures are geometrically identical, being both are face cubic centered, the (200) reflection is forbidden in silicon owing to its higher symmetry, i.e., all atoms are the same.[17] Unfortunately, the ZnS (200) peak is too weak to quantitatively compare the two main ZnS structures for the absence of an analyzable pure cubic line as reference.

However, the lack of diffraction from any hexagonal planes denote that as-grown and thermally annealed ZnS:Mn structures are and remain predominantly cubic [see Figs. 5(a) and 5(b)]. Consequently, the observed diffraction peaks are all attributed to the cubic forms, i.e., (111), (220), and (311). Analysis of their diffraction characteristics does not reveal significant grain growth or reorientation, which is in agreement with previous work.[18] The absence of strong texture effects and the polycrystalline nature of the thin films have been confirmed via the back-reflection Laue method.

XRD patterns of samples exposed to laser irradiation with optical power density greater than 10.76 MW/cm² [see Figs. 5(d)–5(g)] exhibit pronounced cubic to hexagonal transformation via the appearance of the hexagonal (10.1), (10.2), and (10.3) lines. Since the diffraction lines 1, 5, and 7 (Table III) corresponding to both allotropes are difficult to attribute to one or the other form, their diffraction characteristics have not been studied. Nevertheless, by examining their intensity ratios as a function of laser power, the effect of pulsed laser annealing on both crystalline structures can be compared. We observe that the increase in intensity ratios of purely hexagonal lines to unresolved lines $I_{10.1}/I_{00.2}$, I_{111}), $I_{10.3}/(I_{11.2}, I_{311})$, $I_{10.2}/(I_{00.2}, I_{111})$ and $I_{10.3}/(I_{00.2}, I_{111})$, represented by the solid lines in Fig. 6, demonstrates that the thin film becomes more hexagonal with increasing power density and that transformation occurs by reduction of the cubic structure. Also shown in Fig. 6, is the plot of the ratios of purely hexagonal lines: $I_{10.2}/I_{10.1}$, $I_{10.3}/I_{10.2}$ and $I_{10.3}/I_{10.1}$, against laser power density. It is suggested that the preferential wurtzite growth orientation is determined by planes of lower indices.

In Fig. 7, the diffraction characteristics of the (10.1) plane are investigated. Between about ~16 and ~21 MW/cm², the peak intensity $I_{10.1}$ is nearly constant before increasing rapidly beyond ~21 MW/cm², while the full width at half maximum (FWHM) and atomic spacing remain unchanged within experimental errors. Finally, evidence of the crystalline quality improvement of the phosphor thin film is clearly recognized under higher irradiation power (>22.02 MW/cm²), since a secondary diffraction line can be recognized at around 63.63° [Fig. 5(g)], which corresponds to the (20.2) plane.

J. Appl. Phys., Vol. 86, No. 5, 1 September 1999

Mastio et al.   2567

TABLE III. Noticeable diffraction lines in XRD patterns corresponding to calculated diffraction angles ($2\theta_{cal}$) from α-ZnS (sphalerite), β-ZnS (wurzite) and Si. Lattice parameters in nm and established at 300 K.

	α-ZnS ($a = 0.54102$)[a]		β-ZnS ($a_{2H} = 0.382\,26$, $c_{2H} = 0.626\,05$)[b]		Si ($a = 0.5431$)[c]	
Lines	hkl	$2\theta_{cal}(°)$	hkl	$2\theta_{cal}(°)$	hkl	$2\theta_{cal}(°)$
1	111	28.56	00.2	28.49		
2			10.1	30.52		
3	200	33.09				
4			10.2	39.59		
5	220	47.50	11.0	47.53		
6			10.3	51.74		
7	311	56.36	11.2	56.36		
8			20.2	63.53		
9					400	69.13

[a]J. C. Jamieson and H. H. Demarest, J. Phys. Chem. Solids **41**, 963 (1980).
[b]R. R. Reeber and G. W. Powell, J. Appl. Phys. **38**, 1531 (1967).
[c]Reference 16.

C. The dependence of the surface morphology on the annealing treatment

A surface morphology comparison, using AFM analysis, between as-grown samples and either thermally annealed or pulsed laser annealed samples, is presented in Fig. 8. Perspective surface representations of measured surface areas ($3 \times 3 \ \mu$m) highlight clearly that the surface texture is nearly unchanged using the conventional thermal annealing technique up to a maximum treatment temperature of 700 °C [Fig. 8(b)]. On the other hand, a gradual surface improvement with increasing irradiation energy using pulsed laser annealing processing is displayed in Figs. 8(c) and 8(d), which are representative of surfaces being irradiated under laser power densities of 15.68 and 24.27 MW/cm^2.
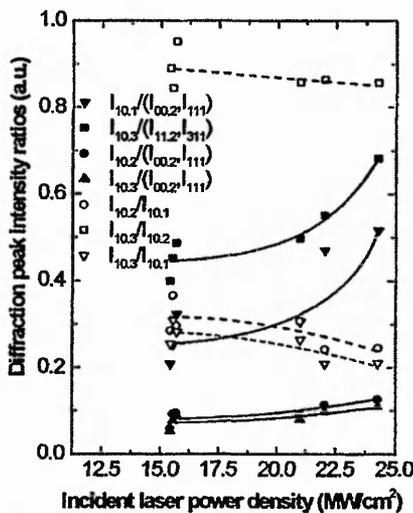

FIG. 6. Intensity ratios of purely hexagonal lines and unresolved lines as function of incident laser power density (solid lines). Intensity ratios of purely hexagonal lines in function of incident laser power density (dashed lines). Curves are generated by computer algorithm and are included for clarity.
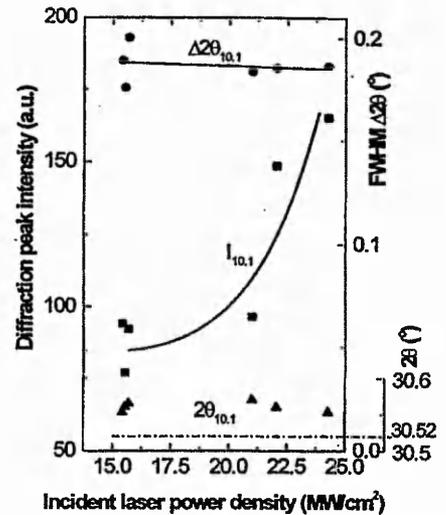

FIG. 7. (10.1) diffraction line characteristics as a function of incident laser power density. Dots=$\Delta 2\theta_{10.1}$ (FWHM), squares=$I_{10.1}$, triangles=$2\theta_{10.1}$. Horizontal axis line corresponds to the calculated diffraction angle in Table III. Curves are generated by computer algorithm and are included for clarity.

Results of the random mean square (RMS) interpolated over the whole analyzed surfaces are also reported. An important reduction in surface roughness is obtained when the sample is irradiated with 24.27 MW/cm^2 of laser power density (RMS=2 nm) compared to the as-grown (RMS=10 nm) or thermal annealed (RMS=12 nm) thin film. The top view of the sample with RMS=2 nm (Fig. 9) is particularly interesting since the six sides of the hexagonal crystallites are clearly distinguishable. An average measurement of the hexagons mean size is approximately 113 nm.

IV. DISCUSSION

As a general rule, it is often found that valence-bound solids can crystallize in several different structures for almost the same cohesive energy, resulting in allotropic materials. For ZnS, the various crystalline forms obtained can all be maintained at room temperature without apparent risk of spontaneous conversion to the energetically most favored one.[19] Thus, ZnS can exist at 300 K either in the zincblende or wurzite form. That property is clearly highlighted by laser annealed samples, while thermal annealed samples exhibit only the (111) oriented cubic structure. The major difference in the XRD patterns of laser and thermal annealed samples is the formation of the wurzite structure, the most stable allotrope at high temperatures, suggesting strongly that the temperatures involved in the former process exceed those of the latter limited to 700 °C. Simulation of the maximal surface temperature attained using the lowest power density of 10.76 MW/cm^2 suggests an effective surface annealing temperature of 875 °C, which conforms to the observed crystallographic modifications.

The diffraction peak intensities, corresponding to either the cubic or hexagonal structures, are indicative of the number of participating planes responsible for constructive interference. Analysis of the (111) diffraction peak for samples thermally annealed at temperatures from 200 °C (as-grown)

(a) Non-annealed.
RMS = 10nm

(b) Thermally annealed (700 °C).
RMS = 12nm

(c) Pulsed laser annealed (P = 15.68 MW/cm^2).
RMS = 5nm

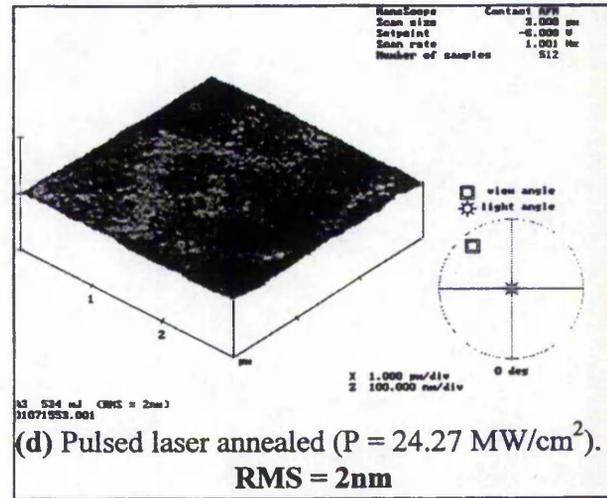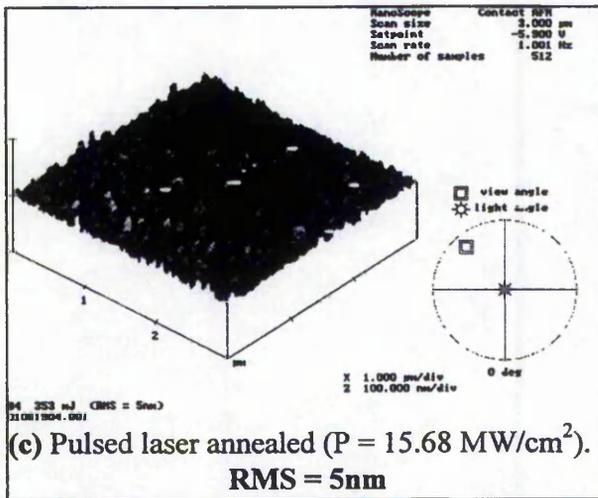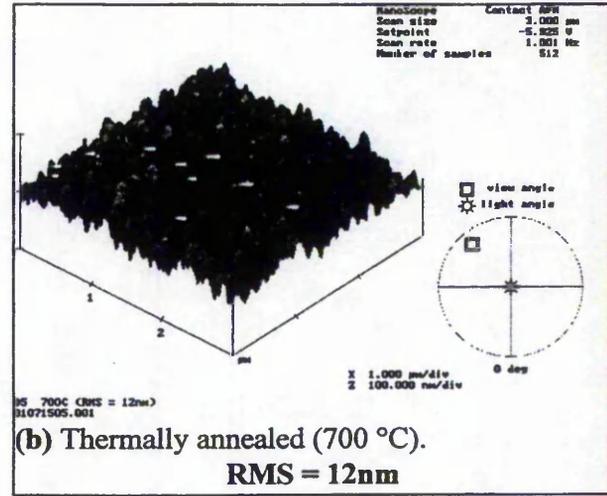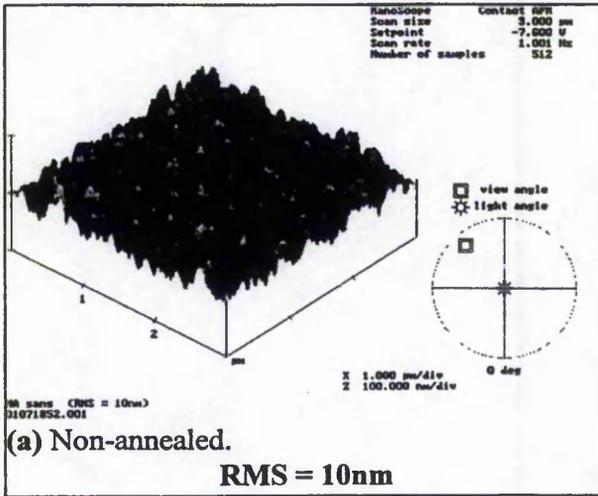**(d)** Pulsed laser annealed (P = 24.27 MW/cm^2).
RMS = 2nm

FIG. 8. Perspective representation of AFM images of samples as-grown (a), thermally annealed at 700 °C (b), and pulsed laser annealed under 16.68 MW/cm^2 (c), and 24.27 MW/cm^2 (d) irradiation power density.
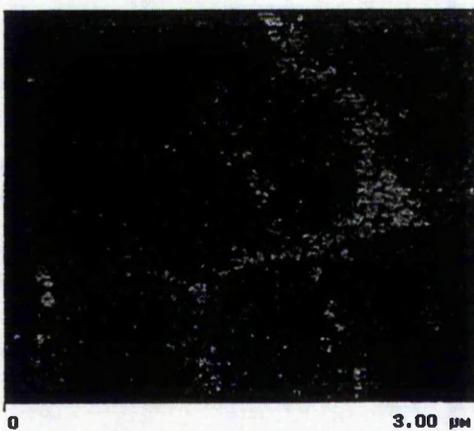

FIG. 9. AFM image (top view) of pulsed laser annealed sample under 24.27 MW/cm^2 irradiation power. Hexagonal crystallite shapes are clearly distinguishable within the $3 \times 3 \mu$m examined surface.

to 700 °C does not show significant variations in intensity, hence suggesting that the number of cubic crystallites remains unchanged within the phosphor layer. However, the diffraction intensities of the (10.1), (10.2), and (10.3) hexagonal planes, "formed" by laser annealing, are increased with the enhanced irradiation power, and two distinctive formation rates (hexagonal peak intensity increase/laser power density increase) are observed below and above 21 MW/cm^2 (see Figs. 6 and 7). Indeed, the cubic to hexagonal transformation appears to be stabilized from 16 to 21 MW/cm^2 and catalysed beyond and up to 24.27 MW/cm^2. The stable transformation region is attributed to the small difference between the lattice formation energies of the two main crystalline forms, i.e., cubic face centered (sphalerite) and hexagonal close packing (wurtzite). It is supposed that the latter property becomes predominant when the samples are laser annealed at power densities close to the phase transition threshold. Also, the spatial and transient temperature distribution within the phosphor layer is nonhomogeneous (Figs. 2 and 3). Therefore, neither structure is expected to have prece-

J. Appl. Phys., Vol. 86, No. 5, 1 September 1999

Mastio *et al.* 2569

dence in its formation, thus leading to the observed stable transformation region below 21 MW/cm^2. Confirmation of this hypothesis may be inferred from the work of Addamiano and Aven,[15] who investigated the stability of pure hexagonal crystals (grown from the melt), and the transformation of the cubic zincblende structure. It was observed that in the interval between 700 and 1150 °C, no full conversion to the cubic phase was achieved.

The first hexagonal lines were detected for laser annealed samples at power densities between 10.76 and 15.43 MW/cm^2, which is below the simulated phase transition threshold of 17 MW/cm^2. Remember however that this simulated value was determined using the optical and thermal parameters of single crystal ZnS. For polycrystalline thin films, as studied here, we would not expect such a sharp transition since the binding energies between atoms are less well defined. Evidently, the same is valid for the melting temperature, and hence we expect a similar shift even without considering localized melting at grain boundaries. Nevertheless, according to the model, solid state and solid–liquid transitions are expected to occur, respectively, in the regions of 17 and 30.5 MW/cm^2. The fact that the calculated transition threshold lies within the stabilized transition region is encouraging for the viability of the model. In the past, structural investigations and photoluminescence characterization of a ZnS thin (200 nm) film, deposited on Si and implanted with Mn ions, implied a possible melting threshold in the region of ~0.6–0.8 J/cm^2 when irradiated with a XeCl laser (40 ns duration) under 90 psi of Ne gas.[6] Interestingly, the calculation of the melting fluence using the experimentation conditions of the latter work and the present simulation model gives 0.7 J/cm^2, which agrees well with the experimental data.

Within the whole laser power density range examined in the present study, the FWHM ($\Delta 2\theta$), indicative of grain size, remains constant (Fig. 7). Therefore, we attribute the increase in the formation rate of hexagonal planes from enhanced transformation within the thickness of the film. This would be consistent with the maximal temperature versus depth simulation (Fig. 2) and with the behavior of the effective transition depth (Fig. 4). Results plotted in Fig. 4 suggest also that the effective transformation time using our laser annealing conditions is less than 40 ns. This result combined with the FWHM studies suggests that the laser processing used is too fast to facilitate grain growth and that transformation occurs in the solid state without a melting front. Note that the effective transformation time is correlated to depth–temperature profiles and in-depth transformation rate.

Under some assumptions of the crystalline quality, the average crystal dimension L perpendicular to the reflecting planes may be determined using the Sherrer equation[20]

$$B(2\theta) = 0.94\lambda/L \cos\theta, \tag{4}$$

where $B(2\theta)$ is the full width in radians subtended by the half maximum intensity width of the pattern peak, λ is the x-ray wavelength, and θ is half of the diffraction angle. Using Eq. (4), the average wurzite crystallite size within the 800 nm thin film has been calculated to be ~47 nm. A similar average grain size calculation of the nonannealed or ther-

mally annealed cubic structures gives ~31 nm. Note that an intrinsic increase of the crystallite dimension from the substrate–phosphor interface and throughout the phosphor layer is expected due to its nonuniform microscopic columnar nature.[21] This deposition characteristic would explain the bigger wurzite crystallite size, since they are formed in the upper part of the ZnS:Mn thin film.

AFM analysis highlights that the cubic to hexagonal phase transformation induced a gradual surface morphology improvement of up to a factor of 5, while the unaltered cubic form (non- and thermal annealed) remained essentially unchanged. Similar surface improvements related to crystalline quality and reorientation were reported when pseudoepitaxial ZnS films were grown on differently oriented Si substrates,[22,23] indicating that surface quality is directly related to crystalline ordering within the bulk of the thin film. It was also demonstrated[22] that the best-single crystal films were obtained with a Si (100) substrate, which was also used for the present study. The emergence of the hexagonal crystallite shapes at the surface, when the sample has been annealed at 24.27 MW/cm^2 (Fig. 9) possibly result from the well-oriented hexagonal structure (appearance of a secondary reflection peak in the diffraction pattern), and from the migration of voids and other defects to the column boundaries. Additionally, slight material removal via laser ablation is most likely to occur under our laser annealing conditions.[12] It is possible that this material loss may also take part in the surface smoothing effect.

V. CONCLUSIONS

Both as-grown and samples thermally annealed, (up to 700 °C), exhibit the zincblende form. Using the novel pulse laser annealing technique, it is suggested that allotropic transition from the cubic to hexagonal phase occurs between 10.76 and 15.43 MW/cm^2 of applied power density, i.e., below the calculated transition threshold of 17 MW/cm^2. Both the threshold shift and dual formation rate behavior, as opposed to a sharp transition, can be explained by the polycrystalline nature of the as-grown film, the small difference in lattice formation energies of the two main crystalline forms, and the nonhomogenous spatial and transient thermal distribution into the thin film.

From XRD analysis, the FWHM related to crystallite size remains constant using both annealing techniques. Considering the processing temperatures and time factors involved, we infer that the pulsed laser annealing processing time is insufficient to increase the crystalline size and that allotropic transition occurs in the solid state. It is concluded that the intensity increase of the hexagonal closed packed plane reflections is due to enhanced in-depth transformations.

Finally, AFM analysis demonstrates that a gradual surface smoothing is concomitant to the phase transition.

[1] Y. A. Ono, Encyclopedia Appl. Phys. **5**, 295 (1993).

[2] A. Fuh, R. P. Gallinger, P. Shuster, J. Adolph, and O. Caporaletti, Thin Solid Films **207**, 202 (1992).

[3] W. M. Cranton, R. Stevens, C. B. Thomas, A. H. Abdullah, and M. R. Craven, Proc. IEE Colloquium on Materials for Displays, 1995.

[4] W. M. Cranton, E. A. Mastio, C. B. Thomas, R. Stevens, and J. P. O. Evans, CLF-RAL Annual Report, 147 (1997).

[5] E. A. Mastio, W. M. Cranton, C. B. Thomas, E. Fogarassy, and S. de Unamuno, Appl. Surf. Sci. **139**, 35 (1999).

[6] H. S. Reehal, J. M. Gallego, and C. B. Edwards, Appl. Phys. Lett. **40**, 258 (1982).

[7] W. M. Cranton, D. M. Spink, R. Stevens, and C. B. Thomas, Thin Solid Films **226**, 156 (1993).

[8] H. S. Reehal and C. B. Edwards, Ann. Rep. Laser Facility Committee, SERC Rutherford and Appleton Labs, 2.17–2.18 (1981).

[9] S. Ozaki and S. Adachi, Jpn. J. Appl. Phys., Part 1 **32**, 5008 (1993).

[10] P. M. Savani, M. Philosophy thesis, University of Bradford, 1982, p. 97.

[11] D. Sands, F. X. Wagner, and P. H. Key, J. Appl. Phys. **85**, 3855 (1999).

[12] W. M. Cranton, P. H. Key, D. Sands, C. B. Thomas, and F. X. Wagner, Appl. Surf. Sci. **96–98**, 501 (1996).

[13] S. de Unamuno and E. Fogarassy, Appl. Surf. Sci. **36**, 1 (1989).

[14] A. Addamiano and P. A. Dell, J. Phys. Chem. **61**, 1020 (1957).

[15] A. Addamiano and M. Aven, J. Appl. Phys. **31**, 36 (1960).

[16] *Handbook of Chemistry and Physics*, 78th ed., edited by D. R. Lide (1997–1998).

[17] D. B. Cullity, *Elements of X-ray Diffraction*, ISBN 0-201-01174-3, (Addison-Wesley, Reading, MA, 1978).

[18] A. F. Cattel and A. G. Cullis, Thin Solid Films **92**, 211 (1982).

[19] J. S. Blakemore, *Solid State Physics*, 2nd. ed. (Cambridge University Press, Cambridge, 1985), p. 10.

[20] B. E. Warren, *X-ray Diffraction* (Dover, New York, 1990), p. 253.

[21] L. E. Tannas, *Flat Panels Displays and CRTs* (Van Nostrand, Princeton, 1985), p. 260.
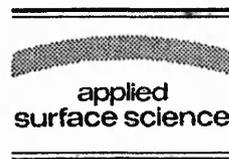
[22] T. G. R. Rawlins, J. Mater. Sci. **5**, 881 (1970).

[23] P. L. Jones, C. N. Litting, D. E. Mason, and V. A. Williams, Br. J. Appl. Phys., J. Phys. D **1**, 283 (1968).

Pulsed KrF laser annealing of RF sputtered ZnS:Mn thin films

E.A. Mastio [a,*], W.M. Cranton [a], C.B. Thomas [a], E. Fogarassy [b], S. de Unamuno [b]

[a] *The Nottingham Trent University (TNTU), Department of Electrical and Electronic Engineering, Burton Street, Nottingham NG1 4BU, UK*
[b] *Laboratoire PHASE (UPR du CNRS no. 292), BP 20, 67037 Strasbourg Cedex 2, France*

Abstract

Pulsed KrF laser annealing (PLA) of ZnS:Mn thin (800 nm) film phosphors has been investigated as an alternative to thermal annealing for the fabrication of electroluminescent devices. The influence of the surrounding gas pressure during exposure, the energy density (Ed) of the laser beam and the effect of double irradiation is reported. Luminescent properties as function of laser energy density (Ed) are determined via photoluminescent (PL) characterisation. Energy densities used vary from 53 to 777 mJ/cm^2. PL intensities are determined to be linearly dependent with Ed beyond a threshold of 150 mJ/cm^2 and maximum PL enhancement is a factor of 2.1 x. A thermal simulation of the PLA process suggest that PL improvement is proportional to deposited thermal energy and this in the solid state. The calculated melting threshold agrees well with previous work. © 1999 Elsevier Science B.V. All rights reserved.

Keywords: Pulsed KrF laser; Annealing; ZnS:Mn thin films

1. Introduction

The basic thin film electroluminescent (TFEL) device consists of a phosphor thin film sandwiched between two insulating layers; the former being submitted to a high electric field upon application of a suitable a.c. drive voltage between the dielectrics. Electroluminescent characteristics and performance of TFEL devices are governed by three distinct mechanisms, i.e., field emission of electrons from trapping states at the phosphor/insulator interface, acceleration of the charge carriers under the electric field, energy transfer of the latter to luminescent centres and radiative decay of these centres [1,2].

Critical to the radiative efficiency of any TFEL phosphor is a post-deposition annealing treatment at 500°C which facilitates the effective incorporation of the luminescent dopant ions within the host lattice. Unfortunately, this annealing temperature is limited by either the type of substrate or by the reduction of interface state density at the phosphor/dielectric interface as demonstrated in Ref. [3]. Therefore, the pulsed laser annealing (PLA) technique is a natural candidate for annealing the phosphor layer with little heating effect on the interface.

In this work we report on the PLA and its thermal simulation of a ZnS:Mn thin film which is the most efficient and widely used phosphor layer in TFEL devices.

2. Experimental conditions

2.1. Samples

Two 800 nm thick ZnS:Mn thin films have been deposited onto n-type single crystal ⟨100⟩ silicon

* Corresponding author. Tel.: +44-115-9418418 XT 2176; Fax: +44-115-9486567; E-mail: emmanuel.mastio@ntu.ac.uk

wafers by radio-frequency (RF) sputtering from a solid target in an argon atmosphere. During deposition, the substrate temperature was maintained at 200°C. The resultant ZnS:Mn thin films are polycrystalline (predominantly cubic) in nature [4], with columnar structure. The lattice match between zinc blende (cubic) and silicon is as good as 4%, i.e., 5.409 Å and 5.431 Å, respectively. In accordance to the optimised thermal annealing (TA) process, the used dopant concentration is 0.43 wt.%, i.e., $\sim 2.45 \times 10^{20}$ ions/cm^3 [5].

In the following, the two samples are reported as NTU185(LSF2) and NTU201(LSF3).

2.2. Laser annealing conditions

In order to achieve efficient absorption of the radiation in the thin film it is necessary to irradiate with photons of energy greater than the band gap (~ 3.66 eV for ZnS), since at lower energy the thin film is optically transparent. The wafers were annealed by the 20 ns pulses of a KrF excimer laser beam (249 nm, i.e., ~ 4.98 eV). Ed was varied from 53 to 777 mJ/cm^2 using blank silica plates as attenuators. Diagnostics of the beam profile whilst increasing the Ed by beam focusing were provided by a 249 nm sensitive CCD camera. The spatial uniformity of the radiation over its area and the Ed were determined to be $\pm 15\%$.

The PLA irradiations of the samples were carried out using an arrangement described previously [6] in which the 4-in. wafers were mounted in a pressure cell allowing pressurisation up to 150 psi. In this study, Ar gas has been used as an inert environment at atmospheric pressure and 150 psi ($= 13.6$ bar). The number of laser shots illuminating the same areas was either one or two. The time delay between consecutive pulses was always longer than one second, ensuring complete thermal relaxation of the wafers and the pressure cell.

To facilitate the accurate positioning of the target wafer in the KrF beam, a biaxial motion was constructed using micro-control stages with ± 10 μm accuracy over 200 mm travel range, capable of supporting 30 kg. PC control of the stepper motor drives allowed irradiation of specific areas of the wafer.

2.3. Photoluminescence analysis

After PLA, the characteristic orange Mn photoluminescence was examined at room temperature. The isoelectronic Mn^{2+} ion has a first excitation state at 2.1 eV above the ground state and a radiative decay of the excited ions back to their ground level produces the visible emission. Excitation of the phosphor was accomplished with a N$_2$ (337 nm, i.e., ~ 3.68 eV) pulsed laser operating at 20 Hz, 6 mW average power and 400 mJ maximal energy per pulse. For measurement, a Minolta LS110 luminance-meter, was placed at right angles to the examined samples. A remote voltmeter coupled to the Minolta output permitted signal readings even operating in a dark room (very low background signal) and a probe-station allowed accurate positioning of the tested samples. The reported values are all relative to non-annealed regions of the examined wafer.

2.4. Simulation

As stated in the introduction, the temperature control of the phosphor bulk and its interface during thermal processing are crucial for TFEL applications. Since measurement of these temperatures during pulsed LA are difficult, the thermal effect of LA has been simulated by solving the one-dimensional heat flow equation [7]: $C_s \rho (\partial T(x, t))/(\partial t) = ((\partial)/(\partial x))(k((\partial T(x, t))/(\partial x))) + S(x, t)$, where C_s is the specific heat, ρ the density and k the thermal conductivity of the sample. The temperature T and heat generation S are functions of space and time. The heat generation: $S(x, t) = P(t)\alpha(1 - R)\exp(-\alpha x)$ depends on the optical absorption α and surface reflectivity R of the materials. $P(t)$ is the time-dependent power density of the laser beam. Therefore, the accuracy of the modelling is strongly related to how precisely the optical and thermal properties of the irradiated materials are known. Si is probably one of the best known components thanks to semiconductor technology but for the phosphor layer, even if ZnS is a well known material, different values can be found in the literature. The assumption was made that the doped poly-ZnS thin film possesses the same properties of a single crystal zinc

Table 1
Optical and thermal parameters of the phosphor thin film and the substrate used for simulation

At 300 K	Cubic ZnS (poly-ZnS:Mn)	C–Si
$R_{(\perp \text{ to surf.})}$ at 249 nm	0.27 [8]	–
α (cm^{-1}) at 249 nm	3.33×10^5 [8]	–
T_{melting} (K)	2100 ± 20 (under $p_{Ar} = 150$ psi) [9]	1683 [7]
$T_{\text{transition}}$ (K)	1295 [10]	–
k (W/cm K)	0.251 [11]	1.40 [7]
C_s (J/kg K)	472 [11]	745 [7]
ρ (g/cm^3)	4.079 [11]	2.32 [7]

blende structure. Hence, the different parameters used for calculation are reported in Table 1.

3. Results and discussion

3.1. Simulation

Based on the simulation, Fig. 1 shows the theoretical depth-dependent maximum temperature of the samples for the used LA conditions. The calculated temperature profiles are very significant for absorbing media where the penetration depth of the light is small compared to the thermal diffusion length, i.e.,

$1/\alpha < \sqrt{2D\tau_p}$ with $D = K/\rho C_s$. D in cm^2 s^{-1} and τ_p in seconds are the thermal diffusivity and the rectangular laser pulse duration, respectively. In this case, the heat source becomes a surface source and the heat propagation into the thin film is governed by its thermal characteristics. At the interface, the slope changes are not clearly defined, demonstrating that the Si wafer acts like a very soft heat sink. The critical interface temperature of 500°C, above which reduction of interface state density occurs, is reached at ~ 340 mJ/cm^2.

As deduced from Fig. 2. which gives the maximum surface temperature as a function of Ed, melting should occur at 610 mJ/cm^2. In the past, structural investigations and PL characterisation of ZnS thin (200 nm) film, deposited on Si and implanted with Mn ions, implied a possible melting threshold in the region of ~ 0.6–0.8 J/cm^2 when irradiated with a XeCl laser under 90 psi of Ne [12]. Interestingly, the calculation of the melting fluence using the experimentation conditions of the latter work gives 700 mJ/cm^2 which agrees well, validating the thermal model.

The calculated transition fluence is 340 mJ/cm^2 and correspond to the cubic-hexagonal transformation where hexagonal is the stable allotrope at high temperatures. Also, Fig. 2. exhibits a linear dependence between optical energy density and maximal temperature rise.
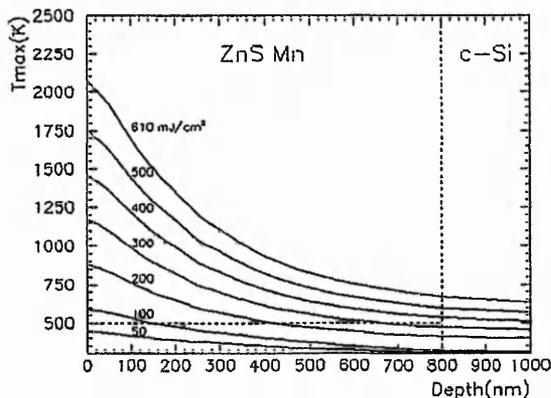

Fig. 1. Temperature distribution profile as function of depth into 800 nm ZnS:Mn film deposited onto a Si wafer during irradiation with a 20 ns pulsed KrF excimer laser at various fluences.
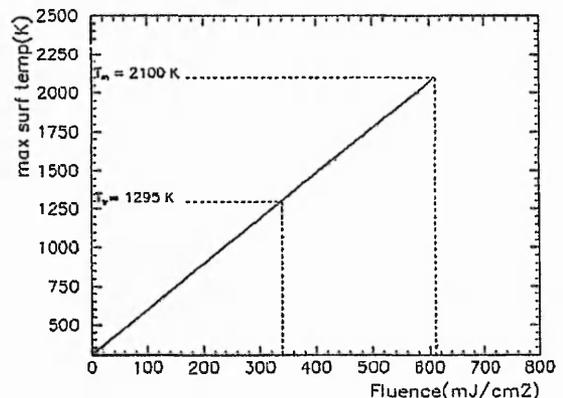

Fig. 2. Maximal surface temperature as function of laser fluences of 800 nm ZnS:Mn film deposited onto a Si wafer during irradiation with a 20 ns pulsed KrF excimer laser.

3.2. Photoluminescence

Increase in PL relatively to non-PLA samples has been obtained with the specimens held under 150 psi of argon pressure as reported in Figs. 3 and 4. As shown in Fig. 2, no fusion should occur below 610 mJ/cm^2. Hence, higher PL is due to Mn diffusion into sulphur-surrounded Zn vacancies of the lattice, increasing the number of effective luminescent centres. This increase is linearly dependent with the laser fluence even in the range where the phase transition is expected (Fig. 4). Double shot irradiation also shows this characteristic but at higher rate of improvement (Fig. 3). Since the action of several pulses cannot be additive due to the interval between them (nanosecond regime), it can be concluded that the structure formed on each shot influences subsequent coupling of the radiation to the samples. Therefore, as the Ed is increasing, the double shot irradiation benefit from improved coupling due to changes induced by the initial shot.
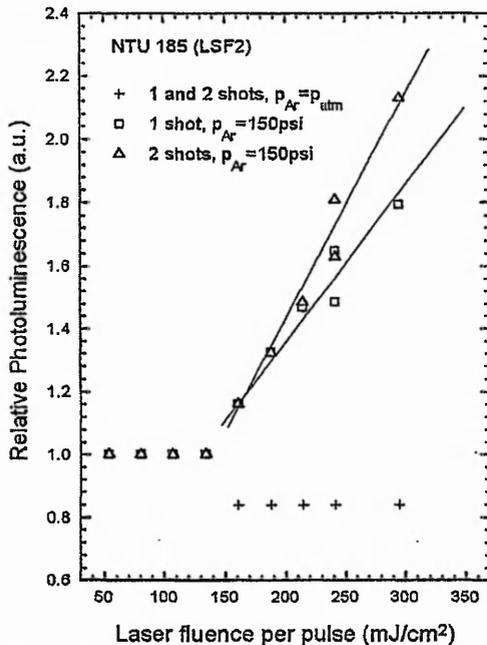

Fig. 3. Relative PL vs. Ed of 800 nm ZnS:Mn film deposited onto a Si wafer after LA with a 20 ns pulsed KrF excimer laser. Single and double shot irradiation under atmospheric and 150 psi Ar pressure.
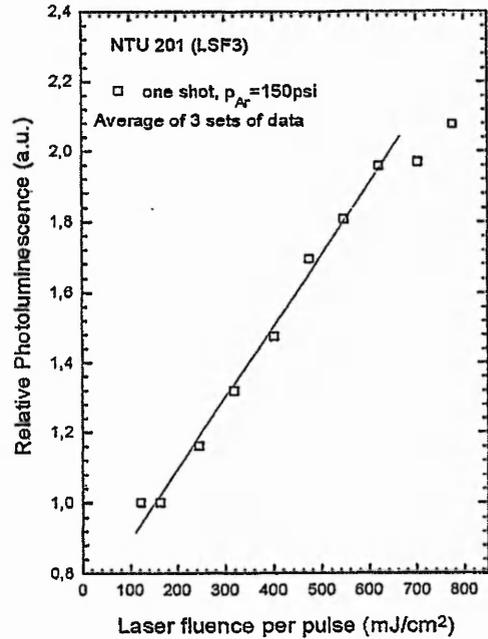

Fig. 4. Relative PL vs. Ed of 800 nm ZnS:Mn film deposited onto a Si wafer after LA with a 20 ns pulsed KrF excimer laser. Single shot irradiation before melting-regrowth process under 150 psi Ar pressure.

ZnS sublimes before melting at normal pressure and Fig. 3 highlights clearly the predicted vaporisation when irradiating under one atmosphere. The loss of material is followed by PL reduction (crosses) with an ablation threshold of ~ 150 mJ/cm^2. This value appears to be in fairly good agreement with that fund when using a XeCl excimer source to process a ZnS target, at atmospheric pressure [13]. It is interesting to note that the optical energy density necessary for sublimation in one case ($p_{ar} = p_{atm}$), is also equal to the one necessary for photoluminescence improvement ($p_{ar} = 150$ psi).

4. Conclusions

The most significant result to emerge from the present study is the linear dependence between PL improvement factor and Ed when irradiating under 150 psi of Ar pressure. Thermal simulation of PLA processing shows that this improvement is obtained in the solid state and that the linearity is conserved during phase transition. Recently, atomic force mi-

croscopy (AFM) measurements [14] of a new set of samples show reduction in waviness and roughness above calculated melting point, validating the assumption made on the optical and thermal properties of the irradiated samples. In a near future, X-ray diffraction (XRD) characterisation technique will be used to probe the metallurgic transition.

Finally, the linear characteristics shown by calculation and experimentation imply a correlation between the Mn luminescence efficiency and the temperature rise of the bulk.

Acknowledgements

References

[1] D.H. Smith, Modelling a.c. thin-film electroluminescent devices, J. Luminescence 23 (1981) 209–235.

[2] A. Onton, V. Marello, Physical phenomena in ac thin-film electroluminescent phosphors, Advances in Image Pickup and Display 5 (1982) 137–197.

[3] W.M. Cranton, R. Stevens, C.B. Thomas, A.H. Abdullah, M.R. Craven, Proc. IEE Colloquium on Materials for displays, October 1995.

[4] L.E. Tannas, in: Van Nostrand (Ed.), Flat Panels Displays and CRTs, ISBN 0-442-28250-8, 1985, p. 260.

[5] W.M. Cranton, PhD Thesis, Univ. of Bradford, 1995.

[6] W.M. Cranton, E.A. Mastio, C.B. Thomas, R. Stevens, Laser annealing for high intensity flat screen displays, Central Laser Facility Rutherford Appleton Laboratory Annual Report 1996/1997, pp. 147–148.

[7] S. de Unamuno, E. Fogarassy, Appl. Surf. Sci. 36 (1989) 1.

[8] S. Ozaki, S. Adachi, Optical constants of cubic ZnS, Jpn. J. Appl. Phys. 32 (1993) 5008–5013.

[9] A. Addamiano, P.A. Dell, The melting point of Zinc Sulfide, J. Phys. Chem. 61 (1957) 1020–1021.

[10] A. Addamiano, M. Aven, Some properties of zinc sulfide crystals grown from the melt, J. Appl. Phys. 31 (1960) 36–39.

[11] D.R. Lide (Ed.), Handbook of Chemistry and Physics, 78th edn., 1997–1998.

[12] H.S. Reehal, J.M. Gallego, C.B. Edwards, Pulsed XeCl laser annealing of ZnS:Mn thin films, Appl. Phys. Lett. 40 (3) (1982) 258–260.

[13] W.M. Cranton, P.H. Key, D. Sands, C.B. Thomas, F.X. Wagner, XeCl laser ablation of thin film ZnS, Appl. Surf. Sci. 96–98 (3) (1986) 501–504.

[14] M. Robino (IPCMS-GOLNO), private communication.

ELSEVIER

Ablation study on pulsed KrF laser annealed electroluminescent ZnS:Mn/Y₂O₃ multilayers deposited on Si

E.A. Mastio [a,*], E. Fogarassy [b], W.M. Cranton [a], C.B. Thomas [a]

[a] *The Nottingham Trent University, Department of Electrical and Electronic Engineering, Burton Street, Nottingham NG1 4BU, England, UK*

[b] *Laboratoire PHASE (UPR du CNRS no. 292), BP 20, 67037 Strasbourg Cedex 2, France*

Abstract

The ZnS:Mn active layer of a thin film electroluminescent (TFEL) device has been annealed under 1.034 MPa (10.34 bar, 150 psi) of argon pressure using a 20-ns pulsed KrF excimer laser. We investigate the effects of multiple shots at various power densities upon the ablation rates of the ZnS:Mn layer. The results are compared to a thermal simulation of the laser-matter interaction using single pulse irradiation, and it is inferred that the cubic to hexagonal transition and melting of ZnS:Mn decrease the ablation rate. © 1999 Elsevier Science B.V. All rights reserved.

Keywords: ZnS:Mn; Laser annealing; Ablation; Thin films; Electroluminescence; Thermal model

1. Introduction

It is known that annealing is an important step in the manufacturing process of thin film electroluminescent devices (TFEL), since it is required for the activation of luminescent dopant ions and for improved crystalline quality. Conventional thermal annealing temperatures are limited to 500°C either by the substrate, e.g., glass or by the reduction of the interface state density at the phosphor–dielectric interface [1]. However, pulsed excimer laser treatment promises a technique that will heat the phosphor layer for very short times with minimal energy absorption at the interfaces and cladding dielectrics,

thereby preventing the detrimental modification of the interface states which reduces the device efficiency. The viability of KrF laser annealing under 1.034 MPa (10.34 bar, 150 psi) of argon pressure for activating the luminescent dopant of ZnS:Mn phosphors has recently been demonstrated by the authors [2]. Critical to its technological development for electroluminescent application is the definition of the parameters which are needed to successfully anneal the phosphor thin films with no, or minimal ablation.

The aim of this paper is to analyse and discuss the effects of multiple irradiation shots at various power densities during laser ablation of a TFEL base layer, i.e., a stack of 800 nm of ZnS:Mn (phosphor) and 300 nm of Y₂O₃ (insulator) films deposited onto a 4-in. silicon wafer. Also to be considered is the evaluation of the remaining phosphor thickness obtained under the various annealing conditions since

* Corresponding author. Tel.: +44-115-8482176; fax: +44-115-9486567.

E-mail address: mastio@phase.c-strasbourg.fr (E.A. Mastio)

film thickness is directly related to electroluminescent characteristics of the fabricated devices, e.g., threshold voltage and luminance. A thermal simulation based on single shot laser irradiation of the studied base layer is also presented for a better understanding of the ablation mechanism involved.

2. Experimental

A thin film of Y_2O_3 (300 nm) and a second layer of ZnS:Mn (800 nm) were successively radio-frequency sputtered onto a 4-in. (100) Si wafer-substrate. The substrate temperature was maintained at 200°C during deposition in 2 mbar of Ar. The vacuum deposition chamber had a basic pressure of 1×10^{-7} mbar.

For laser processing, the sample was mounted in an evacuable pressure cell fitted with an UV-grade quartz window. Pulsed KrF laser irradiations (248 nm; 20 ns duration) were performed under a static argon pressure of 1.034 MPa (10.34 bar, 150 psi). The impinging power density range varied from 8 MW/cm^2 (160 mJ/cm^2) to 49 MW/cm^2 (980 mJ/cm^2) with steps smaller than 5 MW/cm^2 (100 mJ/cm^2). Note that using a 20-ns pulse duration, the conversion factor between (mJ/cm^2) and (MW/cm^2) equals 20. The number of shots on single target areas varied from 1 to 20 with time delays between consecutive pulses longer than 1 s, ensuring complete thermal relaxation of the target. Ablation depths were measured from the nonlaser-treated surface (as-grown) to the centre of the irradiated regions using a Tencor PII profilometer.

3. Results

3.1. Thermal simulation

A thermal model of the KrF laser processing, previously validated on a simple structure based on silicon coated with an 800-nm layer of ZnS:Mn [3] is used to obtain the maximal transient temperatures attained within the TFEL base layer. As in Ref. [3],

the temperatures are obtained by solving the one-dimensional heat flow equation:

$$C_s \rho \frac{\partial T(x,t)}{\partial t} = \frac{\partial}{\partial x}\left(k \frac{\partial T(x,t)}{\partial x} \right) + S(x,t),$$

where C_s is the specific heat, ρ the density and k the thermal conductivity of the materials. The heat generation term: $S(x,t) = P(t)\alpha(1 - R)\exp(-\alpha x)$ depends on the optical absorption constant α and surface reflectivity R of the materials. $P(t)$ is the time dependent power density of the laser beam. The optical and thermal parameters used for the simulation are listed in Table 1. It is assumed that the as-grown polycrystalline ZnS:Mn and Y_2O_3 layers possess the same properties as the face centred cubic ZnS and body centred bixbyite Y_2O_3 single crystals, respectively.

Based on the thermal model, Fig. 1 shows the spatial behaviour of the maximum temperatures reached within the stack of ZnS:Mn and Y_2O_3 layers after a single pulse laser irradiation of 20 ns. Surface temperatures of the zinc sulphide layer corresponding to sublimation, cubic to hexagonal transition, and melting are estimated to be attained at power densities of, respectively, ~ 16.6, 17, and 30.5 MW/cm^2. Results of thermal modelling are unchanged whether simulating the laser irradiation in air at atmospheric

Table 1

Parameters used to solve the one-dimensional thermal model. Thermal and optical properties are determined, respectively, at 300 K and for a 248-nm irradiation wavelength. R represents the reflectivity at normal incidence, α the optical absorption coefficient, k the thermal conductivity, C_s the specific heat, and ρ the density. $T_{transition}$ is the necessary temperature for the phase transition from the cubic to the hexagonal forms of the corresponding materials

	c-ZnS	c-Y_2O_3	c-Si [6]
$R_{(\perp \text{ to surf.})}$	0.27 [7]	0.134*	0.665
α (cm^{-1})	3.33×10^5 [7]	2.826*	1.7×10^6
$T_{melting}$ (K)	2100 ± 20 [8]	2710 [9]	1683
$T_{transition}$ (K)	1295 [10]	2640 [9]	–
$T_{sublimation}$ (K)	~ 1273 [11] (estimated value)	–	–
k (mW/cm K)	251 [12]	133 [13]	1400
C_s (J/kg K)	472 [12]	455.65 [14]	745
ρ (g/cm^3)	4.079 [12]	5.033 [15]	2.32

*Values calculated using the real and imaginary parts or the refractive index of, respectively, 2.155 [4] and 5.6×10^{-6} [5].
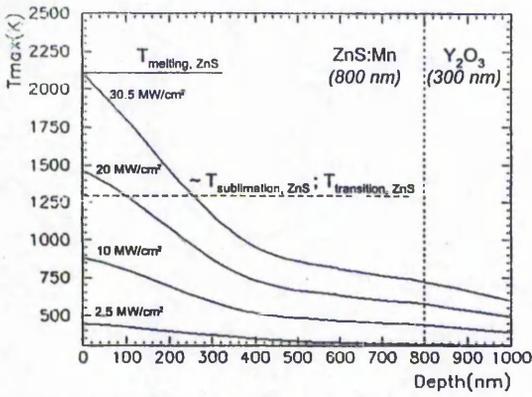
Fig. 1. Simulated maximal temperature distribution profile as a function of depth for 800 nm thick ZnS:Mn and 300 nm thick Y_2O_3 thin films successively deposited onto a Si wafer, during a single pulse from 20 ns duration KrF excimer laser at various power densities. Horizontal lines represent the temperature necessary for sublimation (~ 1273 K), phase transition (1295 K), and melting (2100 K) of zinc sulphide.

pressure, or under 1.034 MPa (10.34 bar, 150 psi) of Ar. The respective thermal conductivity of both target environments, determined at 300 K are: $k_{air (1 bar)} = 0.261$ mW/cm K [16] and $k_{Ar(10...34 bar)} \sim 0.26$ mW/cm K [17].

3.2. Ablation depth and ablation rate analyses

The profile analysis of the laser processed regions did not highlight any material removal when 1 to 20 pulses were used at power densities of 8 or 15 MW/cm^2 and significant measurable ablation occurred only after three pulses of 20 MW/cm^2. Fig. 2 shows the typical form of a profilometer scan measured across the centre of an ablated region.

Figs. 3 and 4 represent the depth of material removed and the ablation rate (thickness of material removed per pulse) obtained with 3 to 20 shots of various laser power densities, respectively. In both figures, all the data representing a specific pulse number configuration, i.e., $3\times$, $5\times$, $10\times$, $15\times$, or $20\times$, are quasi-constant from 20 to 23 MW/cm^2 before increasing to a maximum at ~ 31 MW/cm^2. Above ~ 31 MW/cm^2, a minimum is reached at ~ 40 MW/cm^2 for 3 to 10 pulses, which is shifting to ~ 32 MW/cm^2 at higher pulse repetitions. Exceeding those minima, the accumulated ablated depth (Fig. 3) and ablation rate (Fig. 4) increase again with
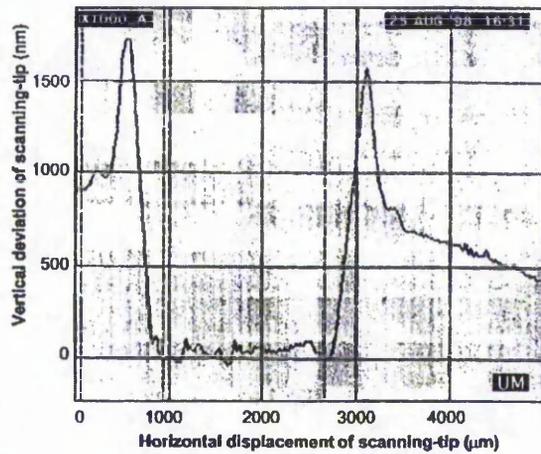

Fig. 2. Profilometer scan of a laser treated area with 20 pulses of 823 mJ/cm^2 (41 MW/cm^2).

increasing laser power densities up to ~ 43 MW/cm^2. In Fig. 3, it is interesting to note that up to five shots, the total depth removed under 20
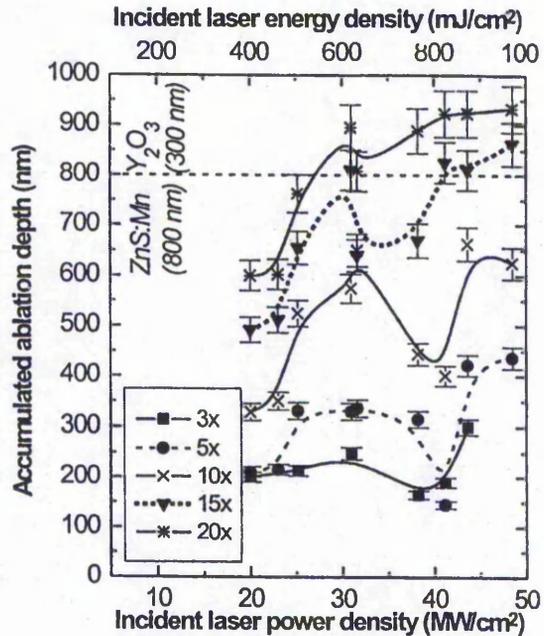

Fig. 3. Cumulative ablated depth plotted against the incident laser power density at a range of pulse numbers for a stack of 800 nm of ZnS:Mn and 300 nm of Y_2O_3. Curves for each specific number of pulses ($3\times$, $5\times$, $10\times$, $15\times$, $20\times$) are fitted by B-splines and drawn for clarity.

MW/cm^2 is smaller than when nearly twice the power density is used, i.e., 41 MW/cm^2. Similarly, the whole 800-nm thick phosphor layer can be removed with 15 irradiations at 31 MW/cm^2 and only 640 nm with slightly higher power density, i.e., 32 MW/cm^2. Fig. 4 shows that, at constant laser power densities, the ablation rate decreases with number of pulses. Exceptions arise at around 40 MW/cm^2 where minima of lower and higher shot numbers do not overlap.

Results of the averaged ablation rates obtained from the different pulse numbers for various power densities are plotted in Fig. 5. The average values have been obtained by (i) plotting the accumulated ablation depths as a function of pulse numbers for various power densities, and (ii) linearly extrapolating the curves to the origin (see for example, inset in Fig. 5). The slope of a linear interpolation is therefore equal to an ablation rate (averaged from all pulse configurations) for a given value of incident laser power density. The data shown in Fig. 5 exhibit

Fig. 5. Ablation rate linearly averaged for all pulse number configurations as a function of incident laser power density and energy density. The data correspond to laser irradiations of (a) 20 MW/cm^2, (b) 23 MW/cm^2, (c) 25 MW/cm^2, (d) 31 MW/cm^2, (e) 32 MW/cm^2, (f) 38 MW/cm^2, (g) 41 MW/cm^2, (h) 43 MW/cm^2, (i) 49 MW/cm^2. Error bars correspond to the fitting errors with respect to the experimental values. The two distinctive curvature changes in the B-spline fitted dashed line are related to the allotropic transition (from cubic to hexagonal) and melting of ZnS:Mn. Inset: Example of a linear fit performed on experimental values, i.e., ablated depth vs. number of pulses, corresponding to the laser irradiation of (d) 31 MW/cm^2.

similar behaviour to those in Figs. 3 and 4, i.e., quasi-constant from 20 to 23 MW/cm^2, maximum at ~ 31 MW/cm^2, and minimum between ~ 32 and ~ 40 MW/cm^2. The quasi-constant region (constant ablation rate) and minima region (reduction of the ablation rate) are attributed to the allotropic transition and melting of ZnS:Mn, which will be discussed in Section 4.

4. Discussion

Due to the low sublimation temperature of ZnS (~ 1300 K), the phosphor layer may be subjected to ablation during excimer laser processing. Indeed, material losses have been observed in the past, using
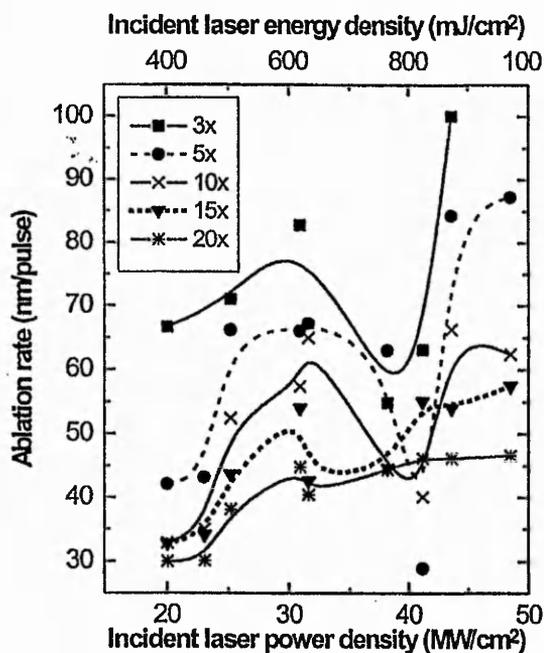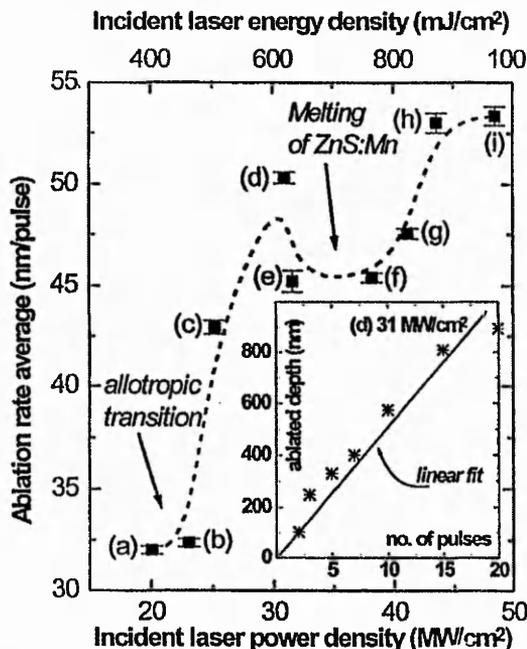

Fig. 4. Ablation rates as function of incident laser power density and energy density at a range of pulse numbers for a stack of 800 nm of ZnS:Mn and 300 nm of Y_2O_3. Curves for each specific number of pulses (3×, 5×, 10×, 15×, 20×) are fitted by B-splines and drawn for clarity.

XeCl lasers with the specimens held under argon pressures up to 1.034 MPa (10.34 bar, 150 psi) [11,18]. Recently, Sands et al. [19] concluded that sublimation is the controlling factor for the onset of XeCl laser ablation in ZnS thin films deposited on Si. In the present study, no surface morphology modification has been established on laser treated regions with power densities of 8 and 15 MW/cm^2. Thus, we estimate the onset for ablation to be greater than 15 MW/cm^2, which does not disagree with the simulated power density necessary for surface sublimation, i.e., $\sim$ 16.6 MW/cm^2 (see Section 3.1).

In Ref. [8], Addiamamo and Dell were able to melt ZnS under 150 psi of Ar pressure and determined a melting point of 2100 ± 20 K. With our experimental conditions and according to our thermal model, we anticipate the melting of ZnS:Mn to start, at the surface, under a laser irradiation of 30.5 MW/cm^2, which from our results corresponds to a reduction in ablation rate (Fig. 5). Previously demonstrated in Ref. [20] is that the excimer laser ablation rate in ZnS thin films deposited on Si is linearly dependent upon surface temperature and heat distribution within the thin film. Thus, when significant absorption of radiation is providing the latent heat of phase transformations, the surface temperature may be lower and a reduction in the ablation rates can be expected. Hence, according to the simulated surface melting condition, we may attribute the minimum region seen on the averaged ablation rate data (between $\sim$ 32 and $\sim$ 40 MW/cm^2, Fig. 5) to the phase change from solid to liquid (melting) within the phosphor layer. Following the same reasoning, we assign the quasi-constant region (from 20 to 23 MW/cm^2, Fig. 5) to the cubic to hexagonal transition of ZnS:Mn, which is predicted by the model to commence at the surface with an impinging laser power density of 17 MW/cm^2. In turn, the distinctive ablation rate reduction by melting could imply that more energy is needed for melting than for allotropic transition. The latter supposition agrees with the experimental values $\Delta_{melting} H = 59\,700$ J/mol and $\Delta_{transition} H = 12\,857$ J/mol [21].

Finally, the accumulated depths (Fig. 3) and ablation rates (Fig. 4) increase and decrease, respectively, with increasing number of laser pulses. This suggests that the phosphor thin film is more difficult to remove with increasing pit depth and that the first laser pulse impinging on a target area is more effective at removing material than the following pulses.

5. Conclusions

The evolution of the laser ablation characteristics of ZnS:Mn has been examined under various pulse numbers and laser power densities. Combining the ablation study and results of the thermal model, we infer that allotropic transition and melting of ZnS:Mn are responsible for the reductions in ablation rate due to conversion of thermal energy to initiate the phase transformations.

References

[1] W.M. Cranton, R. Stevens, C.B. Thomas, A.H. Abdullah, M.R. Craven, Proc. IEEE Colloq. Mater. Displays (1995) .
[2] E.A. Mastio, W.M. Cranton, C.B. Thomas, E. Fogarassy, S. de Unamuno, Appl. Surf. Sci. 138–139 (1999) 35.
[3] E.A. Mastio, M. Robino, E. Fogarassy, M.R. Craven, W.M. Cranton, C.B. Thomas, J. Appl. Phys. 86 (1999) 1.
[4] T. Tomiki, J. Tamashiro, Y. Tanahara, A. Yamada, H. Fukutani, T. Miyahara, H. Kato, S. Shin, M. Ishigame, J. Phys. Soc. Jpn. 55 (1986) 4543.
[5] Y. Nigara, Jpn. J. Appl. Phys. 7 (1968) 404.
[6] S. de Unamuno, E. Fogarassy, Appl. Surf. Sci. 36 (1989) 1.
[7] S. Ozaki, S. Adachi, Jpn. J. Appl. Phys. 32 (1993) 5008.
[8] A. Addamiano, P.A. Dell, J. Phys. Chem. 61 (1957) 1020.
[9] L.M. Lopato, B.S. Nigmanov, A.V. Shevchenko, Z.A. Zaitseva, Inorg. Mater. 22 (1986) 678.
[10] A. Addamiano, M. Aven, J. Appl. Phys. 31 (1960) 36.
[11] W.M. Cranton, P.H. Key, D. Sands, C.B. Thomas, F.X. Wagner, Appl. Surf. Sci. 96–98 (1986) 501.
[12] D.R. Lide (Ed), Handbook of Chemistry and Physics, 78th edn., CRC Press, Boca Raton, FL, 1997 1998.
[13] Y.S. Touloukian (Ed.), Thermophysical properties of matter, Thermal Conductivity of Nonmetallic Solids 2 IFI/Plenum, New York, 1970.
[14] Y.S. Touloukian (Ed.), Thermophysical properties of matter, Specific Heat of Nonmetallic Solids 5 IFI/Plenum, New York, 1970.
[15] W.J. Troff, M.E. Thomas, in: Handbook of Optical Constants of Solids II, Academic Press, 1991, p. 1079.
[16] E. Dwight (Ed.), American Institute of Physics Handbook, 2nd edn., McGraw-Hill, New York, 1972.
[17] B.J. Bailey, K. Kellner, Physica 39 (1968) 444.
[18] H.S. Reehal, J.M. Gallego, C.B. Edwards, Appl. Phys. Lett. 40 (1982) 258.
[19] D. Sands, P. Key, J. Hoyland, Appl. Surf. Sci. 138–139 (1999) 240.
[20] D. Sands, F.X. Wagner, P.H. Key, J. Appl. Phys. 85 (1999) 3855.
[21] R.C. Sharma, Y.A. Chang, J. Phase Equilibria 17 (1996) 261.